§ Chemical Reaction and Flow Modeling in Fullerene and Nanotube Production

Carl D. Scott

Mail Code ES4
NASA Johnson Space Center
Houston, TX 77058 USA
Phone: 281 483 6643
Fax: 281 244 1301
Email: carl.d.scott@nasa.gov

Samir Farhat

LIMHP
Université Paris 13
Av J.-B. Clément
93430 Villetaneuse, France
Phone: 33 1 49 40 34 18
Fax : 33 1 49 40 34 14
Email : farhat@limhp.univ-paris13.fr

Robert B. Greendyke

Department of Mechanical Engineering
3900 University Blvd
University of Texas at Tyler
Tyler, TX 75799 USA
Phone: (903) 566-7245
Fax: (903) 566-7148
Email: rgreendy@mail.uttyl.edu

Table of Contents

References

§.1 Introduction

The development of processes to produce fullerenes and carbon nanotubes has largely been empirical. Fullerenes were first discovered in the soot produced by laser ablation of graphite [1] and then in the soot of electric arc evaporated carbon [2]. Techniques and conditions for producing larger and larger quantities of fullerenes depended mainly on trial and error empirical variations of these processes, with attempts to scale them up by using larger electrodes and targets and higher power. Various concepts of how fullerenes and carbon nanotubes were formed were put forth, but very little was done based on chemical kinetics of the reactions. This was mainly due to the complex mixture of species and complex nature of conditions in the reactors. Temperatures in the reactors varied from several thousand degrees Kelvin down to near room temperature. There are hundreds of species possible, ranging from atomic carbon to large clusters of carbonaceous soot, and metallic catalyst atoms to metal clusters, to complexes of metals and carbon. Most of the chemical kinetics of the reactions and the thermodynamic properties of clusters and complexes have only been approximated. In addition, flow conditions in the reactors are transient or unsteady, and three dimensional, with steep spatial gradients of temperature and species concentrations. All these factors make computational simulations of reactors very complex and challenging.

This article addresses the development of the chemical reactions involved in fullerene production and extends this to production of carbon nanotubes by the laser ablation/oven process and by the electric arc evaporation process. In addition, the high-pressure carbon monoxide (HiPco) process is discussed. The article is in several parts. The first one addresses the thermochemical aspects of modeling; and considers the development of chemical rate equations, estimates of reaction rates, and thermodynamic properties where they are available. The second part addresses modeling of the arc process for fullerene and carbon nanotube production using 0-D, 1-D and 2-D fluid flow models. The third part addresses simulations of the pulsed laser ablation process using time-dependent techniques in 2-D, and a steady state 2-D simulation of a continuous laser ablation process. The fourth part addresses steady state modeling in 0-D and 2-D of the HiPco process. In each of the simulations, there is a variety of simplifications that are made that enable one to concentrate on one aspect or another of the process. There are simplifications that can be made to the chemical reaction models, e.g. reduction in number of species by lumping some of them together in a representative species. Other simulations are carried out by eliminating the chemistry altogether in order to concentrate on the fluid dynamics. When solving problems with a large number of species in more than one spatial dimension, it is almost imperative that the problem be decoupled by solving for the fluid dynamics to find the fluid motion and temperature history of "particles" of fluid moving through a reactor. Then one can solve the chemical rate equations with complex chemistry following the temperature and pressure history. One difficulty is that often mixing with an ambient gas is involved. Therefore, one needs to take dilution and mixing into account. This changes the ratio of carbon species to background gas. Commercially available codes may have no provision for including dilution as part of the input. One must the write special solvers for including dilution in decoupled problems.

The article addresses both fullerene production and single-walled carbon nanotube (SWNT) production. There are at least two schemes or concepts of SWNT growth. This article will only address growth in the gas phase by carbon and catalyst cluster growth and SWNT formation by the addition of carbon. There are other models that conceive of SWNT growth as a phase separation process from clusters made up carbon and metal catalyst, with the carbon precipitating from the cluster as it cools. We will not deal with that concept in this article. Further research is needed to determine the rates at which these composite clusters form, evaporate, and segregate.

§.2 Reaction Schemes and Thermodynamic Properties

This section deals with the formation of fullerenes and SWNTs via precursor species, clusters of carbon, and metal catalysts. Two basic processes are considered; one being processes that involve carbon vaporized at high temperatures such as the arc process, and the laser ablation process. The other is a gas phase process in which carbon is supplied by carbon monoxide at high pressure, the HiPco process.

§.2.1 Carbon and Fullerene Kinetics

Various workers have studied the kinetics of the formation of carbon clusters. Bernholc and Phillips [3] solved the Smoluchowski equations for carbon clusters C_n up to n=25 using a reaction probability, or kernel, based on a scaled derivative of the Gibbs free energy. Their work included both negative and positive ions, in addition to neutral clusters. Using this technique, they predicted the distribution clusters, including the presence of magic numbers. Creasy and Brenna [4,5] used a simple model in which clusters grew by attachment of only the small clusters C, C_2, and C_3. The reaction rates were estimated from gas kinetic rates. Subsequently, Creasy [6] developed more complex reaction models that allowed for multiple steps, in an attempt to account for "magic number" clusters. His analysis produced cluster and fullerene distributions up to about n=450 that depended on the initial concentration of small carbon molecules. The higher the initial density, the greater was the average size cluster, and the more the distribution shifted toward larger clusters at steady state. The reaction rates in their model did not depend on temperature.

§.2.1.1 **Model of Krestinin and Moravsky**

Krestinin, et al. [7] developed a reaction scheme for fullerene formation. Krestinin and Moravsky [8] applied the model to an arc process, where they achieved reasonable agreement with measured fullerene production, considering the approximations made in the arc flow field. They were able to explain the relatively constant ratio of C_{60} to C_{70} seen in arc experiments. The objective of their model was to depict carbon vapor condensation in an arc reactor. Because of the lack of thermodynamic data for the various clusters, the model was formulated, to the extent necessary, not to rely on that data. Many reactions are written as separate forward and backward reactions, or only in terms of condensation and not decomposition of clusters. They rejected formulating a scheme that includes all carbon clusters, as well as their ions, due to the complexity of experimental verification. As experimental data becomes available and simulations are made, then the model can be validated and rate coefficients and reactions can be refined. Their rates are based on measurements using ionic gas chromatography published in the literature

[9,10,11,12]. Carbon clusters up to n=31 are assumed to be highly reactive chains, cycles, and polycycles. Clusters with n=32 to 79 are closed shells, where the main growth or decomposition is from C_2 attachment or detachment, respectively. That odd-n clusters are less stable than even clusters is attributed to a lack of resonance stabilization. Their model reflects a 251-kJ/mole lower enthalpy of formation of even-n numbered clusters as compared with odd-n numbered clusters. Upon decomposition, odd clusters tend to eject C, rather than C_2 [13]. Clusters with n=80 or greater are assumed to be soot Z. In the calculations of Krestinin, et al. [7] they assumed that soot takes on a size distribution, and that soot reactions are heterogeneous. The reaction rate then depends on the surface area of the soot particle. (In later applications [14] of this model to nanotube production discussed in this article, the model is modified so that soot is treated as a single gas phase species.)

Reaction equations and rate coefficients from [7] are given in Arrhenius form in Table §.1 for the fullerene model.

$$k = A \exp(-E/RT) \qquad (§.1)$$

The thermodynamic properties for these clusters were determined from existing data for C, [15], C_2, [16], C_3 - C_{10}, [17], and C_{60F} and C_{70F}, [18]. The enthalpy of formation for clusters with n=11-59, 61-69, and 71-79 were estimated by interpolating the values between n=10 and 60. The entropy of formation was estimated by interpolation between n=5 and 60. The specific heats were set at values corresponding to T>2000 K where fully excited vibration and rotation is achieved. Then $C_p/R=3n-2$ for $n\geq6$. The complete set of thermodynamic coefficients for the fullerene model is listed in Table §.2. These coefficients are in the old NASA format where the various thermodynamic functions are calculated by the formulas:

$$C_{pi}/R = A_{1i} + A_{2i}\,T + A_{3i}\,T^2 + A_{4i}\,T^3 + A_{5i}\,T^4 \qquad (§.2)$$

$$h_i/RT = A_{1i} + A_{2i}\,T/2 + A_{3i}\,T^2/3 + A_{4i}\,T^3/4 + A_{5i}\,T^4/5 + A_{6i}/T \qquad (§.3)$$

$$s_i/R = A_{1i}\ln(T) + A_{2i}\,T + A_{3i}\,T^2/2 + A_{4i}\,T^3/3 + A_{5i}\,T^4/4 + A_{7i} \qquad (§.4)$$

where R is the universal gas constant, h_i is the specific enthalpy of the i^{th} species, and s_i is the specific entropy. For the clusters for which thermodynamic properties were interpolated, it can be seen from the values in Table §.2, that C_{pi} and s_i are constant with respect to temperature. Thus, they are rather approximate. In most simulations, this does not pose a problem because of dilution. The fully excited approximation for C_p is not very significant due to dilution and the high temperatures used in production of fullerenes and nanotubes. In such case the energy equation for the flow does not depend significantly on the energetics of the carbon reactions.

§.2.1.2 Reduced Carbon Cluster Scheme

Because of the significant computer time required for models containing large numbers of species used in computational fluid dynamic (CFD) simulations, large models are impractical for simulating complex time-dependent flows, such as, pulsed laser ablation. To overcome this limitation of CFD codes it is almost imperative that the number of species in the chemical reaction models be reduced to a manageable number. An effort to do this was accomplished for simulating the HiPco process and likewise for the carbon fullerene and carbon/metal-vapor SWNT processes. Gökçen, et al. [19] showed that in simulations of the flow in the HiPco reactor the number of catalyst particles Fe_n for n>2 could be lumped into a single representative iron cluster Fe_c, and the 200 SWNTs in their model could be reduced to a single representative nanotube, CNT. They compared the production of CO_2 using both models and showed that they produced similar results for a constant temperature case. This enabled Gökçen, et al. to use the model in their simulations of the HiPco reactor, thus saving much computer time. Their full and reduced models will be discussed in more detail later.

In a similar way we have reduced the fullerene model of Krestinin, et al. [7]. In the reduced fullerene model we have lumped all carbon cluster C_n with n>3 into a single representative species CC. For carbon balance in the reaction equations, we specify the number of carbons in CC to be 40. The feedstock for growth of CC and the fullerene C_{60} are the small carbon molecules, C, C_2, and C_3. These small molecules coalesce to form CC, which then forms C_{60}. A soot Z is also formed from CC. This soot is considered a single species of constant n=80. The reduced fullerene model is given in Table §.3, and the corresponding thermodynamic coefficients are given in Table §.4. The thermodynamic coefficients for CC and Z correspond to C_{40} and C_{80} in the full fullerene model. These coefficients were derived from interpolations of properties as indicated above.

§.2.2 Metal Catalyst Schemes

When pure carbon is used as the feedstock for reactions in high temperature processes, the product is usually amorphous carbon chains and rings, fullerenes, graphitic particles, and soot. At some conditions multiwall carbon nanotubes (MWNT) are formed. However, if some metal catalysts are added, there is a preference to form single-wall carbon nanotubes. SWNTs have many interesting and unique properties. They may be metallic or semi conducting, depending on their chirality and diameter. The present understanding of their formation does not allow us to predict from chemical kinetics their relative abundance in a given production process. To these authors' knowledge, no one has developed a chemical kinetics model of particular types of nanotubes. Therefore, in the following models, carbon nanotubes will be treated as a single species, with no consideration of types. At present, there are several concepts of how SWNTs form; but we will consider here only those that depend on gas phase reactions in which metal clusters are involved. It is assumed in this article that gas phase reactions govern the rate of the formation of SWNTs and not diffusion or segregation of carbon from metal catalyst particles.

Metal catalyst clusters are formed from metals vaporized from electrodes in the arc process, from composite targets in laser ablation processes, or from decomposition of metal-containing precursor gases, such as iron pentacarbonyl.

§.2.2.1 Iron Cluster Formation and Evaporation

Several authors have developed the kinetics of iron cluster formation and evaporation. Girshick and his coworkers published a series of articles on iron cluster nucleation and growth [20,21,22,23,24,25,26]. They used modified classical aerosol cluster theory to develop nucleation, growth and evaporation rates. They compared plasma generated iron atom nucleation and cluster evolution with measurements. Their basic equations for the rates of cluster growth are given by the collision frequency. Evaporation is considered as a function of cluster size by accounting for its volume and surface tension. They expressed the net rate of change of iron monomers as

$$\frac{Dn_1}{Dt} = \frac{R}{\rho_g} - \rho_g n_1 \sum_{j=1}^{\infty} \beta_{1j} n_j + \sum_{j=2}^{\infty} \left(1 + \delta_{2j}\right) R_j^e n_j \qquad (§.5)$$

while for dimers and all larger clusters they write

$$\frac{Dn_k}{Dt} = \frac{\rho_g}{2} \sum_{i+j=k} \beta_{ij} n_k n_j - \rho_g n_k \sum_{i+j=k} \beta_{jk} n_j + R_{k+1}^e n_{k+1} - R_k^e n_k \qquad (§.6)$$

In these equations R is the rate of monomer generation/depletion by chemical processes, n_j is the number of j-mers per unit mass of gas, β_{ij} is the collision frequency for i-mers with j-mers, E_j is the evaporation coefficient. Adding the Kronecker delta δ_{2j} accounts for two monomers formed from each dimer. The collision frequency function is taken from ideal gas kinetic theory for the free molecule regime

$$\beta_{ij} = r_1^2 \left[\frac{8\pi kT}{m_i} \left(\frac{1}{i} + \frac{1}{j} \right) \right]^{1/2} \left(i^{1/3} + j^{1/3} \right)^2 \qquad (§.7)$$

The evaporation coefficient is written

$$R_j^e = \beta_{i,j-1} n_s \exp\left(\Theta \left[j^{2/3} - (j-1)^{2/3} \right] \right) \qquad (§.8)$$

where n_s is the equilibrium saturation number density, Θ is a dimensionless surface energy

$$\Theta = \frac{\sigma s_1}{kT} \qquad (§.9)$$

where σ is the surface tension, and s_1 is the surface area of the monomer.

The saturation number density n_s can be calculated using the perfect gas law and the vapor pressure

$$p_s = p_s^o \exp\left(\frac{-E_s}{kT} \right) \qquad (§.10)$$

where p_s^o is the coefficient of the vapor pressure expression.

Rate coefficients for gas phase kinetics can be derived in Arrhenius form from these expressions for β_{ij} and E_j. The evaporation rate coefficient can be expressed as

$$k_j = A_j T^{-1/2} \exp\left(-\frac{E_j}{kT} \right) \qquad (§.11)$$

where

$$E_j = \left(\sigma s_1 \left[j^{2/3} - (j-1)^{2/3} \right] - E_s \right) \qquad (§.12)$$

and

$$A_j = r_1^2 \left[\frac{8\pi}{m_i} \left(\frac{1}{i} + \frac{1}{j} \right) \right]^{1/2} \left(i^{1/3} + j^{1/3} \right) \frac{p_s^o}{k} \qquad (§.13)$$

The rate coefficients developed from this analysis were published for iron clusters in [27].

§.2.3 *High Pressure Carbon Monoxide Disproportionation (HiPco) Models*

The high-pressure carbon monoxide (HiPco) process begins with iron pentacarbonyl diluted in carbon monoxide. This mixture is injected at near room temperature into a high temperature reactor, where it mixes rapidly with hot carbon monoxide. As the temperature increases above about 600 °C, $Fe(CO)_5$ decomposes into FeCO and Fe, which then react to form dimers of iron. These iron dimers coalesce with iron atoms and other dimers to form Fe_3 and Fe_4. Coalescence continues and larger and larger clusters of iron are formed.

For modeling the HiPco reactor, Dateo, et al. [28] adopted the rate coefficients of Krestinin, et al. [29] for iron cluster condensation and evaporation. These coefficients are based on assumptions, such as, clusters up to n=4 are considered to be in the gas phase, above that they are considered to be condensed phase with rate coefficients for reactions with smaller clusters having reached their asymptotic limit. Evaporation is assumed to be negligible for clusters larger than n=9; and condensation and growth of iron clusters occurs mainly through reactions with Fe_4 and smaller clusters. The rate coefficients that they used were developed through considerations of the dependence of equilibrium constants on the formation energy and standard reduced thermodynamic potential. They accounted for the collision frequency and its dependence on size when computing the rate coefficients for cluster growth. These reactions and rates from [29] are given in Table 5.

After Krestinin, et al. [29] published their results for iron cluster chemistry, Vlasov, et al. [30] developed rate coefficients for iron cluster kinetics that takes into account nonequilibrium effects associated with the difference between the gas temperature and the internal temperature of the iron clusters. They made their calculations of decomposition of clusters within the framework of the statistical theory of unimolecular reactions, in which they treated only the attachment and detachment of monomers. The nonequilibrium effects are manifested by depletion of internal energy by detachment and gain of internal energy by attachment of monomers. Nonequilibrium effects are seen most vividly for clusters up to n=20. After that, there seems to be a smooth variation in the equilibrium constant and rate coefficients. They plotted their equilibrium constants, decomposition rate coefficient, and recombination coefficients as functions of cluster size for temperatures from 1000 K to 3000 K in Figs. 3, 4 and 5, respectively, of their article [30]. One present author (CDS) curve fit these figures and obtained Arrhenius expressions for the rate coefficients. These coefficients for n<51 are given in Table §.6 5. For n>50 the constants in these expressions can easily be extrapolated. A comparison of evaporation rate coefficients at T=1380 K is given in Fig. §.1; and recombination coefficients at T=1500 K are given in Fig. §.2. It is apparent there is a strong influence nonequilibrium effects associated with atom attachment and evaporation (Vlasov), particularly for small clusters. The recombination rates of Girshick, where classical gas kinetics governs attachment, are probably overestimated for small clusters.

§.2.3.1 **Decomposition of $Fe(CO)_5$**

There are several sources of reaction rates for $Fe(CO)_5$ decomposition. Krestinin, Smirnov, and Zaslonko [29] included a two-step decomposition scheme when simulating the decomposition of $Fe(CO)_5$ and the condensation of Fe. Their decomposition reactions are:

$$\mathrm{Fe(CO)_5} \rightarrow \mathrm{FeCO} + 4\mathrm{CO} \tag{\S.14}$$
$$\mathrm{FeCO} + \mathrm{M} \rightarrow \mathrm{Fe} + \mathrm{CO} + \mathrm{M} \tag{\S.15}$$

The rate coefficient for (§.14) was taken from [31]. They inferred the rate coefficient for (§.15) from the shock tube data. Their complete reaction set is given in Table §.7 6. Note that the formation of dimers in their scheme is allowed by the reactions

$$\mathrm{FeCO} + \mathrm{FeCO} \rightarrow \mathrm{Fe_2} + 2\mathrm{CO} \tag{\S.16}$$
$$\mathrm{FeCO} + \mathrm{Fe} \rightarrow \mathrm{Fe_2} + \mathrm{CO} \tag{\S.17}$$

Since FeCO can react to form Fe_2, the direct nucleation of Fe_2 from two Fe atoms is not required. Due to the nature of the closed shell electronic structure of Fe it is unlikely that two ground state atoms are likely to form Fe_2. It probably requires one or both atoms to be in excited states to achieve Fe recombination [27]. The rate coefficient for the reaction

$$\mathrm{Fe} + \mathrm{Fe} + \mathrm{M} \rightarrow \mathrm{Fe_2} + \mathrm{M} \tag{\S.18}$$

given in Table §.5 6, was inferred from shock tube data. Since formation of iron clusters is very rapid in the shock tube experiments, it is possible that reactions (§.16) and (§.17) dominate. This was discussed in [27].

Smirnov inferred iron pentacarbonyl decomposition rates from shock tube measurements [32] of absorption spectrophotometry of Fe atoms and parent molecules. Vlasov, et al. [33] included them in a review of metal compound decomposition. However, there was a difference in the $Fe(CO)_5$ decomposition rate of one order of magnitude. It is not clear which rate is correct. Rumminger, et al. [34] compiled a set of reactions for the inhibition of flames by iron pentacarbonyl. They included recombination reactions from Seder, Ouderkirk, and Weitz [35]. Using more recent bond energy measurements from Sunderlin, et al. [36] and accurate *ab initio* calculations of Ricca [37], Dateo, et al. [28] calculated the equilibrium constants for decomposition/recombination reactions of $Fe(CO)_n$. With the association rates of Seder, et al. [37] they calculated the dissociation rates that are denoted "Ames" in Table §.7. Since, the HiPco reactor that they modeled is at many atmospheres pressure, they did not give rate coefficients for the low-pressure fall off regime. Rate coefficients for the iron carbonyl dissociation reactions of Smirnov [32] are also given in Table §.7 6.

Iron clusters are formed from FeCO and Fe combining and agglomerating. Krestinin, et al. [29] developed a set of iron cluster reactions and thermodynamic data. Their reactions and rate coefficients are given in Table §.5. They contend that due to low pressure, FeCO decomposition is controlled by the bimolecular activation step. Thus, the rate of decomposition of FeCO is commensurate with the reactions

$$\mathrm{FeCO} + \mathrm{FeCO} \Rightarrow \mathrm{Fe_2} + \mathrm{CO} + \mathrm{CO} \tag{\S.19}$$
$$\mathrm{FeCO} + \mathrm{Fe} \Rightarrow \mathrm{Fe_2} + \mathrm{CO} \tag{\S.20}$$

Because of this, Fe_2 and larger clusters are produced in large quantities during FeCO decomposition. Therefore, it is not necessary that direct formation of Fe_2 nucleation occur via Fe-atom recombination. Further growth of iron clusters is dominated by coagulation of these clusters. Evaporation of small clusters was estimated based on classical theory. However, These rates did not lead to good agreement with measurements. Therefore, they were adjusted as given in Table §.5. The original rate coefficients are given in parentheses.

§.2.3.2 **CO Attachment to Iron Clusters**

In the development of the model for the high-pressure carbon monoxide reactor Dateo, et al. [28] assumed that CO attaches to iron clusters beginning at Fe_{10}. There is some data [38,39] that suggests that CO will attach to smaller clusters and may attach to larger clusters in greater numbers. However, multiple bonding of CO probably does not alter significantly the rate of production of carbon nanotubes (Boudouard reaction). To keep their model simpler, only Fe_nCO are considered for n>9 and no multiple attachments of CO to the clusters. This reaction forms the first of a three-step model for the production of carbon nanotubes.

§.2.3.3 **Formation of Carbon Nanotube Reactions**

The second of the three steps for the formation of carbon nanotubes in the Dateo model is detachment of CO from Fe_nCO. The final step is the conversion of Fe_nCO to a carbon nanotube.

$$\mathrm{Fe}_n\mathrm{CO} + \mathrm{CO} \rightarrow \beta\mathrm{Fe}_n\mathrm{C}_{\mathrm{NT}} + \frac{1+\beta}{2} CO_2 + (1-\beta)\mathrm{Fe}_n\mathrm{CO} \qquad (\S.21)$$

where $\beta=1/(2n_{NT}-1)$ and n_{NT} is the average number of carbon atoms in a carbon nanotube formed in $Fe_n{\cdot}C_{NT}$. In the calculations of Dateo, et al. [28], they let $n_{NT} = 3000$. In the calculations of Scott, et al. [27], they let $n_{NT} = 999$ due to a limitation in the input format of CHEMKIN® [40].

§.2.3.4 **Inerting or "Death" of Clusters**

Daniel Colbert of Rice University suggested by that carbon nanotubes stop growing due to lack of iron clusters or due to carbonizing of the iron cluster to which the nanotube is attached during growth. Iron clusters may become over coated with carbon that blocks the formation of nanotubes. This results in their "death" as a useful catalyst; and nanotube growth stops. To account for this possibility, the following two types of reactions are included in the Dateo model

$$\mathrm{Fe}_n \rightarrow \mathrm{Fe}_n^{*} \qquad (\S.22)$$

$$\mathrm{Fe}_n\mathrm{C}_{\mathrm{NT}} \rightarrow \mathrm{Fe}_n^{*}\mathrm{C}_{\mathrm{NT}} \qquad (\S.23)$$

Fe_n^* and $Fe_n^*C_{NT}$ are clusters and nanotubes that have been poisoned with carbon to the extent that they cannot catalyze the reactions and cease to grow. The HiPco reaction model of Dateo, et al. [28] is summarized in Table §.8.

§.2.3.5 **Reduced HiPco Model**

The full model of Table §.8 is very large, having 971 species and 1948 reactions. To simplify the model and make it useable in a 2D CFD code, Dateo, et al. [28] collapsed or lumped all the iron clusters having n>2 into a single representative cluster Fe_C. They also collapsed the other clusters as well, leaving the following fourteen species: iron carbonyls ($Fe(CO)_5$, $Fe(CO)_4$, $Fe(CO)_3$, $Fe(CO)_2$, and FeCO), CO, CO_2, Fe, Fe_2, Fe_C, Fe_CCO, Fe_CC_{NT}, Fe_C^*, and $Fe_C^*C_{NT}$. Their reduced model, listed in Table §.9, has only twenty-two reactions.

§.2.4 Carbon Vapor Models of Carbon Nanotube Formation

Carbon vapor models are required for processes that start from vaporized carbon such as in laser ablation processes and the arc vaporization process. These processes, and how these models can be applied to them, are described in more detail in the subchapters of this chapter. Single wall carbon nanotubes require a feedstock of carbon vapor plus vaporized metal catalysts. From this feedstock clusters of carbon and nickel condense to form SWNTs and impurities, such as soot and carbon-coated metal clusters. The general concepts of SWNT formation fall into two or three categories. In order to form carbon nanotubes it is necessary for the carbon to be catalyzed by nickel and other metals. Nucleation and growth of carbon nanotubes are not well understood; and there are many possible scenarios for carbon and nickel to condense in a reactor and then to grow nanotubes. An early scheme, called the "scooter mechanism" was envisioned by Smalley's group at Rice University. In it, carbon was envisioned to form fragments of graphene sheets that would tend to close into fullerenes. However, nickel or other metal catalyst atoms would attach to an open edge of the carbon cluster and "scoot" or move around, holding open the end of the tube, while small carbon clusters, e.g. C_2 would attach to the nascent nanotube that would continue to grow. In this scheme, carbon would condense first, then nickel would tend to agglomerate until a cluster of nickel at the end of the nanotube are so large as to soot up and cease to allow the nanotube to grow; or the metal cluster would detach from the nanotube, thus ending its growth. This scenario is supported by the observation that laser ablation nanotubes are almost never seen attached to metal clusters. It also conforms to the tendency for carbon to agglomerate first, followed by nickel, due to the stronger carbon-carbon bond and to the higher concentration of carbon than catalysts.

Another scheme that has much support involving vaporized carbon in SWNT production is one in which metal catalysts are envisioned to form along with carbon with the clusters at high temperature. As the mixture cools, carbon precipitates out of the cluster and the energetics and geometry favor the formation of nanotubes. This is essentially a phase change phenomenon due to cooling of a mixture, especially eutectic mixtures of nickel, cobalt, and carbon. This scheme is supported by the observation that the ends of nanotubes, particularly bundles, are sometimes seen attached to metal clusters. Some clusters are seen to have a number of bundles attached in sort of a "sea urchin" pattern. See Fig. §.3, [courtesy of Alexander Moravsky, MER Corp.] and Fig. 4 from [41].

§.2.4.1 Nickel Cluster Nucleation and Growth

Nickel is used as a catalyst in both the laser ablation process and the arc vaporization process. Other metal catalysts that are commonly used are cobalt and yttrium. Since cobalt is a neighboring transition metal it has similar properties to nickel. Yttrium properties are less well known. For these reasons, only nickel will be discussed here. To assess why nickel did not produce nanotubes in the HiPco reactor, Scott and Smalley [42] tested the effect of the diatomic bond energy and the bond energy of nickel atoms with CO. The bond energy of Ni to Ni is larger than that of Fe to Fe and also, the bond energy between CO and Ni is larger than between CO and Fe. To assess the effects of bond energies, simulations of the HiPco reactor were made using each metal as catalyst. To do the nickel catalyst simulation, it was necessary to create agglomeration and evaporation rates for nickel. The Girshick technique described in equations (§.7-§.13) was used. The surface tension was adjusted until the activation energy for E_1 equaled the

Ni_2 bond energy. The activation energy for NiCO was set equal to its corresponding bond energy.

In principle, more accurate evaporation rate coefficients for small n can be calculated from the cross section data of Amentrout's group [43,44]. They measured the dissociation of Ni atoms and small clusters from nickel clusters from n=2 to 18 in a crossed beam apparatus in which they obtained collisions of the nickel clusters ions with xenon. They corrected their data for internal energy (pressure) effects; and they also suggested the following simple equation to fit their data.

$$\sigma(E)=\frac{\sigma_0\left(E-E_i-E_0\right)^N}{E} \tag{§.24}$$

where N and σ_0 are adjustable parameters, E is the relative kinetic energy, E_i is the internal energy of the cluster, and E_0 is the collision induced dissociation threshold energy. This provided an accurate and convenient formula for calculating rate coefficients from the expression

$$k_e=\frac{4}{\pi}\left(\frac{\mu}{2kT}\right)^{\frac{3}{2}}\int_0^{\infty} v^3 \exp\left[\frac{-\mu v^2}{2kT}\right]\sigma(v)dv \tag{§.25}$$

where k_e is the evaporation rate coefficient, μ is the reduced mass, $v=\sqrt{2E/\mu}$ is the relative velocity, and $\sigma(v)$ is the collision cross-section as a function of relative velocity. The main difficulty with this method is the need for the internal energy, which is not known for many clusters.

Because of the large number of possible nickel clusters, there seemed to be a need for reducing the model in some way. The option chosen [42] was to lump clusters greater than n>8 into sizes 16, 32, … 2048. We call this the "binary" model. Evaporation equations for these clusters are written

$$Ni_n \rightarrow Ni_{n/2} + n/2\ Ni \tag{§.26}$$

which, in an approximate fashion, accounts for the nickel clusters not included in the model. Agglomeration rates for all nickel clusters and evaporation rate coefficients for n≥16 were determined from Girshick's method, equations (§.7-§.13). These evaporation coefficients are given in Table §.10a; and the agglomeration coefficients are given in Table §.10b. The rate coefficients for n≥16 have been multiplied by n to account for the missing clusters between each n and 2n.

§.2.4.2 Combined Carbon and Nickel Clusters to Form Carbon Nanotubes

One kinetics model that takes advantage of the fullerene model of Krestinin, et al. was proposed by Scott [14]. The nickel model of Scott and Smalley [42] is added to the set of reactions for carbon to produce fullerenes and other large carbon clusters is. Carbon and nickel clusters combine to form the nuclei for the growth of carbon nanotubes. The rates of nickel cluster formation and growth are as discussed previously, the growth of the combination carbon/nickel clusters can be obtained from the aerosol theory of Girshick as given in equation (§.7). Carbon clusters in the form of soot Z, and fullerenes C_{60} and C_{70} are assumed to be the precursors that combine to form nickel/carbon clusters, ZNi_C and $CFNi_C$. These clusters are the species that nucleate and grow nanotubes CNT. These reactions are given in Table §.11. For specificity, soot is assumed to have 80 carbon atoms, while ZNi_C is assumed to have 80 carbon atoms and

1024 nickel atoms. CNT is assumed to have 999 carbon atoms. Whereas, this is much fewer than in actual nanotubes, it can represent them; and the number of them will be correspondingly larger. The number 999 is purely arbitrary and can be selected to be something greater. However, in [42] it is chosen because the computer code used to solve the kinetic rate equations has a three-digit limit in the input format for number of atoms in the species definition.

§.2.4.3 Reduced Combined Carbon and Nickel Cluster Nanotube Scheme

As we saw in the reduced HiPco model, we can attempt to reduce the number of species and reactions by lumping most of the metal clusters as well as carbon clusters into representative clusters. Both active and inert (dead) clusters that combine the catalyst and carbon can also be lumped together into a single representative clusters. The species in this reduced model are Ar/He, C, C_2, C_3, C_C, Z (soot,) C_{60F}, Ni, Ni_2, Ni_3, Ni_C, ZNi_C, DZ, and $DZNi_C$. The subscript C on these symbols denote "cluster." The "D" on the symbol indicates a dead particle that no longer reacts. As in the reduced HiPco model and the reduced fullerene model, we the representative lumped clusters have specified numbers of atoms each, just for the specificity required to satisfy element balance in the reaction.

Reaction rate coefficients may have to be adjusted slightly to make the results agree with those of the full model. This can be attempted by solving the problem parametrically, using a simple temperature and dilution profile that is representative of a given reactor or process. The reduced model for SWNT production based on carbon vapor and metal catalysts is given in Table **§.12.** Nickel is the metal chosen because it is most often used.

§.2.4.4 Results Comparing Full and Reduced Fullerene Models

To assure that a reduced model actually is capable of predicting the production of nanotubes one can calculate both models for some representative simple cases such as a temperature profile linear in time. A comparison of the complete Krestinin, et al. [7] model with the reduced fullerene model was presented in [14]. The time evolution of a carbon/nickel vapor from 3500 K to 1500 K was calculated using a zero-dimensional code (AURORA code of CHEMKIN® package [40]) for both models. The calculation of the production of carbon nanotubes and other clusters agree very well. Figs. §.5 and §.6 show comparisons of the time evolution of various species and the production of SWNTs. Whereas, the comparison is very good (within no more than 50%) the production of carbon nanotubes and other clusters must be compared with experiment to calibrate the rate coefficients used in the models.

The models discussed in section §.2 have been applied to various problems associated with the production of carbon nanotubes. The application of these models has taken various levels of fidelity and sophistication. Assessments of the models, particularly comparisons between full and reduced models are given in this section. Section §.3 contains results applied to the arc process, section §.4 addresses laser ablation process results, and §.5 deals with the HiPco process. Two approaches are considered for solving the coupled fluid dynamics equations and the chemical kinetics of the models. Since complete fluid dynamics in three dimensions plus large models having hundreds of species presents a formidable computational task, we approach the solution by simplifications of two types. One is to reduce the size of the model by lumping many clusters into a single representative cluster, as in the "reduced" models. One can then use these reduced models in highly complex geometrical situations using multidimensional fluid dynamics equations. On the other hand, if high fidelity of chemical species and reactions is desired, then the chemistry and fluid dynamics solutions can be decoupled. The fluid dynamics equations are solved without chemical reactions; and then the complex chemical kinetics is developed along streak lines.

§.3 **Analysis and Modeling of Carbon Arc Reactors**

The arc discharge, developed initially for fullerene synthesis [2], can also produce single walled carbon nanotubes (SWNT) [45,46,47,48], by simply adding catalysts to the graphite and by changing process conditions. Compared with other synthesis techniques, the arc leads to temperatures higher than 5000 K, as measured by optical emission spectroscopy [49,50,51], thus insuring total and fast vaporization of graphite anode containing bimetallic catalysts in a background gas of helium, [46] argon [46, 52], or mixtures of them [52, 53]. Catalysts that are commonly used are nickel and yttrium at about one to four molar percent [46]. Optimal conditions are obtained with this catalyst composition [46], for helium at a pressure of 660 mbar, and a current of 100 A. Nanotubes are collected in a soot, called "collaret," that is close to the cooled cathode. They seem to grow either in bundles or as individual tubes that coalesce readily into bundles. Laboratory scale reactors can produce up to one gram of this collaret per 10-minute batch run. The as-produced material contains nanotubes that are 1 to 1.4 nm in diameter and a few micrometers in length. Due to its relatively low cost, the arc discharge process is used to produce nanotubes industrially. Although prices are still high, they are in constant decrease. For example, the MER Corporation in the United States offers a soot synthesized by the electric arc method (**Fig. §.7**) that contains 10 to 40% by mass of nanotubes at $50 per gram, compared with $2000 per gram a few years ago! Contrary to the competing process by chemical vapor deposition CVD in fixed [53,55,56,57,58,59] or fluidised beds [60,61], nanotubes produced by arc are reputed to have excellent structural properties. They are quite straight and present fewer topological defects, probably because of the fast growth conditions. However, the major inconvenience of the arc process remains the presence of impurities such as catalysts and amorphous carbon mixed with the nanotubes. To take advantage of the good structural quality of nanotubes produced by arc, two solutions are possible. The first concerns the development of post-synthesis purification methods to remove these impurities. However, due to the large variety of carbon impurities (**Fig. §.8**), such as amorphous carbon, graphitic nanoparticles, polyhedral carbon particles, onions, single wall nanohorns (SWNHs), fullerenes, and some other forms of carbon with metal catalyst enclosed, purification is a very tedious task and no purification technique is universally admitted today. In addition, this large variety of impurities renders the quantitative techniques developed to measure the amount of carbon nanotubes in the sample such as thermogravimetric analysis (TGA) or near-infrared (NIR) spectroscopy [62] not very reproducible. For these reasons, it is better to improve the process to increase nanotube yield during their formation. Hence, many experimental and theoretical studies have attempted to improve nanotube yield during arc synthesis, and to provide a comprehensive understanding of the growth mechanism. For the future, there is an important challenge for scaling up, optimizing, and controlling the arc process to make it commercially viable. To perform these objectives, several experimental approaches were developed to study the effect of the different arc parameters on nanotube yield and structure. These studies were also complemented by several models, either phenomenological, to understand how and where nanotubes are formed, or macroscopic to understand such processes as mass and heat transfer in the arc and their interconnection. When implemented into computational fluid dynamics CFD numerical codes, these models can predict temperature, species distribution, and fullerene yield or nanotube growth rate. In this section, we will summarize first the experimental approaches used to enhance fullerene or nanotube yield in the arc. Then, by a comparative survey of all synthesis processes, we will point out the specificity of the arc. Phenomenological models, as well as macroscopic multi-dimensional models at 0D, 1D, and 2D will be presented. These models were developed to predict the temperature and chemical species distributions, fullerene yield or nanotube growth rate.

§.3.1 Review of the Arc Process

Several laboratory-scale methods have been proposed to produce SWNTs. Examples include condensation of laser [63,64] vaporized carbon in the presence of catalysts, decomposition of hydrocarbons on supported [54-56], entrained [65,66,67,68] or fluidized bed catalysts, [59,60] decomposition of carbon monoxide on supported catalysts [58] and a high-pressure technique called HiPco. This technique involving decomposition of carbon monoxide on gas phase metallo-organic carbon pentacarbonyl $Fe(CO)_5$ was developed more recently by Smalley's group at Rice University [69,70]. Compared with these processes, the unique aspects of arc synthesis are the presence of the ions in the discharge and the formation of catalysts atoms and small carbon clusters C and C_2 at relatively high temperature. After giving a brief history of the arc, we will present in this section the uses of arc technique to produce carbon materials as fullerenes, multi-walled or single-walled carbon nanotubes. We will discuss in more detail the specific conditions of single-wall carbon nanotube formation.

§.3.1.1 History

Sir Humphry Davy of London, England discovered the electric arc between two carbon electrodes in 1813. In 1844, the French physicist Léon Foucault studied physical phenomenon in the arc lamp. The first industrial use of the arc was achieved in 1862 to produce acetylene by a process developed by Marcellin Berthelot. In 1880, Louis Clerc replaced the oxygen flame for welding applications by the plasma of an electric arc. At the end of the 19th century, carbon arc welding (CAW) was intensively used for locomotive maintenance because of the weld joints were hard and brittle due to the carbon flaking off into the weld puddle [71]. Since 1944, these discoveries opened the way to the thermal plasma synthesis of carbon materials.

The German physicist, Otto Hahn, obtained carbon chains when trying to create some heavy atoms by fixing neutrons during the evaporation of metals in a carbon arc. Harold Kroto and Dave Walton also observed these chains in 1970 during experiments simulating conditions of combustion in the formation of red giant stars. In 1990, fullerene synthesis was performed by Krätschmer et al. [2] (**Fig. §.9**) of the Max Planck Institute in

Heidelberg, Germany under a helium atmosphere. One year later, in 1991, nanotubes were observed for the first time by S. Iijima [72,73,74,75] of the Japanese company, NEC, and by Bethune et al. [76] Due to their unique combination of properties, nanotubes generated a lot of interest in the scientific community, and opened new fields of studies in science and technology. Since 1991, nanotube synthesis in the arc has been extensively developed and studied by several research teams around the world.

§.3.1.2 Experimental approaches

Before presenting the different modelling approaches, we will briefly discuss the experimental approaches used to improve fullerene and nanotube arc processes.

§.3.1.3 Fullerenes vs. multi-walled carbon nanotubes

When the electric current is changed from direct (DC) to alternating (AC) current, nanotubes instead of fullerenes are formed in a deposit on the cathode. Hence, the arc discharge technique, first used to produce fullerenes [2] was then extended to producing multi-walled carbon nanotube [2,77] synthesis by changing the conditions of the discharge in the same apparatus. **Fig. §.8** illustrates ideal structures obtained in the soot. Multi-walled carbon nanotubes are formed inside a hard deposit that grows on the cathode at a speed of about 1 mm/min. They are organized in bundles with diameters between 2 and 30 nm [72,77,78]. Ebbesen et al. [45] and Ajayan and Iijima [77] proposed improvements in the classic process of Krätschmer and Huffmen. These studies showed that optimal growth conditions are different from of those of fullerenes. For example, the total pressure of helium is 660 mbars for nanotubes and only 200 mbars for fullerenes. The physical reason of this difference remains not very elucidated. Among the limited number of publications on this topic, we notice Zhang et al. [79] work on the effect of the helium pressure on the MWCNT yield. They indicated that the increase in pressure enhances nanotube yield and decreases fullerene formation. Cadek et al. [80] reported a pressure of 660 mbar and a current density of 195 A/cm^2 as optimal conditions for MWCNT synthesis. Nanotube synthesis under an argon atmosphere was studied by Borisenko et al. [81] who showed that argon can improve MWCNT yield by a factor of 5-10 compared to helium in similar arc discharge conditions. A hydrogen discharge was also tested by Ando et al. [82] and Zhao et al. [83] to grow nanotubes with smaller diameters. Double walled carbon nanotubes were produced using a mixture of argon and hydrogen by Hutchison et al. [84] Finally, Jung et al. [85] Tang, et al. [old 42 not Tang] ???studied the morphology and the structure of MWCNT produced in a mixed atmosphere of helium and acetylene in the arc. They noticed that the quantity of carbon nanoparticles, formed inside the cathodic deposit, increases when acetylene is added to the ambient gas. An important modification of the arc method was achieved using liquid nitrogen [85,86] with the advantage of an easier recuperation of the products and a possible continuous synthesis. Another less efficient, but also less expensive method, uses water instead liquid nitrogen [87].

§.3.1.4 Single-walled carbon nanotubes

Single-walled carbon nanotubes were discovered by Iijima [71] in 1991 when adding iron to a graphite anode in the arc. Later, all the process parameters such as catalysts and inert gas composition, current density, pressure, gravity, etc. were varied to enhance nanotube yield. Several metallic particles were used as catalysts including cobalt [76], nickel [89], yttrium [90], manganese [91], scandium [92], lanthanum [92,93] vanadium [94], cerium [95], gadolinium [96],[52] and zirconium [90[49]]. The presence of these catalysts leads to a large variety of metallic particles and carbides in the plasma and in the collected material. Currently, the most efficient catalyst is obtained by mixing two elements such as nickel-yttrium [46,97], nickel-cobalt [98.99], iron-nickel, [100,101] or rhubidium-platinium [102]. According to Saito et al. [102], the efficiency of the Rh-Pt couple is comparable to Ni-Y. It is also noticed that these catalysts can change the diameter distributions in the interval 0.7-3 nm. On the other hand, Sugai et al. [103] used a pulsed discharge to synthesize fullerenes and SWNTs using nickel and cobalt catalysts under an inert atmosphere of helium, argon, or krypton. Argon was found to be the best gas for fullerene production and krypton the most efficient for nanotubes. According to the authors, increasing the pulse duration increases nanotube and decreases fullerene yields, making a competition between these two kinetic pathways. The conventional electric arc is an unsteady process because of instabilities of cathodic spot. This leads to a non-homogeneous distribution of the electric field in the plasma. The cathode spot instability results in random and erratic motion of a luminous spot along the cathode surface. Hence, Lee et al. [104] used a technique of rotation of the anode to create uniform plasma. This rotation generated a turbulence that accelerates carbon species perpendicularly to the anode. In this situation, carbon is not condensed on the surface of the cathode but collected on a graphite collector placed in the periphery of the plasma. According to the authors, increasing the speed of rotation increases nanotube yield and decreases nanotube diameter. This result was confirmed by Bae and al. [105] Effects of gravity have been studied by Kanai and al. [106] who found that the absence of gravity forces can reduce convective fluxes of the inert gas increasing plasma volume. Consequently, the authors found an increase of the yield of nanotubes and an increase of their diameter. A key parameter for the arc is the erosion rate of the anode. This parameter depends on the input power, the chemical composition of the anode, the length of the arc, and the nature of the inert gas, the pressure, the cooling of electrodes as well as the geometry of the reactor. Not all these parameters are independent, increasing the complexity of the problem. Therefore, Zhang et al. [107] studied the dependence of the speed of erosion of the anode with the pressure and the nature of the inert gas (argon or helium). The authors found that for low pressures between 100 and 300 mbars, the erosion rate of a pure graphite anode is lower in argon than in helium. This tendency is reversed for pressures between 300 and 900 mbars. Takizawa et al. [108] measured the quantity of soot formed in the reactor while varying the percentage of nickel and yttrium in the composition of the anode. They demonstrated that the addition of yttrium traces (0,1% at.) with the nickel increases soot yield by a factor of 2-3. This yield was not important when only nickel or yttrium has been used as catalyst.

§.3.2 Analysis of the Arc Discharge

§.3.2.1 Description of the experiment

The carbon arc apparatus consists of a static water-cooled reaction chamber with two cooled graphite rods. For the anode, a graphite rod filled with catalysts (Co, Fe, Ni, Y) is generally used. The cathode is made of pure graphite or copper. It was reported that copper does not improve the results and leads to a less stable arc [109][65]. The distance between the anode and the cathode can be adjusted by moving the anode toward the cathode manually [46,52] or automatically [49] using an optoelectronic system. A direct current (DC) for nanotube synthesis or alternating current (AC) for fullerene production passes through the electrodes; and plasma is created in the inter-electrode region. Efficient operation is assumed to exist when the discharge is stable and the anode erosion rate is constant. This can be achieved by maintaining a constant voltage between the electrodes, which is closely related to the stability of the electrode spacing. The plasma is first ignited by contact between the anode and the cathode, which elevates the temperature of the contact point until evaporation of the anode material. Then, the anode is moved back to maintain a desired gap between the growing deposit on the cathode and the burning anode. An active plasma zone bounded by the deposit and the anode is created. This hot plasma zone produces carbon and catalyst vapors, which then diffuse to the cooled reactor regions. Carbon species and catalysts build up on the end of the cathode (called cathode deposit) and deposit forms a collaret around the cathode deposit. Soot is deposited on the reactor walls by free convection. The high temperature near the anode and the high energy density in the plasma insure vaporization of most of the anode material. The water-cooled cathode leads to high quench rates and high levels of super cooled or supersaturated vapor with nanotube formation. The quench process is uncontrolled, but arc products usually are: soot on the reactor walls, web-like structures between the cathode and the chamber walls, a hard gray deposit at the cathode's end, and a rubber-like collaret rich in nanotubes around this deposit. **Fig. §.10** Figure 4 shows SEM and HRTEM micrographs of as-produced nanotubes.

§.3.2.2 Comparison with the high temperature processes

The nanotubes produced by arc discharge are similar to those obtained at high temperature process as laser or solar vaporization; and it is interesting to compare all these processes to point out the specificity of the arc. In high temperature processes, the temperature is higher than 3500 K, permitting the total vaporization of the target or anode formed by graphite and catalyst. To achieve such high temperatures, high energy densities are needed to totally atomize the solid and to form atoms of carbon C and catalyst M. When the temperature decreases in the cold region of the reactor carbon reacts to form molecules of superior size and clusters composed only of carbon, such as C_2, C_3… C_{60}… CNT…, soot or composed of only metal as M_2, M_3, …, $M_{cluster}$ or, finally, a mixture of them C_nM_m. To understand these processes, it is necessary to quantify mass and energy fluxes at different conditions. In Table §.131, a comparison of fluxes of mass and energy for the most important high temperature processes is given. In this table, I and V are respectively the current and potential drop between electrodes, r_A is anode radius, d_{AC} is the distance between anode and cathode, P the pressure, λ is the laser wave length, ν the frequency of the laser, E_{pulse} is the pulse energy, t_{pulse} is the duration between two pulses and Φ is the laser or solar spot diameter. We notice that the arc process is by far the most efficient process in terms of erosion rate and produces 4.2 g/h of soot containing nanotubes. Nevertheless, for industrial applications, arc processes have at least two disadvantages. (1) This process is discontinuous and requires cycles of production/cleaning. (2) The nanotube concentration in the soot is relatively poor.

§.3.3 Specificity of the arc

§.3.3.1 Specific conditions for SWNT growth

Typical experimental conditions [110] for SWNT synthesis in the arc are the following:

(i) The inert gas is helium.
(ii) The potential drop between the electrodes is V= 40 V.
(iii) The anode diameter r_A=3 mm and the cathode diameter r_C= 16 mm.
(iv) The current density j = 100-350 A/cm^2.
(v) The interelectrode distance d_{AC} = 1-3 mm
(vi) The plasma temperature ~ 6500 K.
(vii) The erosion rate 70 g/h.
(viii) The pressure 660 mbar.
(ix) The velocity of material leaving the anode as calculated by Farhat, et al. [107[66] u_{anode}=78 m/s and estimated by Krestinin and Moravskii [7,111], u_{anode}=2-80 m/s for fullerene conditions.
(x) The dilution factor τ describing how much time the carbon material leaving the interelectrode space is mixed with helium. τ=20-30. [7,111]
(xi) Mixing time τ_{mix} is a parameter introduced by Krestinin and Moravskii [7,111] to measure the time that carbon material needs to be totally mixed with helium when leaving the interelectrode space: τ_{mix}=2-8 ms [7,111].

Other parameters such as water flow-rate used to cool the cathode and loss by radiation from the plasma are reported in the literature [112,113]. Gamaly and Ebbesen [114] proposed to estimate gas radiation simply from Stephan-Maxwell equation $Q_{rad} = \sigma T^4 = 5.67\times10^{-12}$ T^4 J/cm^2 s K^4 with T~ 4000 K. However, arcs are not usually optically thick. Therefore, this is not a good assumption.

§.3.3.2 Space charge, potential and electric field distribution

Space charge, potential, and electric field distributions have been described by Gamaly and Ebbesen [114] for multi-walled carbon nanotube conditions. According to them, the space distribution of the potential has a steep drop near the cathode in a region of positive space charge where practically the entire potential drop occurs as showed in **Fig. §.11**. They calculated this sheath length at Δ=12 μm for typical multi-walled carbon nanotube conditions with V=20 V and j=150 A/cm^2. This is also the distance of the main potential drop in the interelectrode region. Gamaly and Ebbesen [114] also estimated the average electric field in this region at $E=2\times10^4$ V/cm and consider that the electric field in the outer region is several order of magnitude lower.

§.3.3.3 Ionisation state and density of the plasma

The interelectrode region is composed of a mixture of inert gas, carbon and catalyst atoms and molecules. **Fig. §.12** shows qualitatively 15 pictures of the development of the arc in the argon as the distance between the electrodes is changed. Light is emitted from atom and ion lines, as well as from C_2 and, possibly, CN molecules. The first ionisation potential of some elements present in the plasma are summarized in

Table §.14. For a helium/carbon discharge without catalysts used for MWCNT synthesis, Gamaly and Ebbesen [114] *estimated that the carbon ion* C^+ *is the major ion, with the* density in the plasma of $n_{C+} = 5\times10^{15}$ cm^{-3} and near the cathode of $n_{C+} = 6.9\times10^{13}$ cm^{-3}. The ion velocity was estimated at $v_{ion} = 1.8\times10^5$ cm/s. At these conditions, the flux of carbon to the cathode is 6.25×10^{19} carbon/s and the number density of the plasma is dominated by helium with $n_{He} = 6.4\times10^{18}$ cm^{-3}. Nevertheless, Scott et al. found that yttrium and nickel ions are the major ions in the discharge when catalyst is added to the anode for SWNT optimal conditions. **Figs. §.13 and §.14** show measured optical emission spectra and that calculated with the atomic emission spectroscopy Fortran program named AES and developed by J. Hornkohl of the Tennessee Space Institute.

§.3.4 Modeling Arc Process

After presenting the main results obtained by the analysis of the experimental arc process, we need to develop a systemic approach in order to establish a relation between nanotubes or fullerene yield and arc parameters. Before establishing such relations, it is legitimate to ask some questions.

- Where and how nanotubes are formed in the reactor and how can this perfect linear and symmetric structure be formed in such an anisotropic plasma?
- Why in the same reactor, but with different conditions we obtain fullerenes C_{60} and C_{70}, MWCNT or SWNT?
- What are the growth precursors, and by which kinetic mechanisms are they formed and transported in the plasma? What is the role of the ions in the growth of nanotubes?
- What process parameters control this growth and how do they influence nanotube diameter and chirality?

Due to the complexity of time and space phenomena in the arc, and the interconnection of several individual processes such as electric, mass, and energy transfer, answering all these questions is a difficult task without the help of modeling. Very few works are reported in the literature to determine arc characteristics in the specific conditions of fullerene or nanotube growth. We selected some approaches, developed mainly by Gamaly and Ebbesen [114[77]] for multi-walled carbon nanotubes, Bilodeau et al. [[115]] and Kristinin and Moravskii [7,108] for fullerenes, Hinkov, [[116]] Scott, [[117]] and Farhat et al. [110] for single wall carbon nanotubes.

§.3.4.1 Phenomenological growth models

A quantitative description of nanotubes was first described by Gamaly and Ebbesen [114] based on the approximation of the distribution of density, velocity and temperature of carbon vapors, electric charge, potential, and electric field in the arc. On this basis, the authors presented a scenario for the nanotube formation, growth, and termination in time and space scales. It is doubtful that some of the details of this model are correct. However, it points out some useful facts. Typical multi-walled nanotubes conditions reported are obtained with the vaporization of pure graphite anode in a helium discharge chamber with P=500 Torr, anode to cathode distance $d_{AC}\leq1$mm, a potential drop of V=20 V and a current density of $j=150$ A/cm^2. At these conditions, average plasma temperature was assumed to be constant and ~ 4000 K. The deposit of area 0.5 cm^2 containing MWCNT grow at the cathode with a measured rate of 1 mm/min =16 μm/s. Assuming the average material density of 1.5 g/cm^3, this corresponds to a flux of carbon of 1.3×10^{20} $atoms/cm^2/s$ or a flow rate of 6.25×10^{19} atoms/s. At plasma temperature of 4000 K, calculated C^+ density in the plasma is $n_{C+} = 5\times10^{15}$ cm^{-3} and near the cathode $n_{C+} = 6.9\times10^{13}$ cm^{-3}. The ion velocity was estimated at $v_{ion} = 1.8\times10^5$ cm/s and the plasma is dominated by helium with $n_{He} = 6.4\times10^{18}$ cm^{-3}. Since the temperature of the plasma is close to the melting (4100 K) and boiling (4470 K) temperatures of graphite, carbon begin to evaporate producing a thin layer of saturated carbon vapor near the cathode surface. By a kinetic theory calculation of the evaporation, the authors determine that the carbon vapor sheath density is $n_{vap} \sim 1.35\times10^{18}$ cm^{-3} which is very close to the density of surrounding gas. The carbon vapor initially expands from the gas and forms a thin shield over the cathode surface. There the gas is cooled in a region very close to the cathode of only 2 to 3 μm in thickness having a temperature gradient of 26 K/cm. The saturated carbon is in fact diluted with helium in such way that the density after mixing is $n_{vap} \sim 4.8\times10^{17}$ cm^{-3}. According to the authors, the growth is due to the competitive input of two groups of carbon having different velocity distributions. The first group comes from the anode and has a Maxwellian velocity distribution. The second group is composed of ions accelerated in the gap between the positive space charge and the cathode. Due to the large difference in the first ionization potential between carbon (11.26 eV) and helium (24.87 eV), the major ion in the plasma is C^+. At a potential drop of V=20V, the ion velocity, calculated from the kinetic energy, equals 2×10^6 cm/s, which is ten times higher than thermal velocity. The presented scenario of deposit growth consists of cycles of four events.

1) Seed structure formation during the establishment of a steady ion current by collisions between C* + C* leading to C_2 which is the feedstock for the seed structure growth. The small characteristic time of C_2 formation ($10^{-7} - 10^{-8}$ s) permits forming about 10^7 seeds in a micrometer-thick layer.

2) Vertical tube growth during the stable stage of the discharge. Since the mean free path of carbon-carbon collisions (15 μm) is larger than the sheath thickness (2-3 μm), ions maintain perpendicular direction when moving to the cathode.

3) Termination of tube growth [illegible] instability [illegible] interruption [illegible] external voltage or current. Another cause of the instability reported by the authors is due to the splitting of the current into thinner filaments threads that moves randomly to the cathode.

4) The tube ends are capped by a process involving the rearrangement of carbon having Maxwellian distribution in the absence of current.

Based on this model, and the assumption that the characteristic reaction time for carbon-carbon attachment is proportional to the carbon-carbon collision time, the authors estimated the time of creating a 1 μm length tube with a diameter of 5 nm at ~0.02 s. Their conclusion is based on the qualitative agreement between the predicted time of these two groups with the experimental time ~0.07 s. Gamaly and Ebbesen pointed out the importance of cooling the cathode in reducing the velocity of carbons with Maxwellian distribution, thus reducing the perturbation amplitude and improving yield and quality of nanotubes. They finally concluded that the extremely high local field of ~10^8 V/cm as suggested by Smalley [118] to explain open end nanotube growth is four orders of magnitude higher than their calculated average electric field of 20 V / 10 mm ~2×10^4 V/cm.

§.3.4.2 Plasma models

The majority of the work of modeling electric arc discharge in presence of carbon and inert gas assumed local thermodynamic equilibrium (LTE). [110,7,111,114,115,119] This assumption consists of considering a unique temperature to represent the plasma. Thus the temperature of electrons T_e, ions T_i and atoms and neutral molecules of the gas T_g are equal. This assumption has been justified by the work of Bilodeau et al. [115] concerning fullerene modeling in the arc. According to them, pure helium plasmas show departures from LTE at pressures of 10^4 Pa. However, their calculations demonstrate that carbon species dominate in the arc region, resulting in an increase of the electric conductivity in comparison to pure helium. As a result, the electric field is limited to values of 10 V/cm, thus limiting deviations from LTE. In order to verify this assumption, Hinkov [116] calculated features of a plasma used at specific conditions of SWNT growth using the AURORA plasma software in the CHEMKIN collection [120]. This software predicts the steady state or time averaged properties of a well mixed or perfectly stirred plasma reactor. By modeling non-thermal plasmas, AURORA determines the ion, electron, and the neutral radical species concentrations, and the electron temperature. Well stirred reactors are characterized by a reactor volume, residence time or mass flow rate, heat loss or gas temperature, surface area, surface temperature, the incoming temperature and mixture composition, as well as the power deposited into the plasma for non-thermal systems. **Fig. §.15** Figure 9 is a schematic representation of the well-mixed plasma reactor [120] and its adaptation to predict plasma compositions [116]. The reactor of volume $V=0.6\ cm^3$ and containing a reactive cathode surface area of $A_m=2\ cm^2$ is continuously fed by a mass flow of 1800 sccm coming from the anode erosion. The composition of the inlet flow is calculated at 4000 K using Ivtanthermo [122] equilibrium computer code with the initial composition of the anode C:Ni:Y 94.8:4.2:1 at.%, diluted by a factor of 20 in the helium, as suggested by Krestinin and Moravskii [111]. The model takes into account 92 species including carbon radicals C, C_2, C_3, ... C_{79}, fullerenes C_{60F} and C_{70F}, inert gas He and ions Ni^+, Y^+, He^+, C^+, C_4^+, C_5^+ and C_{60}^+. All these species involves 562 electron and neutral reactions listed respectively in Tables §.15 and §.1. In addition to the homogeneous gas chemistry, the surface reactions listed in Table §.16 5, were added to account for the growth and etching of carbon nanotubes assumed to grow at the cathode surface from small carbon atoms. The sticking coefficient of unity for the deposition and 0.1 for etching was arbitrarily chosen. Finally, ions recombine in the sheath by the application of the Bohm condition for ion fluxes to surfaces. Indeed, as suggested by Meeks et al. [120], it is reasonable to constrain the ion flux to a surface according to the Bohm criterion. This condition results in the maximum net flux of a particular ion to a surface equal to the product of the ion density and the Bohm velocity. No data are available for recombination of nickel and yttrium ions in the sheath, hence an arbitrarily Bohm criterion of BOHM=0.4 was chosen by Hinkov [116]. The calculations were performed with the following conditions, inert gas=helium, measured erosion rate $G_{erosion} = 17{,}2$ mg/s at 100 A, assumed dilution factor $\tau_{dilution} = 20$ and a total pressure P= 660 mbar, with and without the LTE assumption. In the first calculation, the LTE assumption with $T_g=T_{ion}=T_e=6500$ K was assumed. The output results from AURORA are summarized in Table §.17 and reveal a residence time of about 28 μs and a weak electronic density of $6.4\times10^{14}\ cm^{-3}$. The predicted total ion current density of 10.4 A/cm^2 corresponds to a total current of the order of 20 A, based on a cathode surface area of 2.01 cm^2. This is much lower than 100 A, making the LTE assumption questionable. The second calculation was performed in the same conditions by maintaining gas temperature at T=6500 K and varying electron temperature from 0.56 eV (6500 K) to 5.17 eV (60000 K) corresponding to varying the current from 20 to 200 A. The estimated ion mass fractions, plotted in **Fig. §.16**, reveal that the major ion is Y^+ for the current intensity I <50 A and Ni^+ for the current intensity I >50. This result is explained by the low quantity of yttrium (1% at.) added to the anode material, and to the weak energy of ionization of the yttrium. Increasing the current intensity, one forms more and more Ni^+ ions from nickel atoms. **Fig. §.17** gives the evolution of calculated current density and electron temperature with electron density. In the optimal domain of current (80-120 A) for nanotube synthesis, the calculated electron density is between 1.25×10^{15} and 1.5×10^{15} cm^{-3}, and the electron temperature is 1.7 – 2.4 eV. Table §.18 summarizes the plasma composition calculated for I=100 A where the electron density of n_e = 1.4×10^{15} cm^{-3} is in good agreement with the measurements of Akita, et al. [51] in the interval $10^{15} – 10^{16}$ cm^{-3} for T= 6000 K as measured by optical emission spectroscopy in the following nanotube conditions: inert gas = helium, pressure P = 300 Torr, $G_{erosion}$ = 50 mg/s, and the flow rate of carbon without catalysts is 5500 sccm. The calculations indicate that when the catalyst is present the major ion is Ni^+ with a molar fraction of 1.3×10^{-3} followed by Y^+ with a molar fraction of 4.7×10^{-4} and C^+ with a molar fraction of 1.3×10^{-4}. From these results, even if the LTE condition is not satisfied, the weak rate of ionization of the carbon (<0.3%) indicate clearly that C^+ ions can not explain the fast nanotube growth rates, as was implied by the model of Gamaly and Ebbesen, described in Section §.3.4.1.

§.3.4.3 Zero-dimensional models

A zero-dimensional model for arc nanotubes synthesis was developed by Farhat et al. [110] and Hinkov [116] to calculate the equilibrium chemical composition in one point in the plasma, assuming LTE and given the gas temperature and pressure. The objective is to study the sensitivity of the kinetic model developed by Krestinin and Moravskii [119] in the specific conditions of nanotube growth.

§.3.4.3.a Model Equations

The multidimensional conservation model is reduced to zero spatial dimensions (0D) by assuming steady state, and a given temperature and zero velocity. The conservation equations can be written as a balance between an accumulation term on the left hand side equation (§.27) and chemical source term.

$$\frac{dY_i}{dt} = \omega_i \frac{M_i}{\rho} \quad (i=2,\dots,n_s) \qquad (§.27)$$

In this equation, n_s the number of gas species, Y_i is the mass fraction, ω_i is the chemical molar production of species i (mol. cm^{-3}. s^{-1}), M_i is the molecular weight (g. mol^{-1}), respectively of species I, ρ is the total mass density (g. cm^{-3}), and t is the time (s).
The source term ω_i is calculated by considering *R* elementary reversible or irreversible reactions involving n_s reacting chemical species A_i.

$$\sum_{i=1}^{ns} v'_{ir} A_i \overset{1}{\underset{2}{\leftrightarrow}} \sum_{i=1}^{ns} v''_{ir} A_i \qquad (r = 1, \dots, R) \qquad (§.28)$$

where ν'_{ir} and ν''_{ir} are the stoichiometric mole numbers of the reactants and products respectively and A_i the chemical symbol for the ith species. The chemical production rate ω_i of ith species can be written as a summation of the rate-of-progress variables for all the reactions involving the ith species :

$$\omega_i = \sum_{r=1}^{n_r} \Delta \nu_{ir} q_r \qquad (r = 1,\ldots,n_r) \qquad (§.29)$$

where $\Delta\nu_{ir} = \nu_{ir}'' - \nu_{ir}'$. The rate-of-progress variables q_r for the rth reaction is given by the difference of the forward rates 1 and the reverse rates 2 as:

$$q_r = k_{1r} \prod_{i=1}^{ns} C_i^{\nu'_{ir}} - k_{2r} \prod_{i=1}^{ns} C_i^{\nu''_{ir}} \qquad (r = 1, \ldots, R) \qquad (§.30)$$

Where k_{1r} and k_{2r} are the forward and reverse rate coefficients of the rth reactions and C_i is the molar concentration of ith species. Reverse reactions are written explicitly in the forward sense. The forward rate constants are calculated for each reaction r by assuming Arrhenius temperature dependence:

$$k_{1r} = A_r T^{\beta_r} \exp\left(\frac{-E_r}{RT}\right) \qquad (r = 1, \ldots, R) \qquad (§.31)$$

The rate-of-progress variables q_r are computed using CHEMKIN database and software package.

The condition of total mass fraction given by.

$$\sum_{i=1}^{ns} Y_i = 1 \qquad (§.32)$$

§.3.4.3.b Kinetic and thermodynamic data

The gas phase chemistry used in this approach involves neutral carbon species and includes small clusters ($C_1 - C_{10}$), cycles and polycycles ($C_{11} - C_{31}$), fullerene shells (C_{32}-C_{46}), fullerene clusters (C_{47}-C_{79}) and two fullerene molecules C_{60F} and C_{70F}. In addition, argon and/or helium, as well as nickel and yttrium, are considered as inert chemical species. There are at least 554 chemical reactions, listed in Table §.1 4, that describe the chemical kinetics of carbon vapor condensation and clusters of different sizes in the arc. The source of these data and the formation enthalpies are discussed by Krestinin and Moravsky [119]. The symbols ↔ and → in each reaction indicates that this reaction is reversible or irreversible respectively. Finally, this model includes 81 carbon species (C_1, C_2 ..., C_{79}, C_{60F}, C_{70F}) involving all the reactions of Table §.1. The thermodynamic properties of species are fitted in the temperature range of 300 to 20 000 K from Ivtanthermo, [122] JANAV [123], NASA [124], and CHEMKIN [40] databases and given in CHEMKIN (old NASA) format. This format presumes that the standard-state thermodynamic properties as Standard state molar heat capacity at constant pressure of the *i*th species c^0_{pi}, standard molar enthalpy H^0, and standard molar enthalpy S^0 are thermally "perfect", in that they are only functions of temperature and are given in terms of polynomial fits **(§.2)-(§.4).** For small carbon species, argon, helium, nickel and yttrium the polynomial coefficients are listed in Table §.4.

§.3.4.3.c Solution procedure

The solution of differential-algebraic-equations (DAE) representing mass conservation equations (§.27) and (§.32) employs a backward differential formula method implemented in LSODI package [125] . This software was designed to solve stiff, DAE and the solution procedure attempts time-integration from an initial guess of the variables. The initial composition of the gas was estimated at a given temperature and pressure using IVTANTHERMO [121] equilibrium computer code, with the initial composition of the anode C:Ni:Y 94.8:4.2:1 atom. %, diluted by a factor of 20 in helium. Time-stepping improves the starting point by relaxing it closer to the steady state solution. This solution method is much faster and much more stable in reaching steady-state convergence than the classical Newton iteration method. The model takes into account 84 equations corresponding to all the species including: radicals C, C_2, C_3, ..., C_{79}, fullerenes C_{60F} and $C_{70F,}$ nickel Ni, yttrium Y and inert gas He. These species involve the 554 reactions of Table §.1. The typical time evolution of the solution for carbon atom mole fractions calculated at T=4000 K and P=660 mbar, is given in **Fig. §.18**. The characteristic reaction time to obtain steady-state C mole fraction is about 1μs. At a cooler temperature, T=2000K, we start to form fullerenes from carbon clusters. **Figs. §.19 and §.20** *show the time evolution of carbon clusters* C_{58},C_{59}, C_{60} *and the fullerenes* C_{60F} and $C_{70F,}$ respectively. Fullerenes have a characteristic reaction time of about 10 μs. Finally, in **Figs. §.21**a and b are plotted mole fractions of small carbon species and total fullerene yield versus temperature calculated in helium at 660 mbar. We can see from these figures that fullerenes start to be formed at 3000 K.

§.3.4.4 Turbulent Fan Jet Model

When the electrode spacing is very small, carbon is ejected from between the electrodes as a radially expanding jet. Krestinin and Moravsky [7,111,119] developed a model to describe the chemical processes taking place in a turbulent fan jet leaving the interelectrode space.

§.3.4.4.a Model formulation

The turbulent jet model accounts for the main processes controlling fullerene formation in electric arc, namely, 1) cooling and mixing of carbon vapor in a buffer gas, 2) reactions of cluster growth and decomposition under non-isothermal conditions, 3) formation of soot particles and heterogeneous reactions on their surface. In this model, the flow from the arc zone is idealized as an axially symmetric fan jet represented in **Fig. §.22**. The pressure gradient in the reactor, the temperature gradient in the gap, as well as the rate of inert gas diffusion inward the inter-electrode zone were neglected. The model solves the gas dynamic equations governing the expansion of an initial volume ΔV_0 at the temperature T_0 with an initial high velocity U_0 of a jet surrounded by a pure and cold inert gas at T_{at}. The velocity profile U in the plane (z,r) representing a jet section is shown schematically in **Fig. §.22**.

§.3.4.4.b Model equations

The conservation equations are written within a boundary layer with turbulent mass and heat transfer across the jet in the following form:

$$\rho U \frac{\partial Y_i}{\partial r} = \frac{\partial}{\partial z} k_c \varepsilon_\tau \rho \frac{\partial Y_i}{\partial z} + M_i f_i \quad (i = 1,\ldots,n_g) \qquad (§.33)$$

$$\rho C_p U \frac{\partial T}{\partial r} = \frac{\partial}{\partial z} k_T \varepsilon_\tau \rho C_p \frac{\partial T}{\partial z} + f_T \qquad (§.34)$$

where ε_τ is the coefficient of turbulent momentum transfer, k_c and k_T are empirical coefficients relating momentum transfer to mass and heat transfer, Y_i and T respectively the mass fractions of the species i and the temperature at the position longitudinal, r, and transverse, z, coordinates of the jet. The terms, f_i and f_T are the rates of mixture component formation and the rate of heat release due to chemical reactions, M_i are the molecular weights of the mixture components, ρ is the gas density, C_p is the mixture specific heat, and U is the mass-mean gas velocity. To solve these partial differential equations, the semi empirical theory of free turbulent jet developed by Abramovich [126^{125}] is applied. In this theory, the ratio between the half-width of a free turbulent jet b and the mixing length L is assumed constant at each longitudinal position r of the jet. L/b = const ~ 0.2. In addition, due to the jet symmetry, derivatives of all the variables with respect to z are equal zero at the jet center plane. Hence temperature and concentration vary little within the turbulent mixing length L (r) and can be assumed constant and equal to their values at z=0. Thus, integrating the equations (§.33) and (§.34) with respect to z over interval [-L,L] yields to an approximate description of evolution of an elementary gas volume moving near the symmetry plane of a fan jet. By replacing the derivatives with respect to z by finite differences:

$$\frac{\partial T}{\partial z} = \frac{T_{at} - T}{b}; \frac{\partial Y_i}{\partial z} = \frac{Y_{0,i} - Y_i}{b} \qquad (§.35)$$

partial differential equations (§.33) and (§.34) are transformed via a procedure described in detail in [7] to a set of ordinary differential equations. These equations are written in CHEMKIN notation as following,

$$\frac{dY_i}{dt} = k_c\left(Y_{0,i} - Y_i\right) + \omega_i \frac{M_i}{\rho} \qquad (i=1,\ldots,n_g) \qquad (§.36\ 13)$$

$$\sum_{i=1}^{n_g} Y_i C_{p,i} \frac{dT}{dt} = \sum_{i=1}^{n_g} Y_i C_{p,i} k_T \left(T_{at} - T\right) + \omega_i h_i \frac{M_i}{\rho} \qquad (§.37\ 14)$$

where Y_i and $Y_{0,i}$ are the mass fractions of mixture components including carbon black particles in the reaction volume and buffer gas respectively, T is the temperature, ω_i is the chemical molar production of species i (mol. cm^{-3}. s^{-1}), M_i is the molecular weight (g. mol^{-1}), ρ is the total mass density (g. cm^{-3}), h_i is the specific enthalpy of the i^{th} species (erg/g), $C_{p,i}$ is the specific heat at constant pressure of the i^{th} species (ergs/g/K)) and t is the time (s). The mass and heat transfer coefficients k_c and k_T are calculated by the empirical formulas:

$$k_c = \frac{0{,}32}{\tau_{mix} + 2t} \qquad (§.38)$$

$$k_T = \frac{0{,}64}{\tau_{mix} + 2t} \qquad (§.39)$$

were τ_{mix} is the time of turbulent mixing calculated from the flow velocity in the jet within the arc zone U_0 using equation (§.40).

$$\tau_{mix} = \frac{r_A}{U_0}\left(\frac{r_A}{d_{AC}}\right)^{0{,}5} \qquad (§.40)$$

The flow velocity U_0 is calculated by equation (§.41) assuming that the carbon vapor in the arc zone is equilibrated with electrode graphite and taking the experimental value of the formation rate of fullerene carbon black, V_{soot}

$$U_0 = \frac{V_{soot} R T_0}{2\pi r_A d_{AC} P} \qquad (§.41)$$

where d_{AC} is the anode to cathode distance, r_A is the anode radius, R is the universal gas constant, P is the helium pressure in the reactor, and T_0 the arc temperature calculated from the equilibrium pressure of the carbon cluster vapor over graphite. V_{soot} is determined from the measured rate of ablation of the anode

§.3.4.4.c Numerical results

The representative experimental conditions of Krestinin and Moravskii are P=100-760 Torr, T_0=3600-3900 K and U_0=2-80 m/s. Under these experimental conditions, the model equations (§.36) and (§.37) were solved using the chemical gas model in Table §.1 and Table §.19. **Fig. §.23** compare calculated and experimental fullerene yields as obtained by Krestinin and Moravsky [8] at different pressures.

§.3.4.5 One-dimensional models

In order to analyze the effect of arc process parameters on temperature and species profiles in (1D), Farhat et al. [111] used the highly structured computer packages SPIN and SURFACE CHEMKIN developed by Kee et al. [40] at SANDIA for rotating disc CVD processes. The complex gas-phase chemical reaction mechanism representing carbon condensation from the arc was added into numerical simulations in a one-dimensional (1D) model. This model was formulated under specific conditions of nanotube growth in the inter-electrode region. It solves for species, temperature, and velocity profiles in a steady-state, one dimensional stagnation-point flow, with temperature dependant fluid properties.

§.3.4.5.a Model formulation

This model is a boundary value problem consisting of a set of ordinary differential equations, solved by a finite difference procedure. It assumes local thermal equilibrium (LTE) and solves the steady-state axial and radial momentum, species, and energy equations in one spatial dimension between the anode and the cathode. The model accounts for carbon deposition at the cathode by a set of surface reactions that simulates nanotube growth. The steady state assumption is justified by the continuous adjustment of the inter-electrode gap leading to a constant erosion rate of the anode, hence a constant condensation of carbon vapor close to the cathode. Local thermodynamic equilibrium was assumed based on the Bilodeau et al. [115] model for fullerene synthesis by arc discharge in the same range of pressure as nanotube synthesis.

§.3.4.5.b Model equations

The governing equations that are solved in the SPIN code include continuity, radial momentum, species conservation, and thermal energy, and are given below.

Continuity

$$\frac{1}{\rho}\frac{\partial \rho}{\partial t}=-\frac{\partial u}{\partial x}-2V-\frac{u}{\rho}\frac{\partial \rho}{\partial x}=0 \qquad (\S.42)$$

Radial momentum

$$\rho\frac{\partial V}{\partial t}=-\frac{\partial}{\partial x}(\mu\frac{\partial V}{\partial x})-\rho u\frac{\partial V}{\partial x}-\rho V^2-\frac{1}{r}\frac{\partial p}{\partial r}=0 \qquad (\S.43)$$

Species continuity

$$\rho\frac{\partial Y_i}{\partial t}+\frac{\partial(\rho Y_i V_i)}{\partial x}+\rho u\frac{\partial Y_i}{\partial x}=M_i\,\omega_i \quad (i=1,\ldots,n_g) \qquad (\S.44)$$

Thermal energy

$$\rho c_p\frac{\partial T}{\partial t}=\frac{\partial}{\partial x}\left(\lambda\frac{\partial T}{\partial x}\right)-\rho c_p u\frac{\partial T}{\partial x}-\sum_{i=1}^{n_g}(c_{pi}\rho Y_i V_i\frac{\partial T}{\partial x}+\dot{\omega}_i h_i)+S_q(x)-Q_{rad}=0 \qquad (\S.45)$$

Although these equations are stated in their transient form, the solution is obtained when all time derivatives are zero. In the governing equations, the independent variables are the distance normal to the cathode x (**Fig. §.24**), and the time t. The dependent variables are axial u and radial V velocities, gas temperature T, gas-phase species mass fractions Y_i. The mass density is given by ρ and the specific heats at constant pressure by c_p. In the radial momentum equation, p is the spatially varying component of the pressure [40]. The molecular weight and specific enthalpy of species i are given by M_i and h_i respectively. The viscosity and thermal conductivity are μ and λ. The net chemical production rate of species i by gas-phase reaction is ω_i. The species diffusion velocity V_i is calculated from mixture diffusion coefficient and species gradient [40]. The source term $S_q(x)$ *in* the energy equation accounts for the electrical energy dissipated in the arc. It was assumed that it is distributed in the form of Gaussian centered at x_s with a (half) half-width of w_s by the equation:

$$S_q(x)=q\frac{1}{w_s}\sqrt{\frac{3}{\pi}}e^{\left[\frac{-3(x-xs)^2}{w_s^2}\right]} \qquad (\S.46)$$

Here, q accounts for the total power integrated over its full spatial extent $q=\int_{-w_s}^{+w_s}S_q(x)\,dx$ and includes 100% of the net power added to the arc. The center of the interelectrode gap was chosen as the peak in the distribution x_s, and w_s chosen to adjust the flatness of the distribution. In the present calculations w_s was 0.15 cm, resulting in a very uniform distribution. The total energy q was calculated from measured electric power dissipated in the arc. It was corrected by the loss from arc plasma due to the gas convection. The radiative term Q_{rad} in the energy equation accounts for the net loss of energy by gas radiation. It was estimated from a curve fit of Owano [127]^{95} in atmospheric argon plasma by:

$$Q_{rad}=1.065\times10^{14}\,\alpha\exp(\frac{-141170}{T})\ (\frac{W}{m^3}) \qquad (\S.47)$$

with T the gas temperature in K and α a non-equilibrium factor accounting for the deviation from the equilibrium; $\alpha=1$ for local thermal equilibrium (LTE). Gas radiation is negligible when helium is used. Gas kinetics, thermodynamic and transport properties of species are estimated in the same way as in section §.3.4.3

§.3.4.5.c Surface chemistry

Carbon nanotube growth is considered as a boundary condition at the cathode by a set of surface reactions simulating nanotube growth. As a first approach, the open-end tube growth (scooter) mechanism developed by Smalley [118] and illustrated in **Fig. §.25** by an African calabash structure decorated by hexagons and open on the top, was implemented as a boundary condition. Open-ended nanotubes were first explained by the high local electric field in the region of nanotubes growth preventing their closure ends. More recently, catalysts such as Ni were thought to be attached to hold open the ends of nanotubes and promoted growth. It was assumed that nanotube growth occurs at the cathode surface (**Fig. §.26**) and that surface chemistry is controlled by the local terminated bond and not by the bulk nanotube bonds. Nanotube growth is based on the adsorption and desorption of three small carbon clusters (C_1 to C_3) to simulate nanotube growth. The surface reactions considered here are listed in Table §.20, where CR represents the nanotube radical site at the open edge of the tube and CNT is assumed to be the unique "bulk" species. In the reaction (S1) for example, carbon atoms C react with a radical site CR to generate a new radical site CR and one incorporated carbon into the bulk nanotube CNT. The pre-exponential factor of these reactions was fixed arbitrarily at 2.50×10^{11} and was varied as a parameter from 3.0×10^{4} for carbon addition of C, C_2 and C_3 on soot [119] to 1.0×10^{13} for carbon addition on diamond [128, 129]. Since no other carbon phases are incorporated in this model, the total number of sites Γ is calculated by geometrical considerations from Hamada's indices n and m. We consider a triangular arrangement of carbon nanotubes within a bundle [130] (**Fig. §.25**) and divide the number of atoms per hexagon by the area of the hexagon using the equation $\Gamma=\dfrac{3N_{at}}{3\sqrt{3}\,(d_{CNT}+d_{NT-NT})^2}\times\dfrac{1}{N_{Av}}$ with N_{at} the number of atoms per unit cell (nanotube), d_{CNT} the nanotube diameter, $d_{NT\text{-}NT}=0.340$ nm the distance between two adjacent nanotubes [129] and N_{Av} the Avogadro's number. For example for a (10,10) nanotube, $d_{CNT}=1.357$ nm and $N_{at}=20$, hence the site density is $\Gamma = 6.66\times10^{-10}$ moles/cm^2. For comparison, this is lower than the diamond site density [128] of 2.61×10^{-9} moles/cm^2. The surface site density is often assumed to be conserved; and the surface-species conservation equation is given by $\dfrac{dZ_{CR}}{dt}=\dfrac{s_{CR}}{\Gamma}=0$ where Z_{CR} is surface species site fraction and Γ is the surface site density [40]. The chemical production s_{CR} of surface species by surface reactions is given by the sum over the rate-of-progress variables for all surface reactions. The rate of production s_{CR} expressed in moles/cm^2/s is converted to linear nanotube growth rate G in µm/s by using nanotube bulk mass density $\rho_{CNT} = 2.20$ g/cm^3 and molecular weight $M_{CNT} = 12.01$ g/mol using the equation

$$G = \frac{s_{CR} M_{CNT}}{\rho_{CNT}} \qquad (§.48)$$

§.3.4.5.d Boundary conditions

The axial gas velocity at the anode was estimated from the measured erosion rate Φ and the total gas density ρ by $u_{anode} = \frac{\Phi}{\rho A}$ where A is the anode surface area. For a stagnation-point flow problem, axial velocity at the cathode is zero. The anode temperature was always fixed at the average vaporisation temperature of graphite, T_{ANODE}=4000 K. The temperature of the cathode T_C is predicted as a part of the solution by adding a radiative energy balance as a boundary condition. Close to cathode surface, the diffusive heat flux in the gas-phase is balanced by the thermal radiative heat loss to the anode given by: $\lambda \left.\frac{\partial T}{\partial x}\right|_{CATHODE} = \sigma \varepsilon (T_C^{\,4} - T_{ANODE}^{4}) F_{CA}$ where σ is the Stefan-Boltzmann constant, ε is the surface emissivity and T_{ANODE} is the anode temperature to which the cathode radiates. The radiative exchange form factor is F_{CA}. At the anode, mass fractions are calculated at the equilibrium temperature of 4000 K, given a dilution factor τ. This factor accounts for the mixing of anode material with inert atmosphere and is defined by the ratio $\tau = \frac{moles(C+Ni+Y)}{moles(C+Ni+Y+He)} \times 100$. In the case of evaporation of the mixture of 94at.%C/5at.%Ni/1at.%Y, Krestinin and Moravsky [7,111] reported that carbon vapor is diluted as much as τ=20-30 times by mixing with inert atmosphere. For the reduced model considered here, mass fractions at the anode were calculated using IVTANTHERMO [121] computer code. For the full model, mass fractions Y_i were calculated from a zero dimension (0D) model involving the following set of ordinary differential equations: $\rho \frac{\partial Y_i}{\partial t} = M_i\, \omega_i = 0 \quad (i = 1,\ldots,n_g)$ where the net chemical production rate ω_i is calculated, as discussed above, from all the reactions listed in Table §.1.

§.3.4.5.e Numerical results

Numerical simulation of nanotube growth in the arc reactor has been carried out by solving the set of model equations and the boundary conditions using the SPIN computer code for the full chemical model. The chemical model of Krestinin and Moravsky, developed originally for fullerene synthesis, was tested in typical single walled nanotube growth conditions in the interelectrode region. For these calculations, helium used was as buffer gas, with a total pressure of P=660 mbar and interelectrode gap of 3 mm. The measured electric power dissipated in the arc for 100 A electric current was $q=1.24\times10^{07}$ Watt/m^2; and the dilution factor at the anode was fixed at τ=20. In these conditions, the measured erosion rate was $\Phi=20.4\times10^{-03}$ g/s and the calculated mass density of the gas at the equilibrium temperature of 4000 K is $\rho=9.24\times10^{-06}$ g/cm^3. For a surface anode area of A=0.29 cm^2, the axial velocity u_{Anode}=7818 cm/s was estimated at the anode from mass conservation. When small gaps are considered, the form factor F_{CA}

should be accounted for. However, in these calculations it was set to unity. Calculated temperature profiles in the 3 mm interelectrode gap for pure helium are shown in **Fig. §.27**. A maximum temperature of ~ 6500 K is obtained at ~ 1 mm from the cathode and is in fairly good agreement with measured rotational temperature from optical emission spectroscopy performed by the Huczko group [49] (5300 K ± 500 K) in the center of the plasma with I=54 A and P=880 mbar). Nanotubes are created between 1200 K and 1800 K. [131,132] Such temperatures are reached very close to the cathode, justifying the assumption of nanotube growth at the cathode surface. The calculated mole fractions of major carbon species are shown in **Fig. §.28**. Due to the high temperature that exists throughout most of the gap, the discharge is dominated by atomic carbon. The regions close to the cathode and anode are cooler than the center of the plasma. This enhances carbon atom recombination and explains the two peaks of C_2 mole fraction shown in **Fig. §.28**. The first peak is due to the recombination of C atoms close to the anode and the second peak occurs at 0.3 mm from the cathode, and is due to the competition between gas and surface chemistry. This second peak constitutes a feedstock for nanotube growth. Radiation intensity contours measured at 515 nm by the Huczko group [49] indicate qualitatively the presence of two zones rich in C_2, in agreement with our calculations. It can be noted from **Fig. §.16** that decreases of C, C_2 and C_3 carbon species close to the cathode are due to the surface chemistry, and that fullerenes start to be formed at 0.3 mm close to the cathode. However, the (1D) model as developed here, is not able to calculate the distribution of fullerenes in all of the reactor. The region where fullerenes start to be formed is important from growth mechanism point of view and could be investigated by optical spectroscopy measurements. The calculated normalized species abundance at the cathode is plotted versus cluster size in **Fig. §.29**. It shows a roughly Gaussian distribution of even-numbered clusters with 28-58 carbon atoms and two peaks for C_{60} and C_{70}. Inserted in **Fig. §.29** are the distributions of carbon clusters as measured under various experimental conditions for laser ablation of a graphite target by Kroto *et al.* [1] that show a similar behavior. The calculated number densities of major carbon species are listed in Table §.21. Number densities of the buffer gas and the catalysts calculated from equation of state are fairly constant $n_{He}=1.4\times10^{18}$ cm^{-3}, $n_{Ni}=2.0\times10^{14}$ cm^{-3} and $n_Y=3.2\times10^{14}$ cm^{-3}.

Finally, the calculated nanotube growth rate using (10,10) is plotted in **Fig. §.30** for dilution factors 5, 10 and 20, as the pre-exponential factor of surface reactions varied from 3.0×10^4 carbon addition of C, C_2 and C_3 on soot [116^{88}] to 1.0×10^{13} corresponding to carbon addition on diamond [127,128]. The results show that the predicted growth rate ranges from a few μm/min to 1000 μm/min.

§.3.4.6 Two-dimensional models

A two dimensional (2D) approach was developed by Bilodeau, et al. [115] for simulating carbon arc reactor for fullerene synthesis in helium or argon. The model solves velocities, temperature, and total concentration of carbon species in the two-dimensional axisymmetric space between the electrodes. The model accounts for carbon evaporation from the anode, deposition on the cathode, and condensation in the regions surrounding the arc.

§.3.4.6.a Model formulation

Bilodeau, et al. [115] assumed an axisymmetric laminar flow, steady state and local thermodynamic equilibrium (LTE). The anode erosion rate was assumed uniform and was obtained experimentally. The deposition on the surface of the cathode is governed by diffusion, with velocities of the order of 400 m/s. The drift of ionic species having a velocity 10 m/s due to the electric field was neglected. The input of energy in the arc is due to ohmic heating and to the enthalpy flux of the electrons. Enthalpy diffusion due to species transport is considered and radiation losses are considered using the net emission coefficient method with a plasma thickness of 0.5 mm. As shown in **Fig. §.31**, two calculation domains were chosen to predict temperature and velocities distribution. The first domain, noted (1) in **Fig. §.31** represents the interelectrode gap of a thickness chosen equal to 1 or 4 mm. The second domain noted (2) in **Fig. §.31** represents the entire reactor.

§.3.4.6.b Model equations

Continuity

$$\vec{\nabla}.(\rho\vec{v})=S_m \qquad (§.49)$$

Axial and radial momentum conservation

$$\vec{\nabla}.(\rho\vec{v}\vec{v})=-\vec{\nabla}P+\vec{\nabla}.(\mu\vec{\nabla}\vec{v})+\rho\vec{g}+\vec{j}\times\vec{B} \qquad (§.50)$$

Energy conservation:

$$\vec{\nabla}.(\rho\vec{v}h)=\vec{\nabla}.(\frac{\kappa}{c_p}\vec{\nabla}h)+\frac{j_x^2}{\sigma}+\frac{5}{2}\frac{k_B}{ec_p}\vec{j}.\vec{\nabla}h-\vec{\nabla}.(\frac{\kappa}{c_p}-\rho D_C)(h_C-h_g)\vec{\nabla}\omega_C-4\pi\varepsilon_n+S_h \qquad (§.51)$$

Carbon species conservation

$$\nabla.(\rho v\omega_C)=\nabla.(\rho D_C\nabla\omega_C)+S_m \qquad (§.52)$$

In these equations, $\vec{v}$ is the gas velocity, P is the local pressure, μ the viscosity, ρ the mass density, g the gravitational acceleration, h is the specific enthalpy, h_C and h_g the enthalpy of pure carbon and pure buffer gas, respectively, κ is the thermal conductivity, c_p the heat capacity at constant pressure, ε_n is the net emission coefficient, e the charge of the electron, k_B is the Boltzmann constant, σ the electrical conductivity, ω_C is the mass fraction of carbon species and D_C is the diffusion coefficient of the carbon species. The axial current intensity

$j_x = \sigma E$ is calculated from the linear electric field E, the conductance G, the total current intensity I, and the radius of the electrodes.

$$E=\frac{I}{G}=\frac{I}{2\pi\int_0^R \sigma r dr} \qquad (§.53)$$

B is the magnetic field intensity:

$$B=\frac{\mu_0}{R}\int_0^R J_r dr \qquad (§.54)$$

with μ_0 the magnetic permeability of vacuum. S_h and S_m are respectively heat and mass source terms. The mass source term S_m represents the carbon evaporation near the anode (positive term) or the condensation of the condensation of carbon species near the cathode (negative term).

§.3.4.6.c Numerical results

The model equations presented above were solved using the SIMPLE method described by Patankar [133]. Boundary conditions are the following:

- On the reactor wall, the temperature T=350 K, the axial and radial velocities $V_z=V_r=0$ and the carbon composition $X_C=0$.
- On the reactor axis, the radial velocity $v_r=o$ and radial gradients $\frac{\partial\phi}{\partial r}=0$; with $\phi=(T, X_C, V_z, J_z)$
- At the anode and cathode tip T=3300 K on the side and T=2800 K on the axis.

Typical temperature profile maps are shown on **Fig. §.32** for helium and argon in the two simulations domains (1) and (2) discussed above. For a 1-mm gap the maximum temperature is ~12,000 K. When the gap distance is increased to 4 mm, this maximum temperature increases to over 17,000 K near the cathode. Bilodeau, et al. attribute this difference to the lower carbon concentration and higher electrical resistivity. When argon is used instead of helium with a gap width of 4 mm, the temperature range (1500 K-5000 K) is wider in argon than in helium. In the temperature range 2000-3000 K assumed by the authors to be favorable for the formation of fullerene precursors, the carbon species concentration is higher in helium than in argon.

§.3.4.6.d Flow and heat transfer modeling

More recently, Hinkov [116] compared the temperature profiles obtained in nanotube conditions for helium at 660 mbar and argon at 100 mbar. The model consists of Navier Stokes equations implemented in FLUENT computer code. For these calculations, only two species, namely carbon atoms and helium or argon without any chemical reactions were considered. A constant heat flux of 6.5×10^9 ergs.cm^{-2}.s^{-1} for argon and 1.2×10^{10} for helium was considered from the measured power. The wall reactor temperature was 300 K. The anode and cathode temperatures are 4000 K and 2000 K, respectively. From Fig. §.33, the calculated maximum temperature is 14700 K for argon and 9080 K for helium. The lower thermal conductivity of argon leads to a much larger hot zone close to the cathode. This result could explain the higher observed nanotube yield when helium is used rather than argon.

§.3.5 Arc Modeling Concluding Remarks

Mathematical modeling of the carbon arc has been the subject of numerous studies where the objective was to better understand fullerene and nanotube growth, as well as to predict the chemical composition of species and the temperature distribution in the discharge. Several approaches were developed and permitted isolating the effects of thermal, kinetic, mixing and electric processes on vaporization and condensation of carbon and metallic clusters. Compared with other high temperature techniques, the uniqueness of the arc is the presence of ions. When a metallic catalyst is mixed to the graphite in the anode, the major ions as measured and calculated are found to be the catalyst ion Y^+ or Ni^+ and not C^+. Hence, in addition to its catalytic role, these metals play the role of current carriers in the discharge. In addition, the energy of ionization of the catalyst is weak; and the process of the anode vaporization is more efficient.

Otherwise, the experimental results indicate that the limiting process in nanotube growth is the rate of anode erosion. It will be interesting to explore the effect of other types of catalysts with lower energies of ionization. In addition, we can conclude that the low density of carbon ions in the discharge does not explain the fast growth of nanotubes. Hence, carbon nanotube growth occurs from neutral precursors and could be modeled by a set of surface reactions simulating open nanotube growth exposed to a mass flux from the anode. Since in this approach nanotube surface chemistry is controlled by the local terminated bond and not by the bulk nanotube bond, a mechanistic approach based on the formal resemblance between the bonding and the structure between open nanotube and other carbon surfaces was proposed to explain nanotube growth. Predicted growth rates are in the range of 100 to 1000 microns/min. Nevertheless, a debate still exists on the reason why the nanotube is maintained open during the growth. Some authors attributed this fact to the high local electric field in the growth region close to the cathode; but the predicted values of this local field varies within four orders of magnitude from 10^4 to10^8 V/cm. This suggest that further modeling efforts are needed to estimate with accuracy the electric field distribution in the connection with thermal, kinetic and turbulent mixing in multi-dimensional configuration. Further development of a modeling approach is in the direction of selecting more representative gas phase and surface reactions and using ab-initio calculations of mechanisms and kinetic data. There is a real need for accurate kinetic data for the adsorption of small carbon clusters on open nanotubes of different diameters and chiralities or on pentagon-heptagon defects of closed nanotubes. Since we have evidence that SWNTs may grow in the gas phase, further work in modeling the arc process will include gas phase production as proposed in Ref. [14]. There, gas phase reactions for the production of SWNTs are proposed to grow from carbon/nickel clusters using a formalism for the reactions like the one developed for the Boudouard reaction used in the high-pressure carbon monoxide process (HiPco) by Dateo et al. [28]. The calculations will be extended to two dimensions, and possibly 3D in order to take into account both collaret and core deposit growth in the cathode region. Even though, growth chemistry and surface site densities are very different for SWNT growth in the collaret as compared with MWNT formation in the hard deposit, the formalism discussed in this paper remains valid, and could take into account simultaneous growth of these species in 2D or 3D configuration.

§.4 Computational Fluid Dynamics Analysis of Transient Carbon Plumes in Laser-Ablation SWNT Production

The use of computational fluid dynamics (CFD) simulation methods for the analysis of the flowfields resulting from the laser ablation of carbon targets in the production of single-walled carbon nanotube production is a relatively new practice, with most studies having been conducted only since the turn of the century. CFD techniques for the solution of the governing equations of fluid motion have been present since the advent of high-speed computers in the 1960's. The National Aeronautics and Space Administration (NASA) and various aircraft corporations originally developed CFD methods primarily by for the solution of external flowfields surrounding aircraft and high-speed space vehicles leaving or returning to the Earth's atmosphere. Additionally, CFD methods for the solution of internal flows such as those occurring through gas turbine engines were developed at the same time as external solution techniques or "codes." Recently, CFD methods have gained popularity in other fields of endeavor that are less "aeronautical" in nature such as the analysis of various forms of materials processing, or when the fluid dynamics equations are merged with equations of electrodynamic forces such as the Maxwell equations (in a group of techniques referred to as "magnetohydrodynamics" or MHD), to such diverse fields of study as the flow of charged particles in the magnetosphere of the Earth. Two excellent references for general conventional internal and external CFD techniques are the works of Hirsch [134, 135] and Hoffman and Chiang [136]. The former publication is more theoretical in nature than the latter, however the latter provides a better introduction for the casual CFD code user.

Recent work in the application of CFD methods to laser ablation flowfield studies have been accomplished by both the solution of the Euler equations [134] which ignore viscous effects in the solution technique and by solution of the Navier-Stokes equations [134] which do incorporate viscous effects. Both methodologies will be examined as they have been applied to laser-ablation SWNT production in the following paragraphs. All numerical techniques are approximations of the full partial differential equations of fluid motion, be they Euler or Navier-Stokes equations, and the solution of the governing PDE's calculated by computer codes will be highly dependant upon the boundary conditions applied. All transient solution methods are highly dependant on two factors – boundary conditions and the time step size taken at each time step. Transient methods rely on having accurate assessment of the current flowfield and then extrapolate the current solution into the future by known mathematical methods. Therefore, no discussion of the CFD techniques as applied to laser ablation flowfields would be complete without a discussion of the boundary condition determination for the flowfields – such discussion will follow the examination of the basic numerical solution methodology for the Euler and Navier-Stokes equations.

§.4.1 Inviscid Solution of Carbon Plumes in Laser Ablation

Lobao and Povitsky [137] have successfully used a unique combined Eulerian and Lagrangian approach to the solution of the flowfields resulting from the rapid vaporization of carbon targets in the SWNT oven. Note should be made that the phrase "Eulerian" in this sense refers to analysis by a fixed control volume, not to the governing inviscid fluid dynamics conservation equations – although Lobao and Povitsky do indeed use the Euler equations in their methodology. Lagrangian methods differ from Eulerian in that individual particles are tracked as they flow through space; and overall thermophysical parameters are then calculated by statistical techniques applied to the many particles in the flowfield.

Lobao and Povitsky make the assumption that the inviscid Euler equations suffice for an analysis of the laser ablation of carbon due to the rapid time frames in which the ablation process occurs. The laser irradiation times for the laser ablation process as practiced at NASA JSC are approximately 10 ns in duration, although the material may continue to ablate for several nanoseconds after the irradiation terminates. It should be noted however that viscous shear stresses, τ, are a function of velocity gradients wherein:

$$\tau_{ij} = \mu \frac{\partial v_i}{\partial x_j} \tag{§.55}$$

for a Newtonian fluid, where v_i is the velocity component in the "i" direction, x_j represents the "j" spatial direction, and μ is the viscosity. A direct physical dependency upon time in the viscous components of the flow physics does not exist then. Given the extreme velocity gradients that occur in the laser ablation process, with inlet velocities of the ablative carbon being on the order of kilometers per second flowing into essentially quiescent argon gas It is possible that even given the short time duration of the flow viscous effects may be of significant enough magnitude that they cannot be ignored.

§.4.1.1 Solution Methodology

Lobao and Povitsky used the two-dimensional compressible Euler equations with a generalized curvilinear coordinate system in ξ, η coordinates. The equations can be represented in vector form by:

$$\frac{\partial Q}{\partial t}+\frac{\partial F}{\partial \xi}+\frac{\partial G}{\partial \eta}=S \qquad (\S.56)$$

where the vectors of conserved variables (Q, F, G, and S) are given by:

$$Q=\frac{\delta}{J}\begin{bmatrix}\rho\\ \rho u\\ \rho v\\ E\\ \rho C_1\\ \rho C_2\end{bmatrix} \qquad F=\frac{\delta}{J}\begin{bmatrix}\rho U\\ \rho uU+\xi_x P\\ \rho vU+\xi_y P\\ (E+P)U\\ \rho C_1 U\\ \rho C_2 U\end{bmatrix}$$

$$G=\frac{\delta}{J}\begin{bmatrix}\rho V\\ \rho uV+\eta_x P\\ \rho vV+\eta_y P\\ (E+P)V\\ \rho C_1 V\\ \rho C_2 V\end{bmatrix} \qquad S=\frac{1}{J}\begin{bmatrix}0\\ 0\\ P\\ 0\\ 0\\ 0\end{bmatrix} \qquad (\S.57)$$

In this formulation, ρ represents the local gas density, u and v are the local velocity components, U and V are the contravariant velocities, E is the total energy, and P the pressure. C_1 and C_2 are the mass fractions of the two species. ξ_x, ξ_y, η_x, and η_y are the metrics of the coordinate transformation. J represents the Jacobian of the coordinate transformation, and δ is the radial axisymmetric coordinate in the η direction. The first equation represents the conservation of mass while the second and third equations are the conservation of momentum in two dimensions. The fourth equation is the conservation of energy, while the final two equations are the "conservation of species" equations for the two chemical species, C_3 and Ar, used in the Lobao and Povitsky analysis. The gas is assumed to be a calorically perfect gas in their analysis. Excellent references for further elaboration on the Euler equations and their generalized coordinate versions can be found in [135,[138]]. Lobao and Povitsky use a second-order upwind scheme for the conservation equations called "MUSCL" [134] and they use a central relaxing Total Variation

Diminishing (TVD) scheme best described in their paper [136]. The Lagrangian scheme used by Lobao and Povitsky to solve for particle motion in the flowfield is not well described in their paper other than the fact that it is based upon a second-order Runge-Kutta scheme, and yields particle streak lines in the resulting carbon plume.

Lobao and Povitsky considered an axisymmetrical flow domain that was 25 cm in the longitudinal direction by 5 cm in the lateral dimension with a structured grid giving a grid size of 250 x 50 computational nodes. Initial conditions inside the flow chamber were a pressure of 1 atm and a temperature of 1500 K for the argon in simulation of a high-pressure ablation process and also for a pressure of 10^{-6} atm for a low-pressure ablation case in their paper. The boundary conditions at the site of the laser irradiation are given as 100 atm of pressure at a temperature of 5000 K. The irradiation boundary condition was allowed to propagate for 20 ns with an initial time step of 10^{-11} sec. The ablation boundary condition is then replaced by the flow chamber conditions and the entering plume of C_3 is allowed to propagate downstream. Time steps in the Lobao and Povitsky method were controlled by adjustment of the Courant-Friedricks-Lewy, or CFL, number given the fixed even grid spacing.

§.4.1.2 Results

Lobao and Povitsky simulated a number of variations upon the standard conditions used in the laser ablation at NASA JSC and qualitative comparisons were made between the parametric variations, although no comparisons were made to existing experimental data [139] for shock front expansion. As previously mentioned, two variations on the chamber pressure were simulated and showed consistent physical results in that the C_3 plume expanded more rapidly in the lower chamber pressure than in the 1 atm pressure case.

Other variations on the standard operating conditions that Lobao and Povitsky examined included the influence of carbon injection velocity on the flowfield dynamics. Initially, the entrance velocity of the carbon plume was set to zero and the plume allowed to propagate by virtue of the pressure differential. Additional injection velocities were simulated in their paper although few results were shown. A final variation examined by Lobao and Povitsky was the effect of the interaction of multiple laser irradiations upon overall plume dynamics. The standard processing of SWNT calls for irradiation of 10 ns duration for the first pulse followed 50 ns later by a second pulse of 10 ns duration. This process then repeats on a 60 Hz cycle. Lobao and Povitsky allow for a similar double-plume injection however using a gap of 16 μs between irradiation intervals. The main effect of the multiple plume interaction noted by Lobao and Povitsky was the increase in plume temperatures observed from the reflected shock waves re-compressing the plume from wall and plume interactions.

§.4.2 Navier-Stokes Solutions of Carbon Plumes in Laser Ablation

Greendyke et al [140, 141, 142, 143, 144, 145] have conducted a number of studies of the carbon plume resulting from laser ablation of a carbon surface in SWNT production using a full Navier-Stokes solution of the flow equations. In preliminary work [139], it was determined that the viscous stress terms could not be ignored given that the background flow was approximately 3 cm/s yet the carbon plume entrance velocity was on the order of 5 km/s. such large differences in velocity would necessarily lead to large viscous stress terms (as explained in the previous section) given the magnitude of the inevitable velocity gradients.

In his first study [139], Greendyke used the VULCAN code [146], which was originally designed for the study and analysis of internal supersonic combustion processes in hypersonic propulsion applications. The code was selected for its ability to handle mixed elliptical, parabolic, and hyperbolic flowfield equations. The code solves the generalized curvilinear Navier-Stokes equations described by:

$$Q_t + (E - E_v)_\xi + (F - F_v)_\eta + (G - G_v)_\zeta = S$$

where Q_t, E, F, G, and S are vectors describing the conserved variables included in the conservation of mass, momentum, energy, and species conservation equations as best described by White and Morrison [146]. E_v, F_v, and G_v represent the viscous flux vectors and are also described in [146]. In addition to the full Navier-Stokes equations, the VULCAN code also contains several turbulence model formulations, and Greendyke selected the k-ω model of Pope (described, along with other turbulence models in [147]) for his studies. The VULCAN code utilizes several solution methodologies for the Navier-Stokes equations, and Greendyke selected the time-accurate 4th order Runge-Kutta methodology option of the VULCAN code that is based upon a method first developed by Jameson et al [148] for the solution of the Euler equations. In general however, any CFD code capable of mixed flow regimes would work well in laser ablation plume development studies – a very good synopsis of modern CFD codes can be found in Laney [149] and at the accompanying web site [150].

§.4.2.1 Boundary Condition Determination at Ablative Surfaces

Before any CFD code can be accurately run for the solution of carbon plumes, it is necessary to correctly determine the boundary conditions at the ablative surface – without the boundary conditions correctly determined, no CFD code can predict reliable results. However, very little experimental information was available for the boundary conditions at the surface of the laser ablation carbon target. The only known thermophysical quantities had been the carbon mass ablation rate of 1.6×10^{-6} gm/laser pulse in argon, and the approximate energy of 300 mJ over the 5 mm laser spot size. Greendyke et al's original studies [140,141] assumed that the carbon mass was injected into the flowfield through the 10 ns duration of the laser pulse. A simultaneous solution of both the ideal gas equation

$$PV = NRT \tag{§.58}$$

and the Clausius-Claperon equation:

$$P = P_{ref} \cdot e^{\frac{-\Delta H_{vap}}{kT}} \tag{§.59}$$

resulted in a density of 10.59 kg/m^3, a gas temperature of 5211 K, a vapor pressure of 377 atm., and a carbon injection velocity of 1900 m/s at the target surface. In those studies however, the resulting propagating carbon plumes exceeded the shock front locations data gathered by Puretzky, et al. [139] past the 200 μs post-ablation time.

In later studies [142,143], the ablation time was assumed to be 15 ns – the additional 5 ns worth of ejected ablation material coming after the termination of the laser pulse. The resulting solution of ideal gas and Clausius-Claperon equations showed that while the temperature of the injected carbon was relatively insensitive to the additional ablation time (T=4950 K), the vapor pressure of the carbon plume dropped considerably to approximately 100 atm. The corresponding density was an order of magnitude less, 1.039 kg/m^3, and the plume injection velocity rose to 5228 m/s due to the lower molecular weight. Chemical equilibrium was assumed at the ablation surface and the CHEMKIN [40] code was used to determine inlet carbon species mass fractions for C through C_5 (no data being available in CHEMKIN for C_6). C_3 and C_5 were found to be the dominant species at the ablation surface inlet with the mass fraction of C_3 being 0.463 and C_5 being 0.426. The next contributors to the inlet flow were C_2 and C_4 with species mass fractions of 0.044 and 0.059 respectively. The atomic carbon mass fraction was nearly negligible at 0.008.

§.4.2.2 Flow Domain Gridding

After the correct determination of flowfield boundary conditions, the domain of interest needs to be resolved into a computational grid for the calculation of flowfield characteristics. Greendyke [140] originally used a 2D axisymmetric solution methodology for the flowfield volume with a 2D grid. At the time of his first investigation into laser ablation carbon flowfields, little was known of the resulting flowfield and the degree to which the carbon plume would propagate into the flowfield downstream of the carbon targets or the region in the outer quartz tube of the laser ablation oven. Fig. §.34 shows the original axisymmetric grid that was used by Greendyke in the original investigations. Fig. §.34 however displays a symmetrical grid about the y=0 axis. Only the portions for $y \geq 0$ are used in the actual axisymmetric flowfield calculations. One problem encountered was that the grid only extends to 10 cm in front of the carbon target and boundary conditions at the upstream portion of the background argon flow reflected the pressure wave resulting from ablation boundary conditions back into the propagating carbon flow. In later studies, Greendyke et al [142-145] used a "primary grid" (Fig. §.35) with 0.5 mm grid node locations for the first 10 cm in front of the ablation surface for the inner quartz tube alone as in the first work [140-141], with a "secondary grid" of 0.5 mm vertical spacing and 5 cm horizontal spacing out to a point 55 cm upstream of the carbon target. The elongated flowfield region under consideration alleviated the problem of reflecting pressure waves returning to influence the carbon plume's propagation into the argon background flow.

Multiple gridding software options are available to the researcher, with varying degrees of complexity to use. The most convenient of the available gridding software codes is the *Mesh Generator*^{TM} software [151] available as an "add-on" package to Amtec Engineering Inc.'s *Tecplot*$^{®}$ software [152]. The *Mesh Generator*^{TM} is capable of outputting grid information in both the ASCII format and the PLOT3D form (PLOT3D is a graphics package for CFD use that is available from the Open Channel Foundation – see their web site at [153]) used by many commercially available CFD codes such as the VULCAN code [146].

§.4.2.3 Flowfield Solution Procedures used by Greendyke et al

In all of the studies by Greendyke, et al. [140-145] the same procedure was used throughout. After determination of the boundary conditions, the first priority of the simulations was the solution of the "base" argon flow. The global elliptical viscous method of the VULCAN code was used with diagonal approximate-factorization in axisymmetric fashion for this part of the simulation. Full k-ω turbulence modeling and a mixture of thermally perfect gases options were chosen. The solution was allowed to converge until a sixth-order reduction in the L2 norm was observed.

Actual simulation of the carbon plume resulting from the laser-ablation of the target could proceed with the base flow established. To simulate the carbon plume a jet of carbon was allowed to enter at a density, with the boundary conditions described above, from the first five grid point locations in the grid block immediately in front of the carbon target corresponding to 2.5 mm in actual length. Flow enters axisymmetrically having a radius of the laser beam's spot size. The time-accurate Runge-Kutta solution procedure was applied to the restart files from the base flow simulation for 100 (or 150 in later studies) time steps of 0.1 ns each – corresponding to the actual duration of a laser pulse. The restart files from this "carbon-injection" simulation were themselves used in subsequent simulations with the carbon mass flow injection deleted in the input data file for VULCAN. An isothermal wall boundary condition was used in place of the carbon injection condition with a temperature set to slightly higher (1773 K) than the initial ambient conditions in the nanotube production chamber. This boundary condition was held constant until 60 ns of simulated time had passed and then the ablation boundary condition was re-initiated for another 15 ns of simulated time to correspond to the second laser ablation of the processing on a 60 Hz cycle as practiced at NASA Johnson Space Center. The flow with the developing carbon plume was simply allowed to develop naturally to whatever point in time required by manipulation of the time step size and maximum number of iterations allowed in the VULCAN input data file.

§.4.2.4 Results of Navier-Stokes Simulations

For the original work with full Navier-Stokes solution methods, Greendyke et al used only C_3 as the injected species at the carbon ablation boundary points to determine flowfield characteristics and plume propagation into the background argon gas. No chemical reactions were allowed in these studies. Fig. §.36 shows the result of the C_3 injection simulations at 200 μs post-injection time, and indicates the classic "smoke ring" profile of the carbon plume observed by multiple experimental investigations. Further confirmation of the accuracy of the Navier-Stokes modeling was presented by Greendyke, et al. [143] using only C_3 as the injected carbon species without chemical reactions.. Good comparisons were obtained with experimental observations of carbon plume propagation conducted by Puretzky, et al. [139] for the earlier post-injection times. As the flowfield solutions were allowed to progress however, computational results for the leading edge of the carbon plume began to overtake experimental results at the 1-millisecond point of post-injection time. Temperature contours compared favorably to experimental results as well in this study as can be seen in Fig. §.37.

In later studies [142-145], Greendyke et al added chemical reaction mechanisms to the flowfield solution methodologies. The first reaction model [141] was a twelve species, 14-reaction model for the formation of carbon molecules up to C_6 including the ion species of C^+, C_4^+, and C_5^+ as well as electron concentrations. The chemical reaction model was a reduced form of the reaction mechanism for the formation of C_{60} and C_{70}

fullerenes developed by Krestinin and Moravsky [8]. The primary purpose of the inclusion of higher species and chemical reactions was two-fold. The first purpose was to see what effect condensation of the carbon species would have on flowfield dynamics and temperature profiles. The second purpose was to determine if formation of the C_6 molecule, since it is not injected in the boundary conditions, would provide some indication to the thermophysical conditions for higher carbon molecule formation. The formation of C_6 would then serve as an "indicator species" for more complex carbon molecule formation. One discrepancy in this initial study with chemical reaction mechanisms was immediately observed – temperature profiles with chemical reaction mechanisms quickly exceeded the temperature profiles from earlier work – this result was first thought to be the result of energy being released into the flowfield from the condensation of lighter carbon species. However, in later work, Greendyke, et al. [144] discovered that the high temperatures were the result of excessive time steps being used in combination with chemical reactions. If the time steps for the initial laser ablation boundary conditions were decreased to 0.01 ns, temperature profiles in argon background gases returned to similar, although not identical, profiles for the original work with C_3. A curious result of this work was that even with the higher temperature profiles, leading edge propagation of the carbon plume was comparable to the earlier work [141], but deviated from Puretzky et al's experimental work [139] at post-ablation onset times at, or beyond, 1 millisecond. A possible cause for the higher plume propagation speed of the calculated results than experimental could be the curve-fit data incorporated into the input files used in the VULCAN code for diffusion of the higher species of carbon. No data was available for the higher carbon species and data for C and C_2 was simply extrapolated for higher species. As is generally known, lighter species will diffuse faster than heavier species.

It is impractical to use the full C_{60} and C_{70} model for fullerene formation of Krestinin and Moravsky. All flowfield solution methods such as the VULCAN code have to solve the species continuity equations at each grid point in the considered flowfield domain. Computational intensity therefore increases with the number of grid points and species by the relationship:

$$CPU \propto (N \bullet S)^2$$

where CPU indicates CPU processor time, N is the number of grid point locations in the domain, and S is the number of chemical species. As a result, for the flowfield grid described in [138], computational times of up to 30 minutes were required for a single iteration at a time step of 10^{-13} s thereby rendering such CFD studies impractical.

In the same studies [143-145], work began by Greendyke et al on duplicating a series of parametric experimental studies conducted at NASA Johnson Space Center [154]. The latest work [145], represented the culmination of the computational simulations to duplicate the set of experiments. For this study, the 12 species model originally used was replaced by an 11 species model with 14 reactions – which is given in Table §.22. The goals of this study were to gain insight into the thermophysical characteristics of the flows under differing pressures, background gas temperatures, different background gas chemical species, and differing diameters of the quartz inner tube of the laser ablation oven. A secondary goal was again to attempt to define "indicators" in the flowfield solutions of the carbon plume that would provide insight in the refinement of the laser ablation SWNT processing and allow improvement of the method for increased production. Unfortunately, in the set of experiments that this study was based upon it was not possible to determine the actual quantities of SWNT produced in the experiments. Only the total carbon ablated was available, thereby negating the ability to do a direct comparison between computational studies and SWNT production.

However, certain insights were still available from the computational study. One of the main results of Greendyke's study was a direct correlation between plume expansion into the background gas and the amount of recovered carbon from the experiments. A plume expansion factor, ϕ, was defined by Greendyke as:

$$\phi = \iiint \left[\frac{\rho_{carbon}}{\rho} \bullet \sqrt{x^2 + y^2} \right] dV \qquad (\S.60)$$

where,

$$\frac{\rho_{carbon}}{\rho} = \sum_{\substack{carbon \\ species}} \frac{\rho_i}{\rho} \qquad (\S.61)$$

or, the local summation of the individual carbon species' mass fractions. The plume expansion factor provided a relative measure from one case to the next of the propagation of carbon throughout the flowfield assuming the carbon plume originates at the origin, as it does in all cases in [145]. The plume expansion factor provided a direct relative measure of the expansion of carbon throughout the flowfield.

Varying the thermophysical characteristics of the background gas resulted in widely different plume development at similar points in time. Figs. §.38-40 indicate the difference in both leading edge propagation of the carbon plume for argon, helium, and N_2 background gases at 100 μs post-ablation time. The resulting plume expansion factors for the variation of background gases is seen in Fig. §.41, which shows that the higher the plume expansion factor, the lower the mass of recovered material from the laser ablation when compared to the experimental results of Arepalli et al [154]. Similar results were obtained for the other variations of background gas temperature, pressure, and the inner tube diameter of the laser ablation oven with one noticeable discrepancy – the case where the inner quartz tube was reduced from its nominal 1 inch diameter used in standard processing to a diameter of ½ inch. Experimental results showed that the narrower diameter case should result in a reduced quantity of mass being recovered from laser ablation, while the inverse relationship seen with the plume expansion factor plotted in Fig. §.42 indicates that the mass recovered should have been higher than the nominal one inch diameter case. With the exception of this one case, the plume expansion factor did provide the best "indicator" yet of the amount of ablative carbon material that could be recovered from laser ablation studies. However, the plume expansion factor did not provide a direct quantitative relationship for the carbon recovered, but it did provide a qualitative relative measure from one case to the next. A possible cause of this discrepancy may be the result of the high concentration of carbon in the small diameter case resulted in more absorption of laser energy by the ablation products. This reduced the energy flux to the target, resulting in less ablation.

Other results from the latest study [145] did provide thermal and species concentration profiles for the parametric variations that can be used in separate decoupled solutions with more complex chemical models (such as the Krestinin and Moravsky model in [8]) using the CHEMKIN software [40]. At the present time, Greendyke and Scott are continuing these decoupled studies with a refined grid mesh in the immediate ablation area of the carbon target for times ranging from ablation onset up to the first few microseconds after ablation onset. The flowfield solutions at different points in post-ablation onset times that result from this study can be combined into a single solution file via use of the *Tecplot®* [150] software. The resulting solution data file can then be input into the *CFD Analyzer™* [155] add-on feature to the Tecplot package. Once the user has specified the location of basic flowfield properties in the file, such as pressure and temperature, the *CFD Analyzer™* package can automatically integrate streaklines or particle trajectories over the time domain of the composite flowfield solution file. All flowfield properties and chemical compositions along the streaklines are then returned by the software for analysis with the decoupled methodology previously described. Results from decoupled calculations along streamlines will be discussed in the next section.

§.4.3 Chemical Kinetics Along Streak lines In Pulsed Laser Ablation

For CFD problems having more than one dimension, adding a large chemical kinetics model would overwhelm even supercomputers. Solutions would take days or weeks of computer time to solve. In many cases it is useful to decouple the problem and solve the fluid dynamics and energy equations without chemical reactions. The history of temperature, pressure, and mixing (dilution) with an external gas can be determined along streak lines. For steady state problems such as the arc or HiPco process, as was described in section §.5.3.1, one can easily integrate the position divided by velocity to obtain the time at corresponding points in the flow. The CFD solution provides all other properties, except the detailed chemical species. One can then use a chemical kinetics code, such as the AURORA code of CHEMKIN to solve the chemical rate equations along the streamline, as a function of time. For time dependent solutions of the flow equations, as is needed for dynamic situations such as the laser ablation process, a similar technique can be used to follow a sample "particle" of the flow as time evolves. However, the process requires having the solution at various times during the development of the flow. With these solutions described in **§.4.2** one can do a similar integration of the distance/velocity. For example, in some preliminary calculations we have the evolution of the solution along a number of streak lines that start next to the laser ablation target. These streak lines are shown in Fig. §.43. Integrating the distance divided by velocity we obtain the time interval between point and therefore the time at each location. Then we have the flow field properties as a function of time. The temperature (Fig. §.44) and pressure profiles were then input into the AURORA code to solve the chemical rate equations for the evolution of the species along the streak line. One such preliminary solution is shown in Fig. §.45 for the complete model along one of the streak lines. The rate coefficients for this calculation were not accurate; therefore, it only represents the methodology, not accurate results.

§.4.4 Conclusions from CFD Modeling

The present limitations of reduced carbon chemical reaction mechanisms and the resulting computational overhead that would result from higher-order chemistry models severely hinder the analysis of laser ablation SWNT production by CFD methods when CFD is used by itself. However, this does not mean that useful information for the study of SWNT production is unobtainable – the use of the plume expansion factor formulated by Greendyke, et al. [145] and outlined in the previous section does yield insight into the possible enhancement of SWNT production by aerodynamic means alone. The information provided – chemical profiles of "building block" species, temperature profiles, relative localized densities of the chemical species, etc. can provide input data for de-coupled studies with chemical reaction codes that do not have the dependency of CPU time on grid resolution and number of grid points considered. Indeed, it is possible that in the future, unconventional CFD methods such as Direct Simulation Monte Carlo methods [[157]], or molecular dynamics methods [[158]], could more completely simulate at least the initial onset of ablation in the flowfield since they do not have the same relationship between the number of chemical species and computational overhead – although such methods have difficulties of their own that make their use questionable at the present time.

§.5 Computational Simulation of the HiPco SWNT Production Process

A new method for the production of SWNT that is receiving much attention at the current time is the "High Pressure Carbon Monoxide" or HiPco process, first developed by Nikolaev, et al. [[159]]. Two of the main problems in the production of SWNT are the ability to produce them in economically viable quantities and to produce them with predetermined structures that have unique properties such as their chirality. While the HiPco process does not necessarily address the latter problem, it is a possible answer to the former. The HiPco process is a continuous gas production reactor that utilizes a relatively cold input stream of CO and iron pentacarbonyl, $Fe(CO)_5$, that is injected into the reactor with impinging streams of heated CO in a "showerhead" configuration (Fig. §.46). As the iron pentacarbonyl is heated by the impinging streams, it decomposes releasing the Fe atoms, which then condense into metallic iron clusters. The clusters serve as catalysts for SWNT development. The SWNT begin to develop from the iron clusters when CO molecules interact with the iron catalyst and form an iron cluster with the developing SWNT forming on it and CO_2 molecules.

Computational simulations of the HiPco using reacting-gas computational fluid dynamics (CFD) have not been common. One of the primary investigations into the process has been the work of Dateo, et al. [27] and Gökçen, et al. [19], who conducted extensive work first on a reduced chemical reaction model for the HiPco process and then combined this model with a simplified CFD code to produce a parametric analysis of the HiPco process. Work by other researchers such as Povitsky and Salas [[160]] have focused on the actual aerodynamics of the HiPco process to insure the best mixing of the iron pentacarbonyl and carbon monoxide streams for SWNT production. Scott, et al. [31] also conducted research on the HiPco process with limited CFD methods that utilized a chemical reaction model that is decoupled from the flowfield solution method.

§.5.1 Reacting Gas Modeling of the HiPco Process

Dateo, Gökçen and Meyyappan published a two-part paper [27,19] that modeled their chemical reaction mechanism [27] in the first part, and the application of that chemical reaction mechanism [19] couples with a CFD solution methodology for the analysis of the HiPco reactor chamber. The first paper established their chemical reaction mechanism that can be broken down into 3 fundamental parts: the decomposition of the iron pentacarbonyl steps, iron catalyst growth and evaporation, and finally, carbon nanotube formation.

Dateo, et al. noted that the iron pentacarbonyl will begin to decompose at temperatures above 500 K, which is the situation as the inlet $Fe(CO)_5$ stream initially encounters the hotter stream of CO. The decomposition mechanism is modeled in five steps:

$$Fe(CO)_5 \leftrightarrow Fe(CO)_4 + CO$$

$$Fe(CO)_4 \leftrightarrow Fe(CO)_3 + CO$$

$$Fe(CO)_3 \leftrightarrow Fe(CO)_2 + CO$$

$$Fe(CO)_2 \leftrightarrow FeCO + CO$$

$$FeCO + M \leftrightarrow Fe + CO + M$$

Chemical reaction rates for the dissociation were estimated by Dateo et al by use of experimental data from Lewis et al [161] and Engelking and Lineberger [162]. The reverse reaction rates were taken from Seder et al [163].

Iron cluster formation in the second part of their model was based upon the rates of Krestinin, et al. [29] wherein their model is based upon the reaction mechanisms:

$$Fe_m + Fe_n \rightarrow Fe_{m+n} \ (n=1\text{-}4)$$

$$Fe_m \rightarrow Fe_{m-1} + Fe$$

$$FeCO + Fe_m \rightarrow Fe_{m+1} + CO$$

$$FeCO + FeCO \rightarrow Fe_2 + 2CO$$

It is noted that iron evaporation will occur at higher temperatures, while the condensation of carbon into SWNT requires higher temperatures for proper formation.

Condensation of the carbon atoms is accomplished by a modification of the Boudouard reaction [164]:

$$2CO(g) \rightarrow C(s) + CO_2(g)$$

into the three-step process suggested by Boudart [165]:

$$Fe_m + CO \rightarrow Fe_m \bullet CO$$

$$Fe_m \bullet CO \rightarrow Fe_m + CO$$

$$Fe_m \bullet CO + CO \rightarrow Fe_m \bullet C_{NT} + CO_2$$

The final composition of the reaction model in [27] consists of 971 species in 1948 chemical reactions. Since computational effort in chemically reacting flowfields is proportional to the square of the number of species multiplied by the number of grid points, the initial model in [27] was reduced for CFD analysis. The reduction was accomplished by grouping the iron cluster species that contain three or more atoms of iron into a single species. This re-grouping of the iron related species results in a much more computationally feasible model that has 14 species and 22 reactions – well within the capabilities of most modern CFD codes.

Both the full and the reduced models were used in a simple "0-D" parametric study that examined variations of temperature, pressure and $Fe(CO)_5$ partial pressure at the gas injection interface. Dateo et al's main findings in part I of their paper [27] determined that increasing the temperature in the HiPco chamber speeds up the decomposition of the iron pentacarbonyl, but at the same time increases iron cluster evaporation. Increasing the pressure was found to speed up the Boudouard reaction and slow down iron pentacarbonyl decomposition. Increasing $Fe(CO)_5$ partial pressures speeds up both decomposition of the iron pentacarbonyl and the formation of iron clusters. When the reduced and full chemistry models were compared in the 0-d model, it was found that the two models gave acceptable comparison to each other over the range of parameters studied.

§.5.2 CFD Modeling of the HiPco Process

In part II of the work [19], Gökçen et al incorporated their reduced three-part chemical model for SWNT formation into a Navier-Stokes flowfield solver for axisymmetric nonequilibrium flows. The fundamental equations they used were expressed in vector form as:

$$\frac{\partial U}{\partial t}+\frac{\partial F}{\partial x}+\frac{1}{y}\frac{\partial (yG)}{\partial y}=W+\frac{H}{y} \qquad (\S.62)$$

where,

$$U=\begin{bmatrix}\rho\\ \rho_1\\ .\\ .\\ \rho_{14}\\ \rho u\\ \rho v\\ E\end{bmatrix}, \qquad F=\begin{bmatrix}\rho u\\ \rho_1 u+j_{1x}\\ .\\ .\\ \rho_{14}u+j_{14x}\\ \rho u^2+P+\tau_{xx}\\ \rho uv+\tau_{xy}\\ u(E+P+\tau_{xx})+v\tau_{xy}+q_x\end{bmatrix}$$

$$G=\begin{bmatrix}\rho v\\ \rho_1 v+j_{1y}\\ .\\ .\\ \rho_{14}v+j_{14y}\\ \rho uv+\tau_{xy}\\ \rho v^2+P+\tau_{yy}\\ v(E+P+\tau_{yy})+u\tau_{yx}+q_y\end{bmatrix}, \qquad W=\begin{bmatrix}w\\ w_1\\ .\\ .\\ w_{14}\\ 0\\ 0\\ 0\end{bmatrix}, \text{ and}$$

$$H = \begin{bmatrix} 0 \\ 0 \\ . \\ . \\ 0 \\ 0 \\ P + \tau_{\theta\theta} \\ 0 \end{bmatrix} \qquad (§.63)$$

The first 15 equations in the set represent the mass conservation equations for overall mass and the 14 species. The latter equations are the conservation of momentum in two directions and the conservation of energy equation. The H-vector reflects changes in the fundamental equations that are required by the axisymmetric geometry, and the W-vector term in the overall equation represents the source vector for chemistry effects. The equations were discretized into a finite-volume approach using a Steger-Warming flux-vector splitting [166]. The coupled gas dynamics and flowfield dynamics solution method utilized an implicit Gauss-Seidel relaxation method [166]. The domain of the HiPco reactor was split into two blocks, one modeling the inlet conical "showerhead" region, and the second for the cylindrical downstream portion of the flow. Laminar flow was assumed throughout the study.

Results from the CFD simulation showed that there was an optimum pressure and temperature for the growth and development of SWNT that agreed with their previous part I of their paper as stated in the previous section. In addition, the variations of temperature and pressure showed good agreement with experimental results. An interesting conclusion of their study, (not elaborated upon in the paper) is the belief that improved mixing in the flowfield domain of the HiPco reactor would not lead to greater iron cluster (and therefore SWNT) production. Gökçen, et al., however, allowed that work was needed to improve the chemical modeling before they could conclusively respond about mixing improvement.

§.5.3 Other HiPco Modeling Efforts

Povitsky and Salas [159] also attempted a CFD analysis of the HiPco flowfield regime with the goal of improving the mixing of the iron precursors. Their technique was to use a combination of an Eulerian-based flowfield solution code named FLUENT [167] for the Navier-Stokes solution of the flowfield without chemical reactions, and a Lagrangian solution method to track the particles of the flow and the resulting parameters of the flowfield through which they pass. The FLUENT code utilized a k-ε turbulence model in the solution procedure as implemented by Povitsky et al. In addition, FLUENT also provided the Lagrangian methodology for the particle trace simulations.

The primary purpose of the Povitsky work was to examine multiple geometric configurations of the HiPco reactor including the angle of the impinging CO jets and the number of jets utilized to determine the optimum configuration of the "showerhead" reactor chamber. An interesting result of their work showed that rapid mixing of the flow geometrically does not imply rapid temporal mixing of the flow. The best geometry for good heating of the iron precursor flow through the center of the reactor chamber was found to be a single central jet containing the precursor gas with three inlet jets for the heated CO with an angle of 45 (30?) degrees between the centerline and the impinging hot CO jets.

§.5.3.1 Production of SNWTs/CO_2

The solution to the chemical kinetics of nanotube production for the HiPco process was developed using two methods. In the first method, Dateo, et al [27] and Gökçen et al. [19] implemented their kinetics model first by applying it parametrically to constant temperature and pressure conditions. They then reduced the model and followed a similar procedure to show that their reduced model produced about the same amount of CO_2 as their full model. The then included these models in an axisymmetric full Navier-Stokes CFD solver and concluded that their reduced model adequately represented the results of the full model. (See details in **§.2.3.**) The second approach was a decoupled method in which Povitsky [168] solved Euler equations with a turbulence model to find streamlines. Scott, et al. [31] then used the solutions along streamlines the chemical kinetics code of CHEMKIN to find the evolution of CO_2 and other species in the HiPco reactor. They used the chemical reaction models developed by Dateo, et al. as well as investigated variations of those models. The time history of the temperature and dilution due to mixing were found along streamlines calculated by Povitsky [168] and Povitsky and Salas.[169] Sample stream paths are shown in Fig. §.47. The variations were developed to investigate the effect of various assumptions about the nucleation rate and the number of clusters in the model on carbon creation and cluster size distributions. Fig. 48 shows the evolution of carbon nanotubes attached to clusters of iron as a function of iron cluster size. One can see that at long times, the largest cluster starts to increase relative to the other clusters. This indicates that larger clusters should be included in the model. However, the amount of carbon nanotubes is dominated by the small cluster population. Therefore, from the standpoint of predicting carbon production, the model is quite adequate and does not need augmenting with larger metal clusters. However, the models tend to over predict the amount of carbon produced as compared with experiments, as seen in Fig. §.49.

§.5.3.2 Assessment of Nickel as Catalyst for HiPco

Due to the fact that iron tends to evaporate at fairly low temperatures, compared with nickel, it was anticipated that nickel might be a better catalyst for the HiPco reactor. However, when nickel tetracarbonyl was injected as the catalyst into the reactor, no carbon nanotubes were produced. The reason was not clear, since nickel is very effective in the arc and laser ablation processes. Modeling the nucleation and evaporation of metals allowed Scott and Smalley [42] to conclude that the higher binding energy and stability of nickel, as compared with iron was the principle factor that contributed to no growth of nanotubes when nickel-only was included as catalyst. A comparison of calculations of the production of SWNTs took into account iron-species rate coefficients and rate coefficients adjusted for the binding energies of nickel. It was found that almost no nanotubes were produced when the values corresponding to the nickel bond energies were used in the rate coefficients for evaporation and for the NiCO bond. It was found that the metal-CO bond energy has a major influence on the production of CO_2. The higher NiCO bond energy almost eliminates production of CO_2, whereas, the smaller bond energy of FeCO leads to significant production. Also, the rate of dimer dissociation and small cluster evaporation affects the production of CO_2 by limiting the rate of cluster growth, and thus the number of clusters available to catalyze SWNT growth. This suggests that if CO reacts with metal clusters and removes atoms from them by forming MeCO, which has the effect of enhancing the evaporation rate and reducing SWNT production. It appears that the stronger bond between nickel and CO tends to extract nickel from clusters. It is like an enhanced evaporation that prevents nickel cluster growth in high pressure CO. Therefore, very few clusters are formed that can catalyze SWNT formation and growth.

§.5.3.3 Production of Catalyst Particles Prior to Injection into HiPco Reactor

An investigation of a potential procedure for injecting premade catalyst particles was studied using models of the HiPco process. It was envisioned that a laser could dissociate $Fe(CO)_5$ in the injector of the HiPco apparatus. Laser dissociation instead of thermal dissociation would free iron atoms for nucleation and growth prior to mixing with hot CO. One might be able to control the size of the iron clusters and thus affect the production of SWNTs in a favorable way. Instead of fabricating the device, it would be reasonable just to be able to compute the results and assure that the experiment is worth building. A calculation was made assuming that all iron carbonyl is completely dissociated prior to injection into the main reactor. This is a truncated model (clusters up to n=40). The inlet flow is then allowed to relax to form iron clusters and iron clusters with CO attached. From Fig. 50, one can see that it takes about 0.1 to 1 ms for a fairly uniform distribution of iron clusters to form at this condition. The model only allows CO to bind to Fe_n clusters for $n>10$, therefore, the small clusters have no CO attached, whereas, the larger ones all have attached CO. The possibility of the clusters catalyzing SWNT formation depends on the residence time in the cool (400 K) zone. The design of the inlet can be tailored to meet a wide range of residence times by adjusting the inlet tube diameter and length. It is apparent that a CW laser might result in over heating, therefore, a pulsed laser might be better. It could be timed such that a slug of gas that is dissociated then flows into the main reactor in the time between pulses. Another adjustable parameter could be the partial pressure of $Fe(CO)_5$, controlled by controlling the temperature of its container. If small clusters are needed, then short residence times are indicated; but if larger clusters are needed, then longer residence times would be preferred.

§.6 Conclusions

Modeling of fullerene and carbon nanotube formation involves understanding how the species react chemically and evolve in time. Time evolution of conditions modeled using various degrees of fidelity in solving the fluid dynamics equations of motion through one degree or another using computational fluid dynamics. The kinetics involves knowing how they are formed from simpler species, that is, a concept of how they grow. This is not an easy question to answer, particularly in the case of single-walled carbon nanotubes. In this chapter, we have assumed the fullerene chemical kinetics model of Krestinin, et al. that was, to some extent, validated by comparisons with measured production. We have applied it to the arc process and the laser ablation process; and we have used it as the basis for carbon cluster growth in models of SWNT production. Growth of SWNTs requires the introduction of metal catalysts; and we included the nucleation and growth of nickel clusters to represent catalysts in arc and laser ablation processes. Unfortunately, the kinetics of nickel cluster growth is not well documented in the literature; therefore, we have taken extensive liberties to approximate the kinetics of nickel. We have posed the mechanisms of cluster formation and growth using the aerosol theory developed by Girshick, which essentially treats cluster growth as a kinetically controlled process. Evaporation of these clusters was treated in their theory as determined from knowledge of the bulk vapor pressure and surface tension. Several variations of the kinetics model of the HiPco process for SWNT production were reviewed. The essential results at the current stage of development indicate that these models can predict measured trends in production, but the absolute quantity of carbon (nanotubes) is over predicted.

We have reviewed various degrees of approximation in the kinetics models, and have shown attempts to reduce the size of HiPco and the carbon vapor models. Reasonable comparisons between the full and reduced models were shown.

It should be emphasized that the kinetics models are approximate and preliminary. They await validation and refinement based on comparisons with measurements. As pointed out, the nickel evaporation model can be refined by using measured cross sections and accounting for internal energy. It is possible that the intermediate clusters should be combinations of carbon and a few nickel atoms, rather than forming carbon, then nickel, followed by combining the two types of clusters. The present models show how we were guided by the observation that metal clusters are seen in the product. However, there are molecular dynamics models [170] that carbon and nickel co-condense. That model indicates further coalescence of nickel and carbon into larger cluster that may be followed by segregation of carbon from the metal catalysts. There are also some electron diffraction measurements that show crystalline metal carbides in the clusters seen in the product.

We have shown computational fluid dynamics models of the arc, laser ablation, and HiPco processes. The highest dimension of any of the calculations, thus far, is two-dimensional. It is apparent from experiment, that the flow fields are three-dimensional. Thus, future work should be extended to 3D for problems when he chemistry is decoupled from the flow field. However, it appears that even 1D calculations can yield important insight and understanding of the flow and its chemical kinetic

§.6 Acknowledgements

The authors would like to thank Ivaylo Hinkov for his help in the preparation of this manuscript.

Table Captions

Table §.19 Soot nuclei and soot particles reaction rates. Data from Krestinin and Moravskii [119]

Table §.20 Surface reaction considered in Farhat et al. [110]

Table §.21 Calculated number densities of small carbon clusters and fullerenes at three positions in the arc (- symbol indicates negligible density). Conditions are Helium with P= 660 mbar, I=100 A, d_{AC}=3 mm, and the dilution factor τ=20.

Table §.22 Simplified Carbon Chemistry Model used in laser ablation simulation

Table 13 Refs.
171
172
173
174

Page intentionally left blank

Figure Captions

Fig. §.1 Comparison of iron cluster evaporation rate coefficients at 1380 K versus number of atoms in nickel clusters.

Fig. §.2 Iron cluster recombination rates at 1500 K. Iron atoms attaching to clusters of size n-1 forming clusters of n-atoms.

Fig. §.3 Nanotube bundles emanating from a nickel/cobalt catalyst particle. (Courtesy A. P. Moravsky, MER Corp.)

Fig. §.4 Nanotube bundles emanating from catalyst particles. (Courtesy A. Loiseau) J. Gavillet et al, *Carbon* 40 (2002) 1649-1663. [41]

Fig. §.5 Carbon cluster and SWNT production for full model (with modified rates) compared with reduced model with temperature ramp from 3500 to 1500 K in 1 μs.

Fig. §.6 Comparison of cluster evolution and production of SWNTs with full model (with modified rates) and the reduced model with temperature ramp from 3500 to 1500 K in 500 μs.

Fig. §.7 MER's industrial reactor of capacity ~100 g SWNT soot per hour. On the left, it shows soot containing up to 20 wt% of nanotubes.

Fig. §.8. Schematic of ideal structures (a) and imprities (b) in the collected arc materials.

Fig. §.9. Krätschmer and Huffman arc reactor.

Fig. §.10 Micrograph of the as produced collaret in the arc chamber; a and b are SEM micrographs at two magnifications [110] showing bundles of SWNTs and impurities obtained with catalyst composition Ni:Y 4.2:1 atomic percent. C) is a high resolution HRTEM of the collaret produced in helium showing bundle of about 60 nanotubes. [171]

Fig. §.11 Space charge potential a dielectric field distribution in the arc.

Fig. §.12 Development of the plasma in the interelectrode zone between the cathode on the left and the anode of 6 mm diameter on the right. [116]

Fig. §.13 Measured optical emission spectra showing the predominance of yttrium ions.[7]

Fig. §.14. Calculated nickel and yttrium spectra. [50]

Fig. §.15 Schematic representation of a well mixed plasma reactor [120] and its adaptation to predict plasma compositions Y_i for given T and T_e. [116]

Fig. §.16 Predicted variations of ions mass fractions with the total current intensity. [116]

Fig. §.17. Plasma characteristics calculated by AURORA in the conditions $T_g=T_{ion}=6500$ K and variable T_e. Hatched zone corresponds to the optimal domain of current intensity 80-120 A for nanotube synthesis. [116]

Fig. §.18 Time evolution of carbon atom mole fraction calculated in helium, at P=660 mbar and T=4000 K.

Fig. §.19 Time evolution of some carbon cluster mole fraction calculated in helium, at P=660 mbar and T=2000 K.

Fig. §.20 Time evolution of fullerene mole fraction calculated in helium, at P=660 mbar and T=2000 K.

Fig. §.21-a. Mole fractions of small carbon species calculated at equilibrium versus temperature calculated in helium at 660 mbar.

Fig. §.21-b. Total fullerene yield versus temperature calculated in helium at 660 mbar.

Fig. §.22 Schematic of the flow issuing from the electric arc zone as represented by Krestinin and Moravsky. [111,7,119]

Fig. §.23 Comparison of experimental and calculated yield of fullerenes versus the pressure [8]. The experimental molar ratio C_{70}/C_{60} is found to be invariably equal to 0.2.

Fig. §.24 Simulation domain and boundary conditions.

Fig. §.25 African calabash with structure decorated by hexagons and opened on the top.

Fig. §.26 Gas-Phase species reacting at the edge of an open nanotube and top view of growing bundles of nanotubes showing surface site density.

Fig. §.27 Calculated temperature profile in the inter-electrode gap of the arc. Conditions are He, P=660 mbar and I=100 A.

Fig. §.28 Calculated axial distribution of small carbon clusters and fullerenes in the inter-electrode gap of the arc. Conditions are He, P=660 mbar, I=100 A, dilution factor $\tau=20$.

Fig. §.45 Example of evolution of species mass fractions along streak line in laser ablation. Arbitrary evaporation rate coefficients were used in calculation, therefore, data is not accurate, but only shown as an example of methodology.

Fig. §.46 Schematic of a generalized "showerhead" HiPco reactor chamber.

Fig. §.47 X- and Y-coordinates along four typical streamlines versus the axial coordinate Z, in mixing zone of HiPco reactor, calculated by the FLUENT code.

Fig. §.48 Carbon nanotube cluster distributions at various times in trajectory no. inj0 of HiPco reactor. Published as Fig. 11 in *JNN* Vol. 3 No. 1/2 pp. 63-73 (2003).

Fig. §.49 Calculated and measured iron fraction in product of HiPco reactor. Published as Fig. 12 in *JNN* Vol. 3 No. 1/2 pp. 63-73 (2003).

Fig. §.50 Iron cluster distribution at various times in inlet to HiPco reactor, starting from fully dissociated iron pentacarbonyl at 35 atmospheres and 400 K.

References

---

[1] H. W. Kroto, J. R. Heath, S. C. O'Brien, R. F. Curl and R. E. Smalley. Nature, **318**, 162 (1985).

[2] W. Krätschmer, L. D. Lamb, K. Fostiropoulos, D. R. Huffman, *Nature* **347** 354 1990.

[3] J. Bernholc and J.C. Phillips, *Phys. Rev. B.,* **33** 7395 (1986)

[4] W.R. Creasy and J.T. Brenna, *Chem. Phys.*, **126** 453 (1988)

[5] W.R. Creasy and J.T. Brenna, *J. Chem. Phys.* **92** 2269 (1990)

[6] W.R. Creasy, *J. Chem. Phys.,* **92** No. 12, 7223 (1990)

[7] A.V.Krestinin, A.P.Moravskii, and P.A.Tesner, *Chemical Physics Reports*, v.17, No.9, 1687 (**1998**).

[8] A. V. Krestinin and A. P. Moravsky, *Chem. Phys. Lett.* 286 479 (**1998**).

[9] G. Von Helden, M.-T. Hsu, N. Gotts, and M.T. Bowers, *J.Phys. Chem.* **86** p. 8182- (1993)

[10] G. Von Helden, N. Gotts, and M.T. Bowers, *Nature* **363** 60 (1993)

[11] J.M. Hunter, J.L. Fye, and N.F. Jarrold, *J. Chem. Phys.* **99** 1785 (1993)

[12] J.M. Hunter, J.L. Fye, E. J. Roskamp, and N.F. Jarrold, *J. Phys. Chem.* **98** 1810 (1994)

[13] P.P. Radi, T.L. Bunn, P.R. Kemper, M.E. Molchan, and M.T. Bowers, *J. Chem. Phys.* **88** 2809 (1988)

[14] C.D. Scott, *J. Nanosci.and Nanotech.* Accepted for publication (2004)

[15] *Termodinamicheskie Svolstva Individual'nykh Veshchest. Spravochnik* (Thermodynamic Properties of Individual Materials. Handbook), V.P. Glushko, Ed. (Nauka, Moscow, 1978) Vol. 2, Book 1

[16] R.S. Udahl, Y. Bao, and W.M. Jackson, *Chem. Phys. Lett.* 178 425 (1991)

[17] J.M.L. Martin, J.P. Francois, and R. Gijbels, *J. Chem. Phys.* **95** 9420 (1991)

[18] C.J. Pope and J.B. Howard, *J. Phys. Chem.* **99** 4306 (1995)

[19] T. Gökçen, C.E. Dateo, and M. Meyyappan, *J. Nanosci. Nanotech.,* **2** No. 5, 535 (2002)

[20] S.L. Girshick, C.-P. Chiu, and P.H. McMurry, *Plasma Chemistry and Plasma Processing,* **8** No. 2 145 (1988)

[21] S.L. Girshick and C.-P. Chiu, *Plasma Chemistry and Plasma Processing,* **9** No. 3 355 (1989)

[22] S.L. Girshick, C.-P. Chiu, and P.H. McMurry, *Aerosol Science and Technology,* **13** 465 (1990)

[23] S.L. Girshick and C.-P. Chiu, *J. Chem. Phys.* **93** No. 2 1273 (1990)

[24] S.L. Girshick, *J. Chem. Phys.* **94** No. 1 826 (1991)

[25] S.L. Girshick, C.-P. Chiu,, R. Muno, C.Y. Wu, L. Yang, S.K. Singh, and P.H. McMurry, *J. Aerosol Sci.* **24** No. 3 367 (1993)

[26] N. Rao, S. Girshick, J. Heberlein, P. McMurry, S. Jones, D. Hansen, and B. Micheel, *Plasma Chemistry and Plasma Processing*, **15** No. 4 581 (1995)

[27] C.D. Scott, A. Povitsky, C.E. Dateo, T. Gökçen, P.A. Willis, and R.E. Smalley, *J. Nanosci. Nanotech.,* **3** no. 1/2, 63 (2003)

[28] C.E. Dateo, T. Gökçen, and M. Meyyappan, *J. Nanosci. Nanotech.,* **2** No. 5, 523 (2002)

[29] A.V. Krestinin, V.N. Smirnov, and I.S. Zaslonko, *Sov. J. Chem. Phys.*, **8** No. 3, 689 (1991)

[30] P.A. Vlasov, I.S. Zaslonko, and Yu.K. Karasevich, *High Temperature* **36** No. 2, 189 (1998)

[31] K.E. Lewis, D.M. Golden, and G.P. Smith, *J. Amer. Chem. Soc.*, **106** No. 14, 3905 (1984)

[32] V.N. Smirnov, *Kinetics and Catalysis*, **34** No. 4 391 (1992)

[33] P.A. Vlasov, I.S. Zaslonko, Yu. K. Karasevich, and V. N. Smirnov, *Kinetics and Catalysis* **40** No. 5 611 (1999)

[34] M.D. Rumminger, D. Reinelt, V. Babushok, and G.T. Linteris, *Combust. Flame*, **116** 207 (1999)

[35] T.A. Seder, A.J. Ouderkirk, and E. Weitz, *J. Chem. Phys.* **85**, 1977 (1986)

[36] L.S. Sunderlin, D. Wang, and R. R. Squires, *J. Am. Chem. Soc.* **114**, 2788 (1992)

[37] A. Ricca, *Chem. Phys. Lett.* **350** 313 (2001)

[38] E.K. Parks, K.P. Kerns, and S.J. Riley, *J. Chem. Phys.* **112** No. 7, 3384 (2000)

[39] K.P. Kerns, E.K. Parks, and S.J. Riley, *J. Chem. Phys.* **112** No. 7, 3394 (2000)

[40] Kee, R.J., Rupley, F.M., Miller, J.A., Coltrin, M.E., Grcar, J.F., Meeks, E., Moffat, H.K., Lutz, A.E., Dixon-Lewis, G., Smooke, M.D., Warnatz, J., Evans, G.H., Larson, R.S., Mitchell, R.E., Petzold, L.R., Reynolds, W.C., Caracotsios, M., Stewart, W.E., Glarborg, P., Wang, C., and Adigun, O., CHEMKIN Collection, Release 3.6, Reaction Design, Inc., San Diego, CA, 2001.

---

[41] J. Gavillet, A. Loisear, F. Ducastelle, S. Thair, P. Bernier, O. Stephan, J. Thibault, and J.-C. Charlier, *Carbon* **40** 1649 (2002).

[42] C.D. Scott and R.E. Smalley, *J. Nanosci. And Nanotech.* **3** No. 1/2 75 (2003)

[43] L. Lian, C.-X. Su, and P.B. Armentrout, *J. Chem. Phys.* **96** No. 10, pp. 7542 (1992)

[44] P.B. Armentrout, *Annu. Rev. Phys. Chem.* **52** . 423 (2001)

[45] Ebbesen, T.W., Ajayan, P.M., *Nature* **358**, 220 (1992).

[46] Journet, C., Maser, W.K., Bernier, P., Loiseau, A., Lamy de La Chapelle, M., Lefrant, S., Deniard, P., Lee, R., Fischer, J.E., *Nature* **388**, 756 (1997).

[47] Huczko, A., Lange, H., Resztak, A., Byszewski, P., *High Temp. Chem. Process.* **4**, 125 (1995).

[48] Huczko, A., Lange, H., Byszewski, P., Poplawsks, M., Starski, A., *J. Phys. Chem. A* **101**, 1267 (1997).

[49] P. Byszewski, H. Lange, A. Huczko and J. F. Behnke, *J. Phys. Chem. Solids* **58**, 11, **(1997)**.

[50] C. D. Scott, S. Farhat, and I. Hinkov, "Analysis of Emission Spectra From Arc in Production of Single-Wall Carbon Nanotubes", Internal LIMHP Report **(2002)**.

[51] S. Akita, H. Ashihara and Y. Nakayama, *Jpn. J. Appl. Phys.* **39,** 4939 **(2000)**.

[52] Farhat, S., Lamy de La Chapelle, M., Loiseau, A., Scott, C.D., Lefrant, S., Journet, C., Bernier, P., *J. Chem. Phys.* **115**, 10 (2001).

[53] Hafner, J. H., Bronikowski, M.J., Azamian, B.R., Nikolaev, P., Rinzler, A.G., Colbert, D.T., Smith, K.A., Smalley, R.E., *Chem. Phys. Lett.* **296**, 195 (1998).

[54] Satishkumar, B.C., Govindaraj, A., Sen, R., Rao, C.N.R., *Chem. Phys. Lett.* 293, 47 (1998).

[55] Colomer, J.-F., Benoit, J.-M., Stephan, C., Lefrant, S., Van Tendeloo, G., Nagy, J.B., *Chem. Phys. Lett.* **345**, 11 (2001).

[56] Cheng, H.M., Li, F., Sun, X., Brown, S.D.M., Pimenta, M.A., Marucci, A., Dresselhaus, G., Dresselhaus, M.S., *Chem. Phys. Lett.* **289**, 602 (1998).

[57] Peigney, A., Laurent, C., Dobigeon, F., Rousset, A., *J. Mater. Res.* **12**, 613 (1997).

[58] Dai, H., Rinzler, A.G., Nikolaev, P., Thess, A., Colbert, D.T., Smalley, R.E., *Chem. Phys. Lett.* **260**, 471 (1996).

[59] Wang, Y., Wei, F., Luo, G., Yu, H., Gu, G., *Chem. Phys. Lett.* **364**, 568 (2002).

[60] Wang, Y., Zhang, Z., Liu, H., Xu, X., Pa, G., Guo, Z., Liu, Y., Han, X., Lan, G., *Spectrochimica Acta Part A* **58**, 2089 (2002).

[61] M. E. Itkis, D. E. Perea, S. Niyogi, S. M. Rickard, M. A. Hamon, H. Hu, B. Zhao, and R. C. Haddon, *Nano Lett.* 3, 309 **(2003)**.

[62] T. Guo and R. E. Smalley, in *Recent Advances in the Chemistry and Physics of Fullerenes and Related Materials*. Electrochem. Soc, Pennington, NJ, USA. Reno, Nevada (1995).

[63] A. Thess, R. Lee, P. Nikolaev, H. J. Dai, P. Petit, J. Robert, C. H. Xu, T. H. Lee, S. G. Kim, A. G. Rinzler, D. T. Colbert, G. E. Scuseria, D. Tomanek, J. E. Fischer, and R. E. Smalley, Science 273, 483 (1996).

[64] R. Sen, A. Govindaraj, and C. N. R. Rao, *Chem. Phys. Lett.* **267**, 276 **(1997)**.

[65] H. M. Cheng, F. Li, G. Su, H. Y. Pan, L. L. He, X. Sun, and M. S. Dresselhaus, *Appl. Phys. Lett.* **72**, 3282 **(1998)**.

[66] H. M. Cheng, F. Li, X. Sun, S. D. M. Brown, M. A. Pimenta, A. Marucci, G. Dresselhaus, and M. S. Dresselhaus, *Chem. Phys. Lett.* **289**, 602 **(1998)**.

[67] G. G. Tibbetts, D. W. Gorkiewicz, and R. L. Alig, *Carbon* **31**, 809 **(1993)**.

[68] P. Nikolaev, M. J. Bronikowski, R. K. Bradley, F. Rohmund, D. T. Colbert, K. A. Smith, and R. E. Smalley, *Chem. Phys. Lett.* **313**, 91 (1999).

[69] K. Bradley, "Large Scale Production of Single Wall Carbon Nanotubes", PhD Thesis, Rice University, (2000).

[70] A history of welding : http://www.weldinghistory.org/htmlhistory/wh_index.html.

[71] Iijima, S., Nature **354**, 56 (1991).

[72] Iijima, S., *Mater. Sci. Eng. B* **19**, 172 (1993)

[73] Can we eliminate this ref and insert Bethune's after the Iijima refs?
Iijima, S., Ichihashi, T., Ando, Y., *Nature* **356**, 776 (1992).

[74] Iijima, S., Ichihashi, T., *Nature* **363**, 503 (1993).

[75] Bethune, D. S., C. H. Chang, M.S. DeVries, G. Gorman, R. Savoy, J. Vazquez, and R. Beyers, *Nature* **363** 605 (1993).

[76] 35 Ajayan, P.M., Iijima, S., *Nature* **358**, 23 (1992).

---

[77] 34 Bacsa, W. S., Ugarte, D., Chatelain, A., De Heer, W., *Phys. Rev. B* **50**, 15473 (1994).

[78] 36 Zhang, H., Wang, D., Xue, X., Chen, B., Peng, S., *J. Phys. D* **30**, L1 (1997).

[79] Cadek, M., Murphy, R., McCarthy, B., Drury, A., Lahr, B., Barklie, R.C., Panhuis, M., Coleman, J.N., Blau, W.J., *Carbon* **40**, 923 (2002).

[80] Borisenko, D.N., Kolesnikov, N.N., Kulakov, M.P., Kveder, V.V., *Int. J. Nanosc.* **1**, 235 (2002).

[81] Ando, Y., Zhao, X., Inoue, S., Iijima, S., *J. of Crystal Growth* **237-239** 1926 (2002).

[82] Zhao, X., Ohkohchi, M., Wang, M., Iijima, S., Ichihashi, T., Ando, Y., *Carbon* **35**, 775 (1997).

[83] Hutchison, J.L., Kiselev, N.A., Krinichnaya, *et al.*, *Carbon* **39**, 761 (2001).

[84] Jung, S.H., Kim, M.R., Jeong, S.H., *et al.*, *Appl. Phys. A* **76**, 285 (2003).

[85] Ishigami, M., Cumings, J., Zettl, A., Chen, S., *Chem. Phys. Lett.* **319**, 457 (2000).

[86] Zhu, H.W., Li, X.S., Jiang, B., Xu, C.L., Zhu, Y.F., Wu, D.H., Chen, X.H., *Chem. Phys. Lett.* **366**, 664 (2002).

[87] Saito, Y., Yoshikawa, T., Inagaki, M., Tomita, M., Hayashi, T., *Chem. Phys. Lett.* **204**, 277 (1993).

[88] Yudaska, M., Komatsu, T., Ichihashi, T., Achiba, Y., Iijima, S., *J. Phys. Chem. B* **102**, 4892 (1998).

[89] Ajayan, P.M., Colliex, C., Lambert, J.M., Bernier, P., Barbedette, L., Tence, M., Stephan, O., *Phys. Rev. Lett.* **72**, 1722 (1994).

[90] Saito, Y., Okuda, M., Yoshikawa, T., Bandow, S., Yamamuro, S., Wakoh, K., Sumiyama, K., *Jpn. J. Appl. Phys.* **33**, L186 (1994).

[91] Ruoff, R.S,. Lorents, D.C., Chan, B., Malhotra, R., Subramoney, S., *Science* **259**, 346 (1993).

[92] Bandow, S., Saito, Y., *Jpn. J. Appl. Phys. Pt. 2,* **32**, L1677 (1993).

[93] Yosida, Y., *Appl. Phys. Lett.* **62**, 3447 (1993).

[94] Majetich, S.A., McHenry, M.E., Artman, J.O., Nuhfer, N.T., Staley, S.W., *Phys. Rev. B* **48**, 16845 (1993).

[95] Ando, Y., Whao, X., *Mol. Cryst. Liq. Cryst* **340**, 707 (2000)

[96] Takizawa, M., Bandow, S., Torii, T., Iijima, S., *Chem. Phys. Lett.* **302**, 146 (1999).

[97] Kim, G.T., Park, J.G., Park, Y.W., Liu, K., Düsberg, G., Roth, S., *Synth. Met.* **103**, 2551 (1999).

[98] Seraphin, S., Zhou, D., *Appl. Phys. Lett.* **64**, 2087 (1994).

[99] Saito, Y., Koyama, T., Kawabata, K., *Z. Phys. D* **40**, 421 (1997).

[100] Saito, Y., Tani, Y., Miyagawa, N., Mitsushima, K., Kasuya, A., Nishina, Y., *Chem. Phys. Lett.* **294**, 593 (1998).

[101] Sugai, T., Omote, H., Bandow, S., Tanaka, N., Shinohara, H., *J. Chem. Phys.* **112**, 6000 (2000).

[102] Lee, S.J., Baik, H.K., Yoo, J., Han, J.H., *Diam. Rel. Mat.* **11**, 914 (2002).

[103] Bae, J.C., Yoon, Y.J., Lee S.-J., Song, K.M., Baik, H.K., *Carbon* **40**, 2905 (2002).

[104] Kanai, M., Koshio, A., Shinohara, H., *et al.*, *Appl. Phys. Lett.* **79**, 2967 (2001).

[105] Zhang, H., Xue, X., Wang, D., He, Y., Peng, Sh., *Mat. Chem. Phys.* **58**, 1 (1999).

[106] Takizawa, M., Bandow, S., Yudasaka, M., Ando, Y., Shimoyama, H., Iijima, S., *Chem. Phys. Lett.* **326**, 351 (2000).

[107] 65 Ebbesen T. W., *Carbon nanotubes, Preparation and Properties*, edited by T. W. Ebbesen, CRC Press, Inc. **(1997).**

[108] Farhat S, Hinkov I. And Carl D. Scott, To be published in *Journal of Nanoscience and Nanotechnology*, 2004.

[109] 73 Krestinin A.V., A.P.Moravskii, *Chemical Physics Reports*, **18**, No.3, .515 **(1999).**

[110] 75 Ebbesen T. W., *Ann. Rev. Mater. Sci.* **24**, 235 (1994)

[111] Ebbesen T. W., H. Hiura, J. Fujita, Y. Ochiai, S. Matsui and K. Tanigaki, *Chem. Phys. Lett.*, **209**, 83 (1993)

[112] 77 Gamaly, E.G., Ebbesen, T.W., *Phys. Rev. B* **52**, 2083 (1995).

[113] 78 Bilodeau, J.-F., Pousse, J., Gleizes, A., *Plasma Chem. and Plasma Proc.* **18**, 285 (1998).

[114] 68 I. Hinkov, PhD thesis, University Paris 13, France, (2004)

[115] 79 Scott C. D. Report on Trip to LIMHP Université Paris 13, 21 October 2003 – 19 November 2003, 2003.

[116] 80 Smalley R.E., *Mater. Sci. Eng. B* **19**, 1 (1993).

[117] 88 1. A. V. Krestinin, A. P. Moravsky, "Dynamics of Fullerene Formation in a Carbon Arc Process," personal communication. The data cited in this communication combines the data from two papers in Russian published in "*Khimicheskaya Fizika*" issued as a version in English named "Chemical Physics Reports". Those two papers in English are Ref. 108 and 7.

---

[118] 81 Meeks E., Moffat H. K., Grcar J. F., and Kee R. J., *AURORA: A FORTRAN Program for Modeling Well Stirred Plasma and Thermal Reactors with Gas and Surface Reactions*, Release 3.6, Reaction Design, Inc., San Diego, CA (2001).

[119] 82 Gurvich, L.V., Iorish V.S., et al. *IVTANTHERMO - A Thermodynamic Database and Software System for the Personal Computer. User's Guide.* (CRC Press, Inc., Boca Raton, 1993).

[120] 90 JANAF, "Thermochemical tables, National Standards Reference Data Series"Report NSRDS-NBS : Dow Chemikal Company, distributer by Clearinghouse for federal Scientific and Technical Information, PB168370 (1965).

[121] 91 B. J. McBride and S. Gordon, "FORTRAN IV Program for Calculation of Thermodynamic Data" NASA Report NASA TN-4097 **(1967)**.

[122] 89 Hindmarsh, A. C., ODEPACK, " A Systematized Collection of ODE Solvers, Scientific Computing, R. S. Stepleman et al. (eds.), Amsterdam, 55-64 (1983).

[123] G. N. Abramovich, *Applied Gas Dynamics*, Nauka, Moscow (1969).

[124] 95 38. T. G. Owano, HTGL Report No. T-279, "Non-Equilibrium behavior in a flowing, atmospheric pressure plasma," Stanford University **(1991)**.

[125] 96 B. W. Yu and S. L. Girshick, *J. Appl. Phys.* **75**, 8 **(1994)**.

[126] 97 D. G. Goodwin, *J. Appl. Phys.* **74** 6888 **(1993)**.

[127] 98 A. Peigney, Ch. Laurent, E. Flahaut, R. Bacsa, A. Rousset, *Carbon*, **39** 507, **(2001).**

[128] 99 H. Kataura, Y. Kumazawa, Y. Maniwa, Y. Ohtsuka, R. Sen, S. Suzuki, Y. Achiba, *Carbon* **38**, 1691 **(2000)**.

[129] 100 A. A. Puretzky, D. B. Geohegan, H. Schittenhelm, X. Fan, M. A. Guillorn, *App. Surf. Science* **552**, 197 **(2002)**.

[130] 102 Patankar S. V., *Numerical Heat Transfer and Fluid Flow, McGraw-Hill*, New York (1980).

[131] 1 Hirsch, C., *Numerical Computation of Internal and External Flows, Vol. 1: Fundamentals of Numerical Discretization*, Wiley and Sons, 1990.

[132] 2 Hirsch, C., *Numerical Computation of Internal and External Flows, Vol. 2: Computational Methods for Inviscid and Viscous Flows*, Wiley and Sons, 1990

[133] 3 Hoffman, K.A. and Chiang, S.T., *Computational Fluid Dynamics for Engineers*, Vol. 1 & 2, Engineering Education System, Wichita, 1993.

[134] 4 Lobao, D.C., and Povitsky, A., AIAA Paper 2003-3923, 33rd AIAA Fluid Dynamics Conference, Orlando FL, June 2003.

[135] 5 Hoffman, K.A., Chiang, S.T., Siddiqui, S., and Papadakis, M., *Fundamental Equations of Fluid Mechanics,* Engineering Education System, Wichita, 1996.

[136] 6 Puretzky, A.A., Geohegan, D.B., Fan, X., and Pennycook, S.J., *Applied Physics A*, **70**, No. 2, February 2000.

[137] 7 Greendyke, R.B., (Hyman, W., Sickorez, D., Miller, M., and Tarkington, W., Editors), NASA Contractor Report on Grants NAG 9-39 and 9-54, Vol. 1, pp. 10-1 to 10-14, Summer 2001.

[138] 8 Greendyke, R.B. and Scott, C.D., Annual APS March Meeting 2002, Indianapolis, IN, March 2002.

[139] 9 Greendyke, R.B., Scott, C.D., and Swain, J., AIAA 2002-3026, AIAA/ASME 8th Joint Thermophysics and Heat Transfer Conference, St. Louis, MO, June 2002.

[140] 10 Greendyke, R.B., Swain, J., and Scott, C.D., NASA/Rice University Workshop on SWNT Growth Mechanisms (Invited speaker/author), Boerne Texas, Feb. 27-March 2 2003.

[141] 11 Greendyke, R.B., Swain, J., and Scott, C.D., Accepted in *The Journal of Nanoscience and Nanotechnology* (2004)

[142] 12 Greendyke, R.B., Swain, J.E., Stein, T., Ray, L., and Scott, C.D., AIAA Paper 2004-0807, AIAA 42nd Aerospace Sciences Meeting, Reno NV, January 2004.

143 13 White, J.A. and Morrison, J.H., AIAA 99-3360, June 1999. (Also see: http://vulcan-cfd.larc.nasa.gov)

144 14 Wilcox, D.C., *Turbulence Modeling for CFD*, 2nd Ed., DCW Industries, Inc., 1998.

145 15 Jameson, A., Schmidt, W., and Turkel, E., AIAA Paper 81-1259, June 1981.

146 16 Laney, C.B., *Computational Gasdynamics*, Cambridge University Press, 1998.

147 17 http://capella.colorado.edu/~laney/home.htm

148 20 Mesh Generator™ *Users Manual, Amtec Engineering Inc.*, Bellevue WA, 1999 (see also http://www.amtec.com).

---

[149] 21 Tecplot® *User's Manual – Version 9.2, Release 1*, Amtec Engineering Inc., Bellevue WA, 2002 (see also http://www.amtec.com).

[150] 22 http://www.openchannelfoundation.org/projects/PLOT3D

[151] 24 Arepalli, S., Holmes, W.A., Nikolaev, P., Hadjiev, V.G., and Scott, C.D., Accepted for publication, *J. Nanoscience and Nanotechnology*, 2004.

[152] CFD Analyzer™ User's Manual, Version 3.0, Amtec Engineering Inc., Bellevue, WA, 2002.

[153] 25 Bird, G.A., *Molecular Gas Dynamics and the Direct Simulation of Gas Flows*, Oxford University Press, 1994.

[154] 26 Frenkel, D. and Smit, B., *Understanding Molecular Simulation*, 2nd Ed., Academic Press, 2002.

[155] 1 Nikolaev, P., Bronikowski, M.J., Bradley, R.K., Rohumond, F., Colbert, D.T., Smith, K.A., and Smalley, R.E., *Chem. Phy. Lett.*, **313**, 91, (1999)

[156] 4 Povitsky, A., and Salas, M.D., *AIAA Journal*, **41**, Nov. 2003 (tentative).

[157] 6 Lewis, K.E., Golden, D.M., and Smith, G.P., *J. Am. Chem. Soc.*, **106**, 3905, (1984).

[158] 7 Engelking, P.C. and Lineberger, W.C., *J. Am. Chem. Soc.*, **101**, 5569, (1979).

[159] 8 Seder, T.A., Ouderkirk, A.J., and Weitz, E., *J. Chem. Phys.*, **85**, 1977, (1986).

[160] 10 Boudouard, G., *Ann. Chem. Phys.*, **24**, 5, (1901).

[161] 11 Boudart, M., *AIChE J.*, **18**, 465, (1972).

[162] 12 Laney, C.B., *Computational Gasdynamics*, Cambridge University Press, 1998.

[163] 13 Fluent Inc., *FLUENT 5.0 Users Manual*, 2000 (See also: http://www.fluent.com)

[164] A. Povitsky, ICASE Report 2000-18, *Computers and Fluids (International Journal)*, accepted for publication, 2001.

[165] A. Povitsky and M. Salas, ICASE Report No. 2001-04, NASA CR 2001-210662, Feb. 2001.

[166] S. Maruyama and Y. Shibuta, *Molecular Crystals and Liquid Crystals,* **387** 87 (2002)

[167] Muñoz, E., Maser, W.K., Benito, A.M., Martinez, M.T., De la Fuente, G.F., Maniette, Y., *Carbon* **38**, 1445 (2000).

[168] Foutel-Richard, A., PhD thesis, CNAM, France (2003).

[169] Guillard, T., Cetout, S., Flamant, G., Laplaze, D., *J. Mat. Science* **35**, 419 (2000).

[170] Laplaze, D., Bernier, P., Maser, W.K., Flamant, G., Guillard, T., Loiseau, A., *Carbon* **36**, 685 (1998).

[171] Hinkov, I., Grand, J., Lamy de la Chapelle, M., Farhat, S., Scott, C.D., Nikolaev, P., Pichot, V., Launois, P., Mevellec, J.Y., Lefrant, S., *J. Appl. Phys.*, **95** (4) (2004)

Table §.1. Gas phase chemistry for Fullerene Model*

Reaction	A(cm^3/s/moles)	β	E/R(K)
1. Chemistry of small clusters ($C_1 - C_{10}$)			
$C + C \leftrightarrow C_2$	2.00×10^{14}	0	0
$C + C2 \leftrightarrow C_3$	2.00×10^{14}	0	0
$C_2 + C_2 \leftrightarrow C_3 + C$	2.00×10^{15}	0	9040
$C_2 + C_2 \leftrightarrow C_4$	2.00×10^{14}	0	0
$C_1 + C_3 \leftrightarrow C_4$	2.00×10^{14}	0	0
$C_1 + C_4 \leftrightarrow C_5$	2.00×10^{14}	0	0
$C_2 + C_3 \leftrightarrow C_5$	2.00×10^{14}	0	0
$C_{n-m} + C_m \leftrightarrow C_n$	2.00×10^{14}	0	0
n=6,10 and m=1,n/2			
2. Chemistry of cycles and polycycles ($C_{11} - C_{31}$)			
$C_{n-m} + C_m \leftrightarrow C_n$	2.00×10^{14}	0	0
n=11,31 and m=1,15			
3. Formation of fullerenes			
$C_{n-m} + C_m \leftrightarrow C_n$	2.00×10^{14}	0	0
n=32,46 and $n-31 \leq m \leq 15$			
4. Growth of fullerenes shells			
$C_n + C \leftrightarrow C_{n+1}$	2.00×10^{14}	0	0
n=32,78 excluding n=59,69			
$C_n + C_2 \rightarrow C_{n+2}$	4.00×10^{08}	0	0
$C_{n+2} \rightarrow C_n + C_2$	3.20×10^{13}	0	61900
n=32,59 excluding n=58			
$C_n + C_2 \rightarrow C_{n+2}$	4.00×10^{08}	0	0
$C_{n+2} \rightarrow C_n + C_2$	3.20×10^{13}	0	61900
n=60,77 excluding n=68			
$C_n + C_3 \leftrightarrow C_{n+2} + C$	1.00×10^{15}	0	0
n=32,77			
5. Formation and decay of fullerenes molecules			
$C_{60} \rightarrow C_{60F}$	5.00×10^{13}	0	37745
$C_{59} + C \rightarrow C_{60F}$	2.00×10^{14}	0	0
$C_{58} + C_2 \rightarrow C_{60F}$	4.00×10^{08}	0	-30196
$C_{60F} \rightarrow C_{58} + C_2$	8.00×10^{12}	0	61900
$C_{58} + C_3 \rightarrow C_{60F} + C$	8.00×10^{14}	0	0
$C_{60F} + C \rightarrow C_{61}$	2.00×10^{13}	0	10065
$C_{60F} + C_2 \rightarrow C_{62}$	2.00×10^{13}	0	10065
$C_{60F} + C_3 \rightarrow C_{63}$	2.00×10^{13}	0	10065
$C_{70} \rightarrow C_{70F}$	1.20×10^{13}	0	37745
$C_{69} + C \rightarrow C_{70F}$	2.00×10^{14}	0	0
$C_{68} + C_2 \rightarrow C_{70F}$	4.00×10^{08}	0	-30600
$C_{70F} \rightarrow C_{68} + C_2$	2.50×10^{14}	0	0
$C_{68} + C_3 \rightarrow C_{70F} + C$	1.40×10^{11}	0	49925
$C_{70F} + C \rightarrow C_{71}$	2.00×10^{13}	0	10065

$C_{70F} + C_2 \rightarrow C_{72}$	2.00×10^{13}	0	10065
$C_{70F} + C_3 \rightarrow C_{72} + C$	2.00×10^{13}	0	10065

* Forward rate constants k are calculated assuming Arrhenius temperature dependence $k = AT^{\beta}\exp(-\frac{E}{RT})$ where A is the pre-exponential factor, β is the temperature exponent and E is the activation energy. Constants A, β and E are from Krestinin, et al. [7].

Table §.2 Thermodynamic Coefficients for Carbon Clusters

H= 1000 to 20000 K
L= 300 to 1000 K

i	A_{1i}	A_{2i}	A_{3i}	A_{4i}	A_{5i}	A_{6i}	A_{7i}
1H	2.3205176E+00	1.8268312E-04	-3.1504542E-08	2.5371109E-12	-6.2267852E-17	8.4851595E+04	5.8203836E+00
1L	1.9031864E+00	4.0200238E-03	-9.0395391E-06	8.1759092E-09	-2.5854092E-12	8.4826660E+04	7.2917617E+00
2H	4.0753780E+00	3.3239978E-04	-1.2344909E-08	-7.0714041E-13	2.8222317E-17	9.9788114E+04	9.6847543E-01
2L	5.4993641E+00	1.8891470E-03	-1.3226503E-05	1.6061423E-08	-5.8286773E-12	9.9140682E+04	-7.7146073E+00
3H	4.9032746E+00	1.1113409E-03	-7.5331984E-08	-4.8099305E-13	8.9121604E-17	9.6812289E+04	1.5052816E-01
3L	3.6042014E+00	7.5373711E-03	-1.1558984E-05	8.8850242E-09	-2.5287216E-12	9.7010617E+04	6.1103710E+00
4H	4.9032746E+00	1.1113409E-03	-7.5331984E-08	-4.8099305E-13	8.9121604E-17	1.1492855E+05	1.5052816E-01
4L	3.6042014E+00	7.5373711E-03	-1.1558984E-05	8.8850242E-09	-2.5287216E-12	1.1512688E+05	6.1103710E+00
5H	1.1592118E+01	8.5502931E-04	-1.2817463E-07	7.7473555E-12	-1.6260603E-16	1.1368121E+05	-3.5115388E+01
5L	1.1731935E+01	-2.5681572E-02	7.8642726E-05	-7.8483519E-08	2.6116987E-11	1.1495211E+05	-2.9295593E+01
6	16	0	0	0	0	149572	-61.28986
7	19	0	0	0	0	157121	-77.6175
8	22	0	0	0	0	178812	-93.94515
9	25	0	0	0	0	186965	-110.2728
10	28	0	0	0	0	178963	-126.6004
11	31	0	0	0	0	181413.9	-142.9281
12	34	0	0	0	0	183864.9	-159.2557
13	37	0	0	0	0	186315.8	-175.5834
14	40	0	0	0	0	188766.8	-191.911
15	43	0	0	0	0	191217.7	-208.2387
16	46	0	0	0	0	193668.6	-224.5663
17	49	0	0	0	0	196119.6	-240.894
18	52	0	0	0	0	198570.5	-257.2216
19	55	0	0	0	0	201021.5	-273.5493
20	58	0	0	0	0	203472.4	-289.8769
21	61	0	0	0	0	205923.3	-306.2045
22	64	0	0	0	0	208374.3	-322.5322
23	67	0	0	0	0	210825.2	-338.8598
24	70	0	0	0	0	213276.2	-355.1874
25	73	0	0	0	0	215727.1	-371.5151
26	76	0	0	0	0	218178	-387.8427
27	79	0	0	0	0	220629	-404.1704
28	82	0	0	0	0	223079.9	-420.498
29	85	0	0	0	0	225530.9	-436.8257
30	88	0	0	0	0	227981.8	-453.1533
31	91	0	0	0	0	230432.7	-469.481
32	94	0	0	0	0	232883.7	-485.8086
33	97	0	0	0	0	265530.6	-502.1362
34	100	0	0	0	0	237785.6	-518.4639
35	103	0	0	0	0	270432.5	-534.7916
36	106	0	0	0	0	242687.4	-551.1192
37	109	0	0	0	0	275334.4	-567.4468
38	112	0	0	0	0	247589.3	-583.7745
39	115	0	0	0	0	280236.3	-600.1021
40	118	0	0	0	0	252491.2	-616.4297
41	121	0	0	0	0	285138.1	-632.7574
42	124	0	0	0	0	257393.1	-649.085
43	127	0	0	0	0	290040	-665.4127
44	130	0	0	0	0	262295	-681.7403
45	133	0	0	0	0	294941.9	-698.068

46	136	0	0	0	0	267196.8	-714.3956
47	139	0	0	0	0	299843.8	-730.7233
48	142	0	0	0	0	272098.7	-747.051
49	145	0	0	0	0	304745.7	-763.3785
50	148	0	0	0	0	277000.6	-779.7062
51	151	0	0	0	0	309647.5	-796.0338
52	154	0	0	0	0	281902.5	-812.3615
53	157	0	0	0	0	314549.4	-828.6891
54	160	0	0	0	0	286804.4	-845.0168
55	163	0	0	0	0	319451.3	-861.3444
56	166	0	0	0	0	291706.3	-877.6721
57	169	0	0	0	0	324353.2	-893.9997
58	172	0	0	0	0	296608.1	-910.3274
59	175	0	0	0	0	329255.1	-926.655
60H	9.9843418E+01	7.8857558E-02	-3.0608799E-05	5.1957690E-09	-3.2188408E-13	2.6670488E+05	-5.4587488E+02
60L	-3.3579084E+01	4.2844440E-01	-3.1712321E-04	4.7546257E-08	2.7677699E-11	3.0465122E+05	1.4832875E+02
61	181	0	0	0	0	334156.9	-959.3103
62	184	0	0	0	0	306411.9	-975.638
63	187	0	0	0	0	339058.8	-991.9655
64	190	0	0	0	0	311313.8	-1008.293
65	193	0	0	0	0	343960.7	-1024.621
66	196	0	0	0	0	316215.6	-1040.949
67	199	0	0	0	0	348862.6	-1057.276
68	202	0	0	0	0	321117.5	-1073.604
69	205	0	0	0	0	353764.4	-1089.931
70H	1.0677602E+02	1.0200334E-01	-3.9562455E-05	6.7122022E-09	-4.1568097E-13	2.9769320E+05	-5.9941734E+02
70L	-3.1366983E+01	3.3484410E-01	9.8587783E-05	-4.4663983E-07	2.2008836E-10	3.4260294E+05	1.4891614E+02
71	211	0	0	0	0	358666.3	-1122.587
72	214	0	0	0	0	330921.3	-1138.914
73	217	0	0	0	0	363568.2	-1155.242
74	220	0	0	0	0	335823.2	-1171.57
75	223	0	0	0	0	368470.1	-1187.897
76	226	0	0	0	0	340725	-1204.225
77	229	0	0	0	0	373372	-1220.553
78	232	0	0	0	0	345626.9	-1236.88
79	235	0	0	0	0	378273.9	-1253.208
80	238	0	0	0	0	350528.8	-1269.536

Table §.3 – Reduced Fullerene model reaction scheme

	A	η	E/R
Cluster Growth			
C + C = C_2	2.0E+14	0.	0.
C + C_2 = C_3	2.0E+14	0.	0.
C2 + C_2 = C_3 + C	2.0E+15	0.	9040.
C3 + C = 0.100CC	2.0E+13	0.	0.
C3 + C_2 = 0.125CC	2.0E+13	0.	0.0
C3 + C_3 = 0.150CC	2.0E+13	0.	0.0
CC + C = 1.025CC	2.3E+14	0.	0.0
CC + C_2 => 1.05CC	2.3E+14	0.	0.0
CC => 0.95CC + C_2	3.2E+13	0.	61900.
Fullerene formation			
CC + C_3 => 0.70C_{60F} + C	2.0E+13	0.	0.
CC + C_2 => 0.70C_{60F}	4.0E+9	0.	-30196.
CC + C => 0.6833333C_{60F}	2.0E+13	0.	0.
Fullerene disintegration			
C_{60F} => 1.45CC + C2	8.0E+13	0.	61900.
Soot formation			
CC + CC => Z	4.0E+13	0.	0.
CC + C_2 => 0.525Z	4.0E+8	0.	-30600.
CC + C_3 => 0.5375Z	6.92E+10	0.5	0.
C_{60F} + Z => 1.75Z	1.26E+12	0.	10098.
CC + C_3 => 0.525Z + C	2.0E+11	0.	0.
Z + C_3 => 1.0375Z	4.0E+12	0.	0.
Z + C_2 => 1.025Z	4.0E+12	0.	0.
Z + C => 1.0125Z	4.0E+12	0.	0.

Table §.4 Thermodynamic Property NASA Coefficients Reduced Fullerene Model plus some other species used in plasma simulations

```
AR                IVTAN AR  1               G   300.000 20000.000 1000.00      1
 0.25199477E+01-0.22858382E-04 0.74655237E-08-0.90208251E-12 0.36063733E-16    2
-0.75393340E+03 0.42492779E+01 0.25670200E+01-0.44283132E-03 0.98495011E-06    3
-0.88424193E-09 0.27879189E-12-0.75176371E+03 0.40801018E+01                   4
C             GMcB 20K 0C   1               G   300.000 20000.000 1000.00      1
 0.23205176E+01 0.18268312E-03-0.31504542E-07 0.25371109E-11-0.62267852E-16    2
 0.84851595E+05 0.58203836E+01 0.19031864E+01 0.40200238E-02-0.90395391E-05    3
 0.81759092E-08-0.25854092E-11 0.84826660E+05 0.72917617E+01                   4
C2            GMcB 20K 0C   2               G   300.000 20000.000 1000.00      1
 0.40753780E+01 0.33239978E-03-0.12344909E-07-0.70714041E-12 0.28222317E-16    2
 0.99788114E+05 0.96847543E+00 0.54993641E+01 0.18891470E-02-0.13226503E-04    3
 0.16061423E-07-0.58286773E-11 0.99140682E+05-0.77146073E+01                   4
C3            GMcB 20K 0C   3               G   300.000 20000.000 1000.00      1
 0.49032746E+01 0.11113409E-02-0.75331984E-07-0.48099305E-12 0.89121604E-16    2
 0.96812289E+05 0.15052816E+00 0.36042014E+01 0.75373711E-02-0.11558984E-04    3
 0.88850242E-08-0.25287216E-11 0.97010617E+05 0.61103710E+01                   4
C60F                    C  60    0    0     G  0300.00   5000.00   1000.00      1
  0.1780000E+03  0.0000000E+00  0.0000000E+00  0.0000000E+00  0.0000000E+00    2
  0.3015100E+06 -0.9429827E+03  0.1780000E+03  0.0000000E+00  0.0000000E+00    3
  0.0000000E+00  0.0000000E+00  0.3015100E+06 -0.9429827E+03                   4
CC                      C  40               G   300.000  5000.000 1000.00      1
  0.1180000E+03  0.0000000E+00  0.0000000E+00  0.0000000E+00  0.0000000E+00    2
  0.2524912E+06 -0.6164297E+03  0.1180000E+03  0.0000000E+00  0.0000000E+00    3
  0.0000000E+00  0.0000000E+00  0.2524912E+06 -0.6164297E+03                   4
Z                       C  80    0    0     G  0300.00   5000.00   1000.00      1
  0.2380000E+03  0.0000000E+00  0.0000000E+00  0.0000000E+00  0.0000000E+00    2
  0.3505288E+06 -0.1269536E+04  0.2380000E+03  0.0000000E+00  0.0000000E+00    3
  0.0000000E+00  0.0000000E+00  0.3505288E+06 -0.1269536E+04                   4

Plasma Species
Ni            GMcB 20K 0Ni  1               G   300.000 20000.000 1000.00      1
 0.36971152E+01-0.82867716E-03 0.18628604E-06-0.11986930E-10 0.23752778E-15    2
 0.50060051E+05 0.72075154E+00 0.42140643E+01-0.10224755E-01 0.25272825E-04    3
-0.24064628E-07 0.78454681E-11 0.50323075E+05 0.58841215E-01                   4
Ni+           GMcB 20K 0Ni  1E  -1          G   300.000 20000.000 1000.00      1
 0.21013259E+01 0.71871149E-03-0.11060734E-06 0.67741068E-11-0.13425799E-15    2
 0.14040022E+06 0.89762594E+01 0.12260499E+00 0.14956310E-01-0.30951078E-04    3
 0.26889803E-07-0.83015704E-11 0.14047983E+06 0.16941765E+02                   4
Y             IV 25K   0Y   1               G   300.000 25000.000 1000.00      1
 0.79437350E+00 0.13579116E-02-0.12031792E-06 0.31899976E-11-0.15582902E-16    2
 0.51410499E+05 0.18158732E+02-0.66965149E+01 0.65805915E-01-0.14851900E-03    3
 0.13342009E-06-0.41975353E-10 0.51184455E+05 0.45676826E+02                   4
Y+                     0Y   1E  -1          G   300.000 25000.000 1000.00      1
 0.30001765E+01 0.19353870E-04 0.10693682E-07-0.93577306E-12 0.20474488E-16    2
 0.12272102E+06 0.46280979E+01-0.10156546E+02 0.94627761E-01-0.20487420E-03    3
 0.17857051E-06-0.55138220E-10 0.12325328E+06 0.57606297E+02                   4
C+            GMcB 20K 0C   1E  -1          G   300.000 20000.000 1000.00      1
 0.25063181E+01 0.16390834E-05-0.41024961E-08 0.78583063E-12-0.23326192E-16    2
 0.21547022E+06 0.43269073E+01 0.26069164E+01-0.48079487E-03 0.83960952E-06    3
-0.64172956E-09 0.18061570E-12 0.21545410E+06 0.38615888E+01                   4
C4+               121286C   4E  -1          G  0300.00   5000.00   1000.00      1
 0.06500180E+02 0.04228632E-01-0.01790717E-04 0.03404812E-08-0.02403978E-12    2
 0.24662108E+06-0.11488894E+02 0.02343028E+02 0.16429811E-01-0.15279858E-04    3
 0.07343826E-07-0.15822743E-11 0.24662184E+06 0.09826204E+02                   4
C5+               121286C   5E  -1          G  0300.00   5000.00   1000.00      1
 0.08078081E+02 0.05743464E-01-0.02436405E-04 0.04638916E-08-0.03278909E-12    2
```

```
 0.23886116E+06-0.01953023E+03 0.02115273E+02 0.02326331E+00-0.02109499E-03    3
 0.09072734E-07-0.15400926E-11 0.23886181E+06 0.10976027E+02                   4
```

```
C4            GMcB 20K 0C   4               G   300.000 20000.000 1000.00      1
 0.49032746E+01 0.11113409E-02-0.75331984E-07-0.48099305E-12 0.89121604E-16    2
 0.11492855E+06 0.15052816E+00 0.36042014E+01 0.75373711E-02-0.11558984E-04    3
 0.88850242E-08-0.25287216E-11 0.11512688E+06 0.61103710E+01                   4
C5            GMcB 20K 0C   5               G   300.000 20000.000 1000.00      1
 0.11592118E+02 0.85502931E-03-0.12817463E-06 0.77473555E-11-0.16260603E-15    2
 0.11368121E+06-0.35115388E+02 0.11731935E+02-0.25681572E-01 0.78642726E-04    3
-0.78483519E-07 0.26116987E-10 0.11495211E+06-0.29295593E+02                   4
```

```
HE                120186HE  1               G  0300.00   5000.00  1000.00      1
 0.02500000E+02 0.00000000E+00 0.00000000E+00 0.00000000E+00 0.00000000E+00    2
-0.07453750E+04 0.09153489E+01 0.02500000E+02 0.00000000E+00 0.00000000E+00    3
 0.00000000E+00 0.00000000E+00-0.07453750E+04 0.09153488E+01                   4
```

Table §.5 Iron Carbonyl and Iron Cluster Model of Krestinin, Smirnov, and Zaslonko [29]

1. Iron Carbonyl Reactions (Krestinin, et al.)	A	η	Ea/R
Fe(CO)5 => FeCO + 4CO	2.0E+15	0.0	20130.9
FeCO => Fe + CO	6.0E+14	0.0	10317.1
Fe + CO + M => FeCO + M	5.0E+14	0.0	0.0
2. Fe Nucleation			
FeCO + FeCO => Fe2 + CO + CO	6.0E+14	0.0	1006.5
FeCO + Fe => Fe2 + CO	6.0E+14	0.0	0.0
Fe + Fe + M => Fe2 + M	6.0E+14	0.0	0.0
3a. Formation small clusters			
Fe2 + FeCO => Fe3 + CO	6.0E+14	0.0	0.0
Fe3 + FeCO => Fe4 + CO	6.0E+14	0.0	0.0
Fe4 + FeCO => Fe5 + CO	6.0E+14	0.0	0.0
Fe2 + Fe + M => Fe3 + M	5.0E+15	0.0	0.0
Fe3 + Fe => Fe4	5.0E+11	0.0	0.0
Fe4 + Fe => Fe5	3.0E+13	0.0	0.0
3b. Evaporation of small clusters			
Fe2 + M => Fe + Fe + M	1E15 (1E16)	0.0	16104.7
Fe3 + M => Fe2 + Fe + M	1E16 (1E17)	0.0	22143.9
Fe4 => Fe3 + Fe	1E13 (2E13)	0.0	27679.9
Fe5 => Fe4 + Fe	2E14 (7E14)	0.0	30699.5
Fe6 => Fe5 + Fe	2E15 (4E15)	0.0	32712.6
Fe7 => Fe6 + Fe	5E15 (1E16)	0.0	33719.2
Fe8 => Fe7 + Fe	1E16 (2E16)	0.0	34222.4
Fe9 => Fe8 + Fe	4E16 (4E16)	0.0	35229.0
3. Fe-atom Exchange			
Fe2 + Fe2 => Fe3 + Fe	3.0E+14	0.0	0.0
Fe2 + Fe3 => Fe4 + Fe	3.0E+14	0.0	0.0
4. Coagulation of small clusters			
Fe2 + Fe2 => Fe4	5.0E+13	0.0	0.0
Fe2 + Fe3 => Fe5	1.0E+14	0.0	0.0
Fe2 + Fe4 => Fe6	3.0E+14	0.0	0.0
Fe3 + Fe3 => Fe6	3.0E+14	0.0	0.0
Fe3 + Fe4 => Fe7	3.0E+14	0.0	0.0
Fe4 + Fe4 => Fe8	3.0E+14	0.0	0.0
5. Heterogeneous reaction in the c-phase (n>=5)			
Fe + Fen => Fe(n+1)	2.3E+13	0.0	0.0
FeCO + Fen => Fe(n+1) + CO	2.3E+13	0.0	0.0
Fe2 + Fen => Fe(n+2)	2.3E+13	0.0	0.0
Fe3 + Fen => Fe(n+3)	2.3E+13	0.0	0.0
Fe4 + Fen => Fe(n+4)	2.3E+13	0.0	0.0

Fen + Fem => Fe(n+m)	k_{nm}	0.0	0.0

$$k_{nm} = Z_{11}\left(\left(n^{1/3} + m^{1/3}\right)/2\right)^2 \left((n+m)/2nm\right)^{1/2}$$

Table §.6 Rate coefficients for iron pentacarbonyl decomposition and recombination

	High Pressure Ames[a]			High Pressure Smirnov[b]			Low Pressure (fall off) Smirnov[b]		
Reaction	A(mol,cm^3, s)	η	E/R (K)	A(mol,cm^3, s)	η	E/R (K)	A(mol,cm^3, s)	η	E/R (K)
$Fe(CO)_5 \rightarrow Fe(CO)_4 + CO$	$4.62X10^{20}$	-1.96	21028.3	$4.26X10^{20}$	-1.85	20447.	$1.22X10^{73}$	-16.78	20447.
$Fe(CO)_4 + CO \rightarrow Fe(CO)_5$[c]	$3.50X10^{10}$	0.	0.						
$Fe(CO)_4 \rightarrow Fe(CO)_3 + CO$	$6.96X10^{22}$	-2.14	14346.3	$2.85X10^{21}$	-1.87	16598.	$2.89X10^{57}$	-12.41	16598.
$Fe(CO)_3 + CO \rightarrow Fe(CO)_4$[c]	$1.30X10^{13}$	0.	.0						
$Fe(CO)_3 \rightarrow Fe(CO)_2 + CO$	$8.70X10^{19}$	-1.58	14679.8	$2.09X10^{21}$	-1.85	17921.	$2.10X10^{47}$	-9.11	17921.
$Fe(CO)_2 + CO \rightarrow Fe(CO)_3$[c]	$1.80X10^{13}$	0.	0.						
$Fe(CO)_2 \rightarrow FeCO + CO$	$3.96X10^{21}$	-2.29	18799.4	$4.07X10^{19}$	-1.46	13110.	$7.92X10^{33}$	-5.4	13110.
$FeCO + CO \rightarrow Fe(CO)_2$[c]	$1.50X10^{13}$	0.	0.						
$FeCO + M \rightarrow Fe + CO + M$	$4.87X10^{19}$	-0.90	2874.5	$1.073X10^{23}$	-2.6	6495.	$1.073X10^{23}$	-2.6	6495.
$Fe + CO + M \rightarrow FeCO + M$[d]	$1.00X10^{15}$	0.	0.						

[a] Ref. [28]

[b] Ref. [32]

[c] Ref. [35]

[d] Ref. [34]

Table §.7 Fits to Vlasov Fig. 2 Recombination Rates

Fe3	+ Fe =>	Fe4	1.28E+10	0.5	0
Fe4	+ Fe =>	Fe5	1.70E+10	0.5	0
Fe5	+ Fe =>	Fe6	2.24E+10	0.5	0
Fe6	+ Fe =>	Fe7	2.89E+10	0.5	0
Fe7	+ Fe =>	Fe8	1.73E+11	0.5	0
Fe8	+ Fe =>	Fe9	2.53E+11	0.5	0
Fe9	+ Fe =>	Fe10	3.18E+11	0.5	0
Fe10	+ Fe =>	Fe11	3.90E+11	0.5	0
Fe11	+ Fe =>	Fe12	4.71E+11	0.5	0
Fe12	+ Fe =>	Fe13	5.60E+11	0.5	0
Fe13	+ Fe =>	Fe14	6.57E+11	0.5	0
Fe14	+ Fe =>	Fe15	7.63E+11	0.5	0
Fe15	+ Fe =>	Fe16	8.77E+11	0.5	0
Fe16	+ Fe =>	Fe17	1.00E+12	0.5	0
Fe17	+ Fe =>	Fe18	1.13E+12	0.5	0
Fe18	+ Fe =>	Fe19	1.27E+12	0.5	0
Fe19	+ Fe =>	Fe20	1.42E+12	0.5	0
Fe20	+ Fe =>	Fe21	1.58E+12	0.5	0
Fe21	+ Fe =>	Fe22	1.74E+12	0.5	0
Fe22	+ Fe =>	Fe23	1.92E+12	0.5	0
Fe23	+ Fe =>	Fe24	2.11E+12	0.5	0
Fe24	+ Fe =>	Fe25	2.30E+12	0.5	0
Fe25	+ Fe =>	Fe26	2.50E+12	0.5	0
Fe26	+ Fe =>	Fe27	2.72E+12	0.5	0
Fe27	+ Fe =>	Fe28	2.94E+12	0.5	0
Fe28	+ Fe =>	Fe29	3.17E+12	0.5	0
Fe29	+ Fe =>	Fe30	3.41E+12	0.5	0
Fe30	+ Fe =>	Fe31	3.66E+12	0.5	0
Fe31	+ Fe =>	Fe32	3.92E+12	0.5	0
Fe32	+ Fe =>	Fe33	4.19E+12	0.5	0
Fe33	+ Fe =>	Fe34	4.47E+12	0.5	0
Fe34	+ Fe =>	Fe35	4.76E+12	0.5	0
Fe35	+ Fe =>	Fe36	5.06E+12	0.5	0
Fe36	+ Fe =>	Fe37	5.37E+12	0.5	0
Fe37	+ Fe =>	Fe38	5.69E+12	0.5	0
Fe38	+ Fe =>	Fe39	6.01E+12	0.5	0
Fe39	+ Fe =>	Fe40	6.35E+12	0.5	0
Fe40	+ Fe =>	Fe41	6.70E+12	0.5	0
Fe41	+ Fe =>	Fe42	7.06E+12	0.5	0
Fe42	+ Fe =>	Fe43	7.43E+12	0.5	0
Fe43	+ Fe =>	Fe44	7.81E+12	0.5	0
Fe44	+ Fe =>	Fe45	8.19E+12	0.5	0
Fe45	+ Fe =>	Fe46	8.59E+12	0.5	0
Fe46	+ Fe =>	Fe47	9.00E+12	0.5	0

```
Fe47    + Fe =>        Fe48    9.42E+12      0.5    0
Fe48    + Fe =>        Fe49    9.85E+12      0.5    0
Fe49    + Fe =>        Fe50    1.03E+13      0.5    0
Fe50    + Fe =>        Fe51    1.07E+13      0.5    0
! Fits to Vlasov Evaporation Rates
Fe4     =>     Fe3     + Fe    4.255E+13     0      24660
Fe5     =>     Fe4     + Fe    4.323E+13     0      24720
Fe6     =>     Fe5     + Fe    4.574E+13     0      36140
Fe7     =>     Fe6     + Fe    5.287E+13     0      34380
Fe8     =>     Fe7     + Fe    5.196E+13     0      25020
Fe9     =>     Fe8     + Fe    5.562E+13     0      31990
Fe10    =>     Fe9     + Fe    5.859E+13     0      31250
Fe11    =>     Fe10    + Fe    7.06E+13      0      35970
Fe12    =>     Fe11    + Fe    5.095E+13     0      38700
Fe13    =>     Fe12    + Fe    5.875E+13     0      47940
Fe14    =>     Fe13    + Fe    6.321E+13     0      32840
Fe15    =>     Fe14    + Fe    6.45E+13      0      41610
Fe16    =>     Fe15    + Fe    6.178E+13     0      37050
Fe17    =>     Fe16    + Fe    7.468E+13     0      35380
Fe18    =>     Fe17    + Fe    6.98E+13      0      34180
Fe19    =>     Fe18    + Fe    7.509E+13     0      40220
Fe20    =>     Fe19    + Fe    7.076E+13     0      38380
Fe21    =>     Fe20    + Fe    7.40298E+13   0      38617.6229
Fe22    =>     Fe21    + Fe    7.59216E+13   0      38769.36455
Fe23    =>     Fe22    + Fe    7.78134E+13   0      38914.9169
Fe24    =>     Fe23    + Fe    7.97052E+13   0      39054.78564
Fe25    =>     Fe24    + Fe    8.1109E+13    0      39206
Fe26    =>     Fe25    + Fe    8.34888E+13   0      39319.20281
Fe27    =>     Fe26    + Fe    8.53806E+13   0      39444.49644
Fe28    =>     Fe27    + Fe    8.72724E+13   0      39565.61064
Fe29    =>     Fe28    + Fe    8.91642E+13   0      39682.82685
Fe30    =>     Fe29    + Fe    9.1372E+13    0      39856
Fe31    =>     Fe30    + Fe    9.29478E+13   0      39906.55531
Fe32    =>     Fe31    + Fe    9.48396E+13   0      40013.50488
Fe33    =>     Fe32    + Fe    9.67314E+13   0      40117.43669
Fe34    =>     Fe33    + Fe    9.86232E+13   0      40218.52357
Fe35    =>     Fe34    + Fe    1.0377E+14    0      40423
Fe36    =>     Fe35    + Fe    1.02407E+14   0      40412.78232
Fe37    =>     Fe36    + Fe    1.04299E+14   0      40506.23296
Fe38    =>     Fe37    + Fe    1.0619E+14    0      40597.39881
Fe39    =>     Fe38    + Fe    1.08082E+14   0      40686.39369
Fe40    =>     Fe39    + Fe    1.09974E+14   0      40773.32304
Fe41    =>     Fe40    + Fe    1.11866E+14   0      40858.28466
Fe42    =>     Fe41    + Fe    1.13758E+14   0      40941.36951
Fe43    =>     Fe42    + Fe    1.15649E+14   0      41022.66227
Fe44    =>     Fe43    + Fe    1.17541E+14   0      41102.24195
```

Fe45	=>	Fe44	+ Fe	1.19433E+14	0	41180.18238
Fe46	=>	Fe45	+ Fe	1.21325E+14	0	41256.55265
Fe47	=>	Fe46	+ Fe	1.23217E+14	0	41331.41751
Fe48	=>	Fe47	+ Fe	1.25108E+14	0	41404.83774
Fe49	=>	Fe48	+ Fe	1.2529E+14	0	41377
Fe50	=>	Fe49	+ Fe	1.28892E+14	0	41547.56942

Table §.8 Full iron pentacarbonyl and iron cluster HiPco model of Dateo, et al. [28]

Thermal Decomposition and Formation of Small Iron Clusters from FeCO Fragment

Reaction	A (mol,cm^3, s)		E_a/k (K)	
1. Ames Carbonyl Rates				
$Fe(CO)_5$ => $Fe(CO)_4$ + CO	4.620E+20	-1.96	21028.30	
$Fe(CO)_4$ + CO => $Fe(CO)_5$	3.500E+10	0.00	0.00	
$Fe(CO)_4$ => $Fe(CO)_3$ + CO	6.960E+22	-2.14	14346.30	
$Fe(CO)_3$ + CO => $Fe(CO)_4$	1.300E+13	0.00	0.00	
$Fe(CO)_3$ => $Fe(CO)_2$ + CO	8.700E+19	-1.58	14679.80	
$Fe(CO)_2$ + CO => $Fe(CO)_3$	1.800E+13	0.00	0.00	
$Fe(CO)_2$ => FeCO + CO	3.960E+21	-2.29	18799.40	
FeCO + CO => $Fe(CO)_2$	1.500E+13	0.00	0.00	
FeCO + M => Fe + CO + M	4.870E+19	-0.90	2874.50	
Fe + CO + M => FeCO + M	1.000E+15	0	0	Krestinin
2 Formation and Growth of Small Iron Clusters				
Fe + Fe + M => Fe_2 + M	4.00E+15	0	0	
Fe_2 + Fe(+ M) => Fe_3 (+ M)	5.00E+15	0	0	
Krestinin Recombination Rates				
Fe_3 + Fe => Fe_4	5.10E+11	0	0.00E+00	
Fe_4 + Fe => Fe_5	3.00E+13	0	0.00E+00	
Fe_5 + Fe => Fe_6	1.10E+12	0	0.00E+00	
Fe_6 + Fe => Fe_7	1.50E+12	0	0.00E+00	
Fe_7 + Fe => Fe_8	7.90E+12	0	0.00E+00	
Fe_8 + Fe => Fe_9	1.00E+13	0	0.00E+00	
Fe_9 + Fe => Fe_{10}	1.30E+13	0	0.00E+00	
3. Thermal Decomposition of Small Iron Clusters				
Krestinin				
Fe_2 + M => Fe + Fe + M	1.00E+15	0	16102.93	
Fe_3 + M => Fe_2 + Fe + M	1.00E+16	0	22141.54	
Fe4 => Fe_3 + Fe	1.00E+13	0	27676.92	
Fe5 => Fe4 + Fe	2.00E+14	0	30696.22	
Fe6 => Fe5 + Fe	2.00E+15	0	32709.09	
Fe7 => Fe6 + Fe	5.00E+15	0	33715.52	
Fe8 => Fe7 + Fe	1.00E+16	0	34218.74	
Fe9 => Fe8 + Fe	4.00E+16	0	35225.17	
4. Coagulation of Small Iron Clusters				
Fe_2 + Fe_2 => Fe4	5.00E+13	0	0	
Fe_2 + Fe_3 => Fe5	1.00E+14	0	0	
Fe_2 + Fe_2 => Fe_3 + Fe	3.00E+14	0	0	
Fe_2 + Fe_3 => Fe4 + Fe	3.00E+14	0	0	
Fe_2 + Fe_4 => Fe_6	3.00E+14	0	0	
Fe_3 + Fe_3 => Fe_6	3.00E+14	0	0	
Fe_3 + Fe_4 => Fe_7	3.00E+14	0	0	
Fe4 + Fe_4 => Fe_8	3.00E+14	0	0	
Fe_2 + Fe_5 => Fe_7	2.30E+13	0	0	
Fe_2 + Fe_6 => Fe_8	2.30E+13	0	0	
5. Coagulation of Larger Clusters				
Fe_n + Fe => Fe_{n+1}	2.30E+13	0	0.00E+00	$9<n<200$
Fe_n + Fe_2 => Fe_{n+2}	2.30E+13	0	0.00E+00	$9<n<199$
Fe_n + Fe_3 => Fe_{n+3}	2.30E+13	0	0.00E+00	$9<n<198$

Fe_n + Fe_4 => Fe_{n+4}	2.30E+13	0	0.00E+00	9<n<197
6. Attachment of CO to Iron Cluters				
Fe_n + CO => Fe_nCO	1.00E+13	0	0	9<n<201
7. Desorption of CO from Clusters				
Fe_nCO => Fe_n + CO	1.00E+15	0	16000	9<n<201
8. Formation of SWNTs				
Fe_nCO + CO => $\beta FenC_{NT}$ + $(1+\beta)/2$ CO_2 + $(1-\beta)Fe_nCO$	1.00E+16	0	12500	9<n<201
9. End of growth of nanotubes (overcoating)				
Fe_nCNT => DFe_nC_{NT}	1.00E+00	0	0	9<n<201
10.End of Catalyst Effectiveness				
Fe_n => DFe_n	1.00E+03	0	0	9<n<201

$\beta = 1/(2n_{NT}-1)$ $n_{NT} = 3000$ in Dateo, et al.[28]

Table §.9 Reduced iron pentacarbonyl and iron cluster HiPco model of Dateo, et al. [28]

Thermal Decomposition and Formation of Small Iron Clusters from FeCO Fragment
Ames Carbonyl Rates

$Fe(CO)_5$ => $Fe(CO)_4$ + CO	4.620E+20	-1.96	21028.30
$Fe(CO)_4$ + CO => $Fe(CO)_5$	3.500E+10	0.00	0.00
$Fe(CO)_4$ => Fe(CO)3 + CO	6.960E+22	-2.14	14346.30
$Fe(CO)_3$ + CO => $Fe(CO)_4$	1.300E+13	0.00	0.00
$Fe(CO)_3$ => Fe(CO)2 + CO	8.700E+19	-1.58	14679.80
$Fe(CO)_2$ + CO => $Fe(CO)_3$	1.800E+13	0.00	0.00
$Fe(CO)_2$ => FeCO + CO	3.960E+21	-2.29	18799.40
FeCO + CO => $Fe(CO)_2$	1.500E+13	0.00	0.00
FeCO + M => Fe + M + CO	4.870E+19	-0.90	2874.50
Fe + CO + M => FeCO + M	1.00E+15	0	

2. Growth and Evaporation of Iron Clusters

Fe + Fe + M => Fe2 + M	4.00E+15	0	0
Fe_2 + Fe + M => $3\alpha Fe_C$ + M	5.00E+15	0	0
Fe2 + M => Fe + Fe + M	1.00E+15	0	16102.93
$Fe_2 + Fe_2$ => $4\alpha Fe_C$	5.00E+13	0	0
Fe_2 + Fe => Fe_5	1.00E+14	0	0
$Fe_2 + Fe_C$ => $(1+2\alpha)Fe_C$	3.00E+14	0	0

3. Attachment of CO on Iron Clusters

Fe_C + CO => Fe_CCO	1.00E+13	0	0

4. Desorption of CO from Clusters

Fe_CCO => Fe_C + CO	1.00E+15	0	16000

5. Formation of SWNTs

Fe_CCO +CO => $\beta Fe_CC_{NT} + (1+\beta)/2\ CO_2 + (1-\beta)Fe_CCO$	1.00E+16	0	12500

6. End of growth of nanotubes

$Fe_CC_{NT} + Fe_C$ => $\beta^*DFe_CC_{NT} + (1-\beta)Fe_CC_{NT}$	3.5E14	0	0

7. End of Catalyst Effectiveness

Fe_C => α^*DFe_C	1000.	0	0

$\beta = 1/(2n_{NT}-1)$, $\alpha = 1/n_C$, $\alpha^* = n_C/n_C^*$
$\beta^* = n_C/(n_C^*-n_C)$, $n_{NT} = 3000$, $n_C = 20$, $n_C^* = 40$

Table §.10a. Nickel Cluster Evaporation for n=32-2048 based on Girshick's formulas, Eqns. (§.7)-(§.13)

Reaction	A (cm^3/s/moles)	β	E/R (K)
$Ni_{32} \rightarrow Ni_{16} + 16Ni$	$9.38X10^{17}$	-0.5	39127.
$Ni_{64} \rightarrow Ni_{32} + 32Ni$	$1.34X10^{18}$	-0.5	40843.
$Ni_{128} \rightarrow Ni_{64} + 64Ni$	$1.96X10^{18}$	-0.5	42194.
$Ni_{256} \rightarrow Ni_{128} + 128Ni$	$2.91X10^{18}$	-0.5	43263.
$Ni_{512} \rightarrow Ni_{256} + 256Ni$	$4.36X10^{18}$	-0.5	44109.
$Ni_{1024} \rightarrow Ni_{512} + 512Ni$	$6.61X10^{18}$	-0.5	44780.
$Ni_{2048} \rightarrow Ni_{1024} + 1024Ni$	$1.01X10^{19}$	-0.5	45312.

Table §.10b. Nickel Cluster based on Girshick's formulas, Eqns. (§.7)-(§.13)

Reaction	A (cm^3/s/moles)	β	E/R (K)
$Ni + Ni \rightarrow Ni_2$	$3.70X10^{12}$	0.5	0
$Ni_2 + Ni \rightarrow Ni_3$	$4.10X10^{12}$	0.5	0
$Ni_3 + Ni \rightarrow Ni_4$	$4.51X10^{12}$	0.5	0
$Ni_4 + Ni \rightarrow Ni_5$	$4.90X10^{12}$	0.5	0
$Ni_5 + Ni \rightarrow Ni_6$	$5.27X10^{12}$	0.5	0
$Ni_6 + Ni \rightarrow Ni_7$	$5.61X10^{12}$	0.5	0
$Ni_7 + Ni \rightarrow Ni_8$	$5.94X10^{12}$	0.5	0
$Ni_2 + Ni_2 \rightarrow Ni_4$	$4.16X10^{12}$	0.5	0
$Ni_2 + Ni_3 \rightarrow Ni_5$	$4.37X10^{12}$	0.5	0
$Ni_2 + Ni_4 \rightarrow Ni_6$	$4.60X10^{12}$	0.5	0
$Ni_3 + Ni_3 \rightarrow Ni_6$	$4.45X10^{12}$	0.5	0
$Ni_3 + Ni_4 \rightarrow Ni_7$	$4.59X10^{12}$	0.5	0
$Ni_6 + Ni_2 \rightarrow Ni_8$	$5.06X10^{12}$	0.5	0
$Ni_5 + Ni_2 \rightarrow Ni_7$	$4.83X10^{12}$	0.5	0
$Ni_5 + Ni_3 \rightarrow Ni_8$	$4.75X10^{12}$	0.5	0
$Ni_4 + Ni_4 \rightarrow Ni_8$	$4.67X10^{12}$	0.5	0
$Ni_8 + Ni_8 \rightarrow Ni_{16}$	$4.19X10^{13}$	0.5	0
$Ni_{16} + Ni_{16} \rightarrow Ni_{32}$	$9.41X10^{13}$	0.5	0
$Ni_{32} + Ni_{32} \rightarrow Ni_{64}$	$2.11X10^{14}$	0.5	0
$Ni_{64} + Ni_{64} \rightarrow Ni_{128}$	$4.74X10^{14}$	0.5	0
$Ni_{128} + Ni_{128} \rightarrow Ni_{256}$	$1.06X10^{15}$	0.5	0
$Ni_{256} + Ni_{256} \rightarrow Ni_{512}$	$2.39X10^{15}$	0.5	0
$Ni_{512} + Ni_{512} \rightarrow Ni_{1024}$	$5.36X10^{15}$	0.5	0
$Ni_{1024} + Ni_{1024} \rightarrow Ni_{2048}$	$1.20X10^{16}$	0.5	0

Table §.11 Reactions to form nickel/carbon nuclei clusters and nanotubes.

```
! Nickel/Carbon Cluster Formation
Z    + Ni1024  => ZNiC                       1.E16   0.5    0.
C60F + Ni1024  => CFNiC                      1.E16   0.5    0.
C70F + Ni1024  => CFNiC + .1428571C70F       1.E16   0.5    0.
!
! Nanotube Formation from Z and Ni
Z + ZNiC       =>  0.08008008008CNT + ZNiC   1.E12   0.5    0.
! Nanotube Formation from C60F, C70F and Ni
C60F + ZNiC    =>  0.06006006006CNT + ZNiC   1.E13   0.5    0.
C70F + ZNiC    =>  0.07007007007CNT + ZNiC   1.E13   0.5    0.
! Soot inerting
Z              => DZ                         1.E2    0. 0.
ZNiC           => DZNiC                      1.E4    0.     0.
```

Table §.12 Reduced carbon vapor/nickel catalyst model

```
C    +  C     =  C2                2.00E+14   0        0
C    +  C2    =  C3                2.00E+14   0        0
C2   +  C2    =  C3       +  C     2.00E+15   0        9040
C3   +  C     =  0.100CC           2.E+14     0.00     0.00
C3   +  C2    =  0.125CC           2.E+14     0.00     0.00
C3   +  C3    =  0.150CC           2.E+14     0.00     0.00
!    Nin  Cluster   Agglomeration       Rao method
Ni   +    Ni  =>  Ni2              3.70479E+12    0.5  0
Ni2  +    Ni  =>  Ni3              4.09656E+12    0.5  0
Ni3  +    Ni  =>  0.0039062NiC     4.51E+12  0.5  0
Ni3  +    Ni2 =>  0.0048828NiC     4.37E+12  0.5  0
Ni3  +    Ni3 =>  0.0058593NiC     4.45E+12  0.5  0
Ni   +    NiC =>  1.0009766NiC     8.04E+13  0.5  0
Ni2  +    NiC =>  1.0019531NiC     5.96E+13  0.5  0
Ni3  +    NiC =>  1.0029297NiC     5.03E+13  0.5  0
! Rate estimated from WebElements  Ni-Ni bond energy 203 kJ/mol
Ni2  + M      => Ni + Ni + M       1.00E+15  0        24476.
! Girshick Evaporation Rates with WebElements energy
Ni3           => Ni2 + Ni          3.37E+17  -0.5     28145.
NiC           => 0.5NiC + 512Ni    6.61E+18  -0.5     44780.
! Carbon cluster agglomeration
CC     + C    =  1.025CC           2.300E+14  0.       0.
CC     + C2   => 1.05CC            2.300E+14  0.       0.
CC            => 0.95CC    + C2    3.2E13     0.       61900.
! Fullerene formation
CC     + C3   =>  0.70C60F  + C    2.00E13    0.       0.
CC     + C2   =>  0.70C60F         4.00E+09   0.      -30196.
CC     + C    =>  0.6833333C60F    2.00E13    0.       0.
! Fullerene disintegration
C60F          =>  1.45CC    +  C2  8.0E13     0.       61900.
C60F+C3       =>  0.7875Z          2.00E+13   0.       10065.
! Soot formation
CC     + CC   =>  Z                4.E13      0.       0.
Z + C3        =   1.0375Z          4.E12      0.       0.
Z + C2        =   1.025Z           4.E12      0.       0.
Z + C         =   1.0125Z          4.E12      0.       0.
! Nickel/Carbon Cluster Evaporation
ZNiC  => 0.9990234ZNiC + Ni + 0.0009766Z 6.61E+18 0. 44780.
! Soot inerting
Z             => DZ                1.0E2      0.       0.
ZNiC          => DZNiC             1.0E4      0.       0.
! Nickel/Carbon Cluster Formation
Z     + NiC   =>  ZNiC             1.E16      0.5      0.
! Nanotube Formation from Z and Ni
Z + ZNiC  =>  0.08008008008CNT + ZNiC   1.E12     .5    .0
! Nanotube Formation from C60F and Ni
C60F + ZNiC =>  0.06006006006CNT + ZNiC 1.E13     .5    .0
```

Table §.13 Comparison of the arc process with other high temperature processes used for SWNT synthesis

Process	Conditions	Energy density (W/m^2)	Vaporization Flux (g/h)	Soot containing SWCNT rate (g/h)	nanotubes (% vol.)	Temperature and cooling rates
Arc discharge [a]	$I = 100$ A; $V = 38$ V r_A=3 mm; $_{\mathrm{DAC}}$= 3mm He; $P = 660$ mbar	1.4×10^8	72	4.2	50 % vol.	$T = 6500$ K Cooling rate = 7300 K/ms
	$I = 100$ A; $V = 22$ V r_A=3 mm; $_{\mathrm{DAC}}$= 3mm Ar ; $P = 100$ mbar	7.8×10^7	8	1.5	20 % vol.	$T = 18000$ K Cooling rate = 4800 K/ms
Pulsed laser [b]	$\lambda_1 = 532$ nm $E_{pulse} = 250 - 490$ mJ $v_1 = 10 - 30$ Hz Φ_1 spot = 5 – 6 mm $t_{pulse} = 40 - 50$ ns $\lambda_2 = 1064$ nm $E_{\mathrm{pulse}} = 300 - 550$ mJ Φ_2 spot = 6 – 7 mm Ar ; $P = 500$ mbar	1.3×10^8 – 5.2×10^8	0.05	3.3×10^{-3} - 40×10^{-3}	60 - 90 % vol.	Oven at 1200°C Target at 3500 K Cooling rate = 170 – 420 K/ms
Continious laser [c]	$\lambda = 10.6$ µm $\Phi spot = 1$ mm Ar;$P = 270$–530mbar	4.3×10^8	0.1	0.13	80 % vol.	Oven at 1200°C Target at 3500 K
Solar energy [d]	λ = sun light **oven at 2 kW** power = 1300 W $\Phi spot = 15$ mm Ar ; $P = 250$ mbar	7.4×10^6	1.77×10^{-4}	0.1	-	Target at 3550 K Cooling rate = 600 K/ms
	Oven at 50 kW He ; $P = 450$ mbar Ni/Co = 2:2 % at.	8.5×10^6	15	13	-	-

a: Hinkov [116]

b: Thess *et al.*, [64]

c: Muñoz *et al.* [171]; Foutel-Richard [172]

d: Guillard *et al.* [173]; Laplaze *et al.* [174]

Table §.**14** First Ionization potential and energy of elements used in models

	Y	**Ni**	**C**	**Ar**	**He**
1st ionization potential (eV)	6.38	7.63	11.26	15.76	24.87
Ionization energy (kJ/mol)	600	737	1086	1520	2372

Table §.15 Electronic gas phase reactions considered in Hinkov [116]

number	Reaction	A (cm^{-3}.s.mol^{-1})	β	E (K)	Ref.
Ion 1	$C + e^- \leftrightarrow C^+ + e^- + e^-$	3.3×10^{20}	0	214420	82
Ion 2	$C^+ + C_3 \rightarrow C_4^+$	9.0×10^{9}	0	0	82
Ion 3	$C^+ + C_4 \rightarrow C_5^+$	6.0×10^{14}	0	0	82
Ion 4	$C^+ + e^- \leftrightarrow C$	3.6×10^{16}	- 4.5	0	83
Ion 5	$C_{60F} \leftrightarrow C_{60}^+ + e^-$	1.33×10^{15}	0	65900	84
Ion 6	$Ni^+ + e^- \leftrightarrow Ni$	2.2×10^{40}	- 4.5	0	85
Ion 7	$Y^+ + e^- \leftrightarrow Y$	2.2×10^{40}	- 4.5	0	85
Ion 8	$He^+ + e^- \leftrightarrow He$	2.2×10^{40}	- 4.5	0	85

Table §.16 Surface reactions considered in Hinkov [116]

number	Reaction	A ($cm^{-3}.s.mol^{-1}$)	β	E (K)
		Deposition		
S_1	$Ni + WL(S) \rightarrow WLNi(S)$ (Stick)	1.0	0	0
S_2	$Y + WL(S) \rightarrow WLY(S)$ (Stick)	1.0	0	0
S_3	$C + WL(S) \rightarrow WLC(S)$ (Stick)	1.0	0	0
S_4	$C_2 + WL(S) \rightarrow WLC_2(S)$ (Stick)	1.0	0	0
S_5	$C_3 + WL(S) \rightarrow WLC_3(S)$ (Stick)	1.0	0	0
S_6	$C_4 + WL(S) \rightarrow WLC_4(S)$ (Stick)	1.0	0	0
S_7	$C_5 + WL(S) \rightarrow WLC_5(S)$ (Stick)	1.0	0	0
		etching		
S_8	$C + WLC(S) \rightarrow WL(S) + C_2$ (Stick)	0.1	0	0
		recombination of ions		
S_9	$Ni^+ + e^- \rightarrow Ni$ (BOHM)	0.4	0	0
S_{10}	$Y^+ + e^- \rightarrow Y$ (BOHM)	0.4	0	0

Table §.17 Plasma characteristics calculated by AURORA assuming LTE and $T_g=T_{ion}=T_e=6500$ K

OUTLET CONDITIONS:

Specified inlet mass flow rate = 0.116 g/s
Outlet mass flow rate = 0.116 g/s
(which. based on an reactor density = 0.551×10^{-05} g/cm^3
and on a reactor volume = 0.6 cm^3
produces a **residence time**) **= 0.284×10^{-04} s**
Total ion current density = 10.4067 A/cm^2

Outlet and reactor temperature = 6500 K
Outlet and reactor pressure = 0.651 atm
Outlet and reactor density = 0.55074×10^{-05} g/cm^3
Outlet and reactor mean molecular weight = 4.5101 g/mol
Outlet molar flow rate = 0.25773×10^{-01} mol/s
Outlet volumetric flow rate = 21106 cm^3/s
(based on reactor pressure and temperature)
= 37833 SCCM
= 37.833 SLPM

Outlet and reactor electron temperature Te = 6502.7 K
Te = 0.56036 eV

OUTLET CONDITIONS FOR GAS PHASE MOLECULAR SPECIES:

Species	Mole fraction	Number density cm^{-3}	mol/s	g/s	cm^3/s
e^-	8.7×10^{-04}	$6.4\times10^{+14}$	2.2×10^{-05}	1.2×10^{-08}	$1.8\times10^{+01}$
C	4.5×10^{-02}	$3.3\times10^{+16}$	1.2×10^{-03}	1.4×10^{-02}	$9.5\times10^{+02}$
C_2	2.0×10^{-05}	$1.5\times10^{+13}$	5.2×10^{-07}	1.2×10^{-05}	4.2×10^{-01}
C_3	2.7×10^{-08}	$2.0\times10^{+10}$	7.0×10^{-10}	2.5×10^{-08}	5.8×10^{-04}
C_4	6.5×10^{-16}	$4.7\times10^{+02}$	1.7×10^{-17}	8.0×10^{-16}	1.4×10^{-11}
C_5	2.0×10^{-15}	$1.5\times10^{+03}$	5.2×10^{-17}	3.2×10^{-15}	4.3×10^{-11}
He^+	5.4×10^{-13}	$4.0\times10^{+05}$	1.4×10^{-14}	5.6×10^{-14}	1.1×10^{-08}
Ni^+	2.7×10^{-04}	$2.0\times10^{+14}$	7.1×10^{-06}	4.2×10^{-04}	$5.8\times10^{+00}$
Y^+	4.7×10^{-04}	$3.5\times10^{+14}$	1.2×10^{-05}	1.1×10^{-03}	$9.9\times10^{+00}$
C^+	1.3×10^{-04}	$9.2\times10^{+13}$	3.2×10^{-06}	3.9×10^{-05}	$2.7\times10^{+00}$
C_4^+	1.1×10^{-12}	$7.9\times10^{+05}$	2.8×10^{-14}	1.3×10^{-12}	2.3×10^{-08}
C_5^+	1.7×10^{-15}	$1.2\times10^{+03}$	4.4×10^{-17}	2.6×10^{-15}	3.6×10^{-11}
C_{60}^+	5.3×10^{-41}	3.9×10^{-23}	1.4×10^{-42}	9.9×10^{-40}	1.1×10^{-36}
Ni	1.7×10^{-03}	$1.3\times10^{+15}$	4.4×10^{-05}	2.6×10^{-03}	$3.6\times10^{+01}$
Y	4.6×10^{-06}	$3.4\times10^{+12}$	1.2×10^{-07}	1.1×10^{-05}	9.8×10^{-02}
He	9.5×10^{-01}	$7.0\times10^{+17}$	2.5×10^{-02}	9.8×10^{-02}	$2.0\times10^{+04}$

Table §.18 Plasma composition calculated for I=100 A in helium with p=660 mbar

Species	Mole fraction	Number density cm^{-3}	mol/s	g/s	cm^3/s
e^-	1.9×10^{-03}	$1.4\times10^{+15}$	4.9×10^{-05}	2.7×10^{-08}	$4.0\times10^{+01}$
C	4.5×10^{-02}	$3.3\times10^{+16}$	1.2×10^{-03}	1.4×10^{-02}	$9.5\times10^{+02}$
C_2	2.0×10^{-05}	$1.5\times10^{+13}$	5.1×10^{-07}	1.2×10^{-05}	4.2×10^{-01}
C_3	2.7×10^{-08}	$2.0\times10^{+10}$	7.0×10^{-10}	2.5×10^{-08}	5.7×10^{-04}
C_4	6.3×10^{-16}	$4.6\times10^{+02}$	1.6×10^{-17}	7.9×10^{-16}	1.3×10^{-11}
C_5	2.0×10^{-15}	$1.5\times10^{+03}$	5.1×10^{-17}	3.1×10^{-15}	4.2×10^{-11}
He^+	7.0×10^{-12}	$5.1\times10^{+06}$	1.8×10^{-13}	7.2×10^{-13}	1.5×10^{-07}
Ni^+	1.3×10^{-03}	$9.4\times10^{+14}$	3.3×10^{-05}	1.9×10^{-03}	$2.7\times10^{+01}$
Y^+	4.7×10^{-04}	$3.5\times10^{+14}$	1.2×10^{-05}	1.1×10^{-03}	$1.0\times10^{+01}$
C^+	1.3×10^{-04}	$9.2\times10^{+13}$	3.2×10^{-06}	3.9×10^{-05}	$2.7\times10^{+00}$
C_4^+	1.0×10^{-12}	$7.7\times10^{+05}$	2.7×10^{-14}	1.3×10^{-12}	2.2×10^{-08}
C_5^+	1.6×10^{-15}	$1.2\times10^{+03}$	4.2×10^{-17}	2.5×10^{-15}	3.5×10^{-11}
C_{60}^+	6.5×10^{-41}	4.8×10^{-23}	1.7×10^{-42}	1.2×10^{-39}	1.4×10^{-36}
Ni	7.2×10^{-04}	$5.2\times10^{+14}$	1.8×10^{-05}	1.1×10^{-03}	$1.5\times10^{+01}$
Y	4.2×10^{-07}	$3.1\times10^{+11}$	1.1×10^{-08}	9.6×10^{-07}	8.9×10^{-03}
He	9.5×10^{-01}	$7.0\times10^{+17}$	2.5×10^{-02}	9.8×10^{-02}	$2.0\times10^{+04}$

```
THERMO ALL
AR                IVTANOAR  1               G   300.000 20000.000 1000.00      1
 0.25199477E+01-0.22858382E-04 0.74655237E-08-0.90208251E-12 0.36063733E-16    2
-0.75393340E+03 0.42492779E+01 0.25670200E+01-0.44283132E-03 0.98495011E-06    3
-0.88424193E-09 0.27879189E-12-0.75176371E+03 0.40801018E+01                   4
C              GMcB 20K 0C    1             G   300.000 20000.000 1000.00      1
 0.23205176E+01 0.18268312E-03-0.31504542E-07 0.25371109E-11-0.62267852E-16    2
 0.84851595E+05 0.58203836E+01 0.19031864E+01 0.40200238E-02-0.90395391E-05    3
 0.81759092E-08-0.25854092E-11 0.84826660E+05 0.72917617E+01                   4
C2             GMcB 20K 0C    2             G   300.000 20000.000 1000.00      1
 0.40753780E+01 0.33239978E-03-0.12344909E-07-0.70714041E-12 0.28222317E-16    2
 0.99788114E+05 0.96847543E+00 0.54993641E+01 0.18891470E-02-0.13226503E-04    3
 0.16061423E-07-0.58286773E-11 0.99140682E+05-0.77146073E+01                   4
C3             GMcB 20K 0C    3             G   300.000 20000.000 1000.00      1
 0.49032746E+01 0.11113409E-02-0.75331984E-07-0.48099305E-12 0.89121604E-16    2
 0.96812289E+05 0.15052816E+00 0.36042014E+01 0.75373711E-02-0.11558984E-04    3
 0.88850242E-08-0.25287216E-11 0.97010617E+05 0.61103710E+01                   4
C4             GMcB 20K 0C    4             G   300.000 20000.000 1000.00      1
 0.49032746E+01 0.11113409E-02-0.75331984E-07-0.48099305E-12 0.89121604E-16    2
 0.11492855E+06 0.15052816E+00 0.36042014E+01 0.75373711E-02-0.11558984E-04    3
 0.88850242E-08-0.25287216E-11 0.11512688E+06 0.61103710E+01                   4
C5             GMcB 20K 0C    5             G   300.000 20000.000 1000.00      1
 0.11592118E+02 0.85502931E-03-0.12817463E-06 0.77473555E-11-0.16260603E-15    2
 0.11368121E+06-0.35115388E+02 0.11731935E+02-0.25681572E-01 0.78642726E-04    3
-0.78483519E-07 0.26116987E-10 0.11495211E+06-0.29295593E+02                   4
HE                120186HE  1               G  0300.00   20000.00   1000.00      1
 0.02500000E+02 0.00000000E+00 0.00000000E+00 0.00000000E+00 0.00000000E+00    2
-0.07453750E+04 0.09153489E+01 0.02500000E+02 0.00000000E+00 0.00000000E+00    3
 0.00000000E+00 0.00000000E+00-0.07453750E+04 0.09153488E+01                   4
Ni             GMcB 20K 0Ni  1              G   300.000 20000.000 1000.00      1
 0.36971152E+01-0.82867716E-03 0.18628604E-06-0.11986930E-10 0.23752778E-15    2
 0.50060051E+05 0.72075154E+00 0.42140643E+01-0.10224755E-01 0.25272825E-04    3
-0.24064628E-07 0.78454681E-11 0.50323075E+05 0.58841215E-01                   4
Y              IV 25K   0Y   1              G   300.000 25000.000 1000.00      1
 0.79437350E+00 0.13579116E-02-0.12031792E-06 0.31899976E-11-0.15582902E-16    2
 0.51410499E+05 0.18158732E+02-0.66965149E+01 0.65805915E-01-0.14851900E-03    3
 0.13342009E-06-0.41975353E-10 0.51184455E+05 0.45676826E+02                   4
```

Table §.19 Soot nuclei and soot particle reaction rates, from Krestinin and Moravskii [119].

Reaction	A($cm^3/s/moles$)	β	E
1. Formation of soot nuclei Z			
$C_{78} + C_2 \rightarrow Z$	4.0×10^{08}	0	-60.8
$C_{78} + C_2 \rightarrow Z + C$	4.0×10^{08}	0	0
n,m = 1-10			
$C_{60\text{-}m} + C_{60\text{-}n} \rightarrow Z$	4.0×10^{14}	0	0
$C_{70\text{-}m} + C_{70\text{-}n} \rightarrow Z$	4.0×10^{14}	0	0
2. Heterogeneous reactions on soot particles[a]			
C_1 + soot ↔ soot	4.0×10^{03}	0	0
C_2 + soot ↔ soot	4.0×10^{03}	0	0
C_3 + soot → soot	4.0×10^{03}	0	0
n=4-79			
C_n + soot → soot	$4.0\times10^{03}\ (1/n)^{0.5}$	0	0
C_{60F} + soot → soot	1.0×10^{03}	0	30
C_{70F} + soot → soot	1.0×10^{03}	0	30

[a] The rate constants of heterogeneous reactions are given per unit aerosol surface area.

Table §.20 Surface reactions considered in Farhat, et al. [115].

Reaction	A unit (cm-s-moles)	β	E(K)
(S1) CR+C → CR+CNT	2.50×10^{11}	0.5	0.0
(S2) CR+C3 → CR +CNT+C2	2.50×10^{11}	0.5	0.0
(S3) CR+C2 → CR +CNT+C	2.50×10^{11}	0.5	0.0

Table §.21 Calculated number densities of small carbon clusters and fullerenes at three positions in the arc. A symbol « -« indicates negligible density. Conditions are helium with p=660 mbar, I=100 amps, $\mathbf{d_{AC}}$=3 mm, and the dilution factor = 20.

	T (K)	C density (cm^{-3})	C_2 density (cm^{-3})	C_3 density (cm^{-3})	C_{60} density (cm^{-3})	C_{70} density (cm^{-3})
ANODE	4000	7.8×10^{15}	$1.1\times10^{+15}$	$1.1\times10^{+15}$	-	-
1 mm from the cathode	6472	$1.2\times10^{+16}$	$2.9\times10^{+12}$	$2.8\times10^{+09}$	-	-
CATHODE	1837	$1.7\times10^{+14}$	$8.5\times10^{+13}$	$6.0\times10^{+13}$	$2.6\times10^{+12}$	$7.0\times10^{+09}$

Table §.22 Simplified Carbon Chemistry Model used in laser ablation simulation

Reaction Rate Coefficients (where k_f=A*T^B*exp(-T_a/T))

	REACTION			A, cm^3/mole/s	B	T_a, K
1	C + e-	<=>	C+ + e- + e-	5.46E-04	0	214420
2	C + C	<=>	C_2	2.00E+14	0	0
3	C + C_2	<=>	C_3	2.00E+14	0	0
4	C_2 + C_2	<=>	C_3 + C	2.00E+15	0	9040
5	C_2 + C_2	<=>	C_4	2.00E+14	0	0
6	C + C_3	<=>	C_4	2.00E+14	0	0
7	C + C_4	<=>	C_5	2.00E+14	0	0
8	C_2 + C_3	<=>	C_5	2.00E+14	0	0
9	C+ + C_3	<=>	C_4^+	9.00E+09	0	0
10	C+ + C_4	<=>	C_5^+	6.00E+14	0	0
11	C+ + e-	<=>	C	3.60E+16	-4.5	0
12	C5 + C	<=>	C_6	2.00E+14	0	0
13	C_4 + C_2	<=>	C_6	2.00E+14	0	0
14	C_3 + C_3	<=>	C_6	2.00E+14	0	0

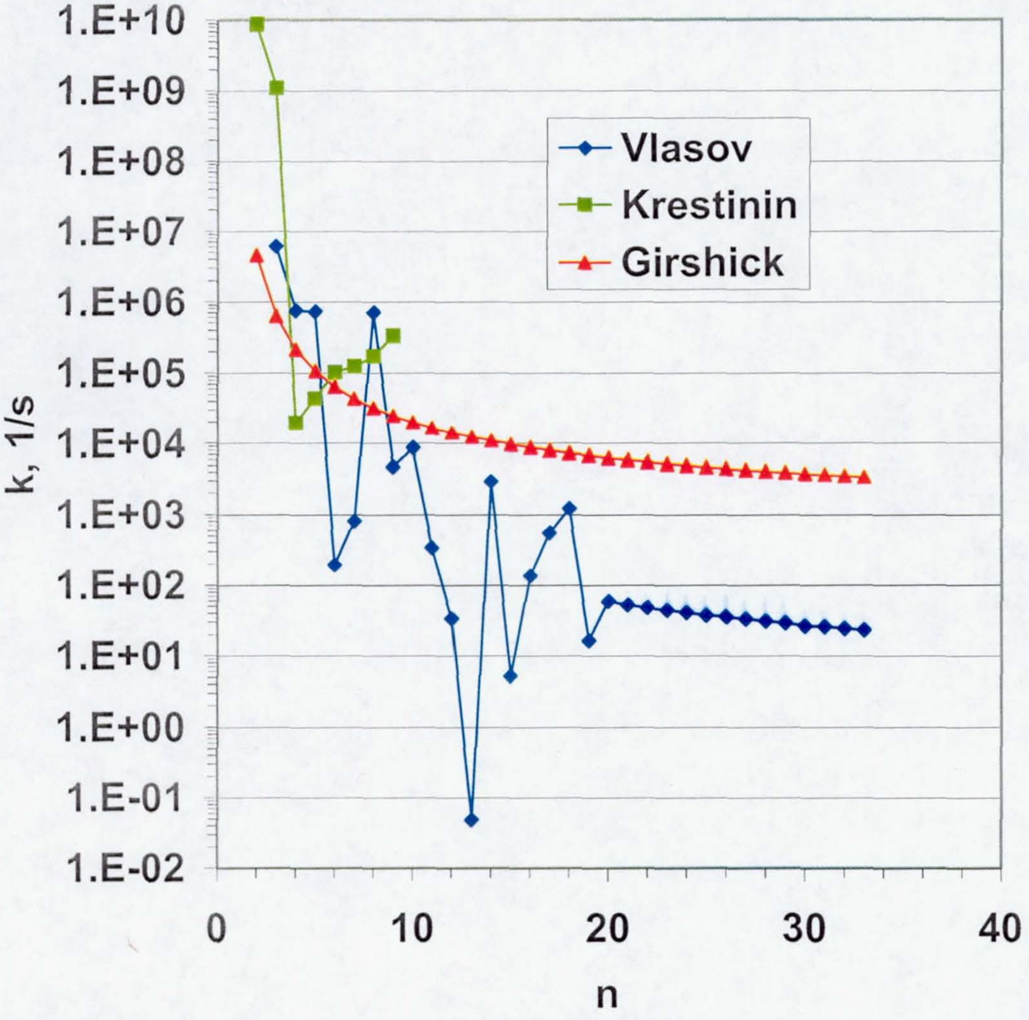

Fig. 1 Comparison of Iron Cluster Evaporation Rate Coefficients at 1380 K.

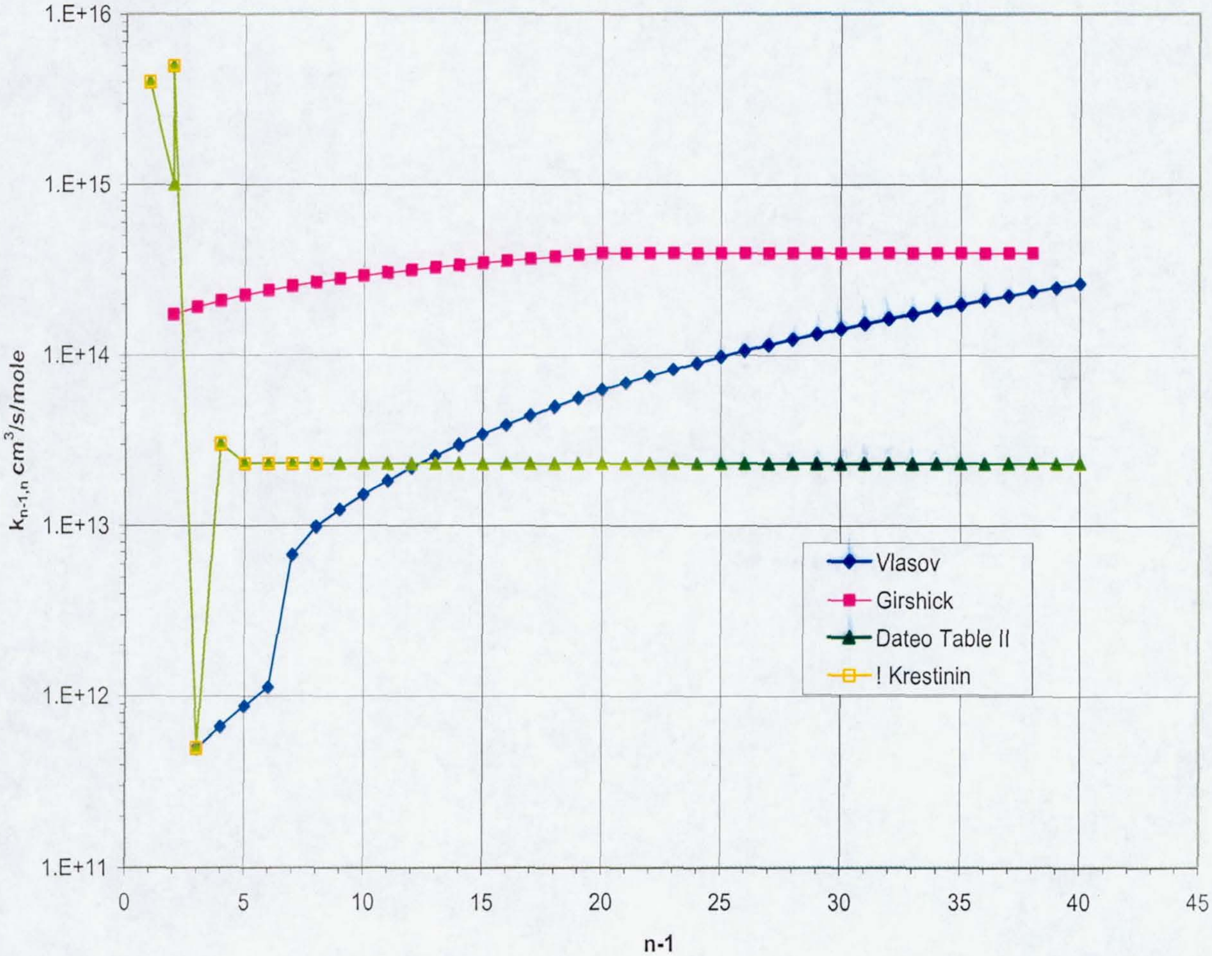

Fig. §.2 Iron cluster recombination rates at 1500 K. Iron atoms attaching to clusters of size n-1 forming clusters of n-atoms.

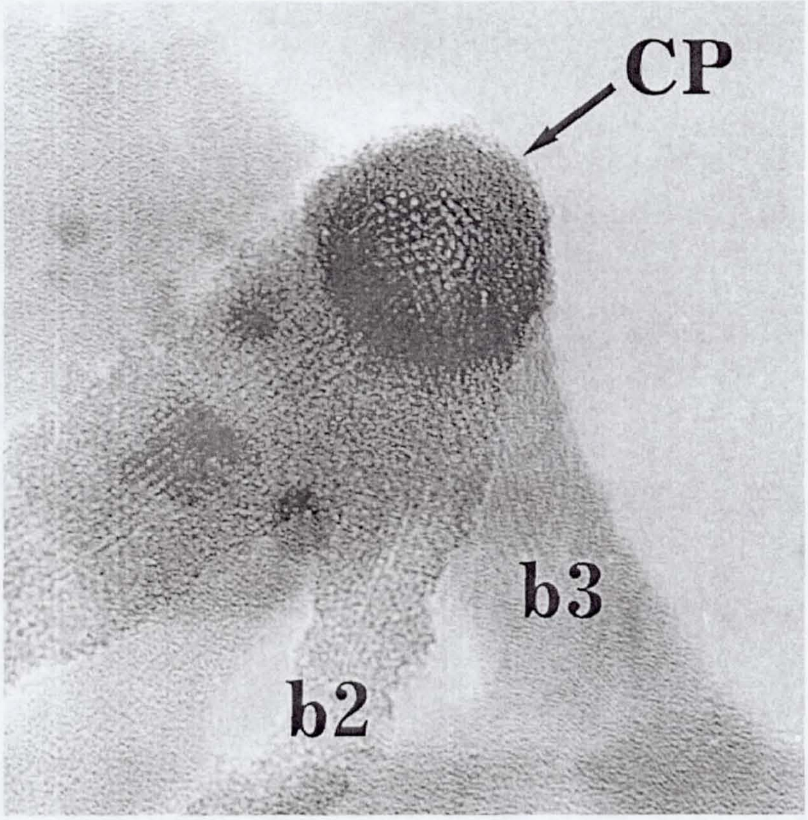

Fig. §.3 Nanotube bundles emanating from a nickel/cobalt catalyst particle. (Courtesy A. P. Moravsky)

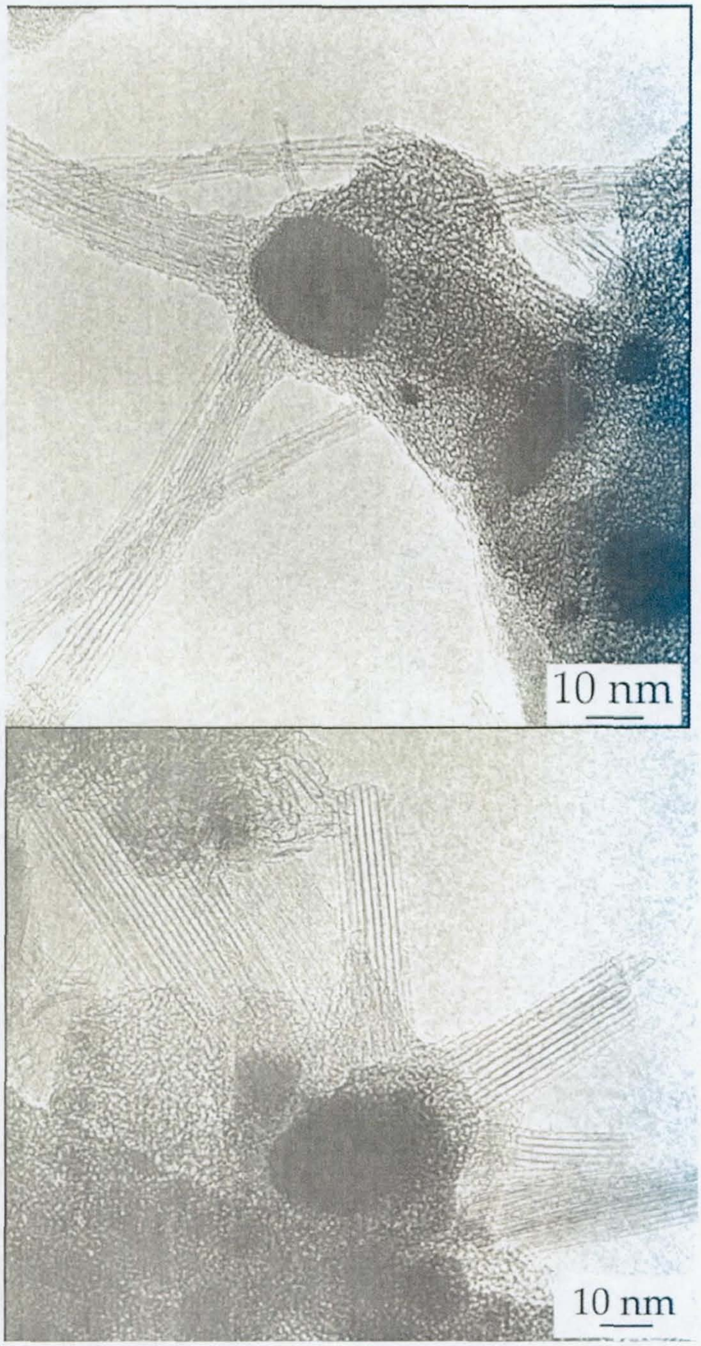

Fig. §.4 Nanotube bundles emanating from catalyst particles. (Courtesy A. Loiseau) [??]

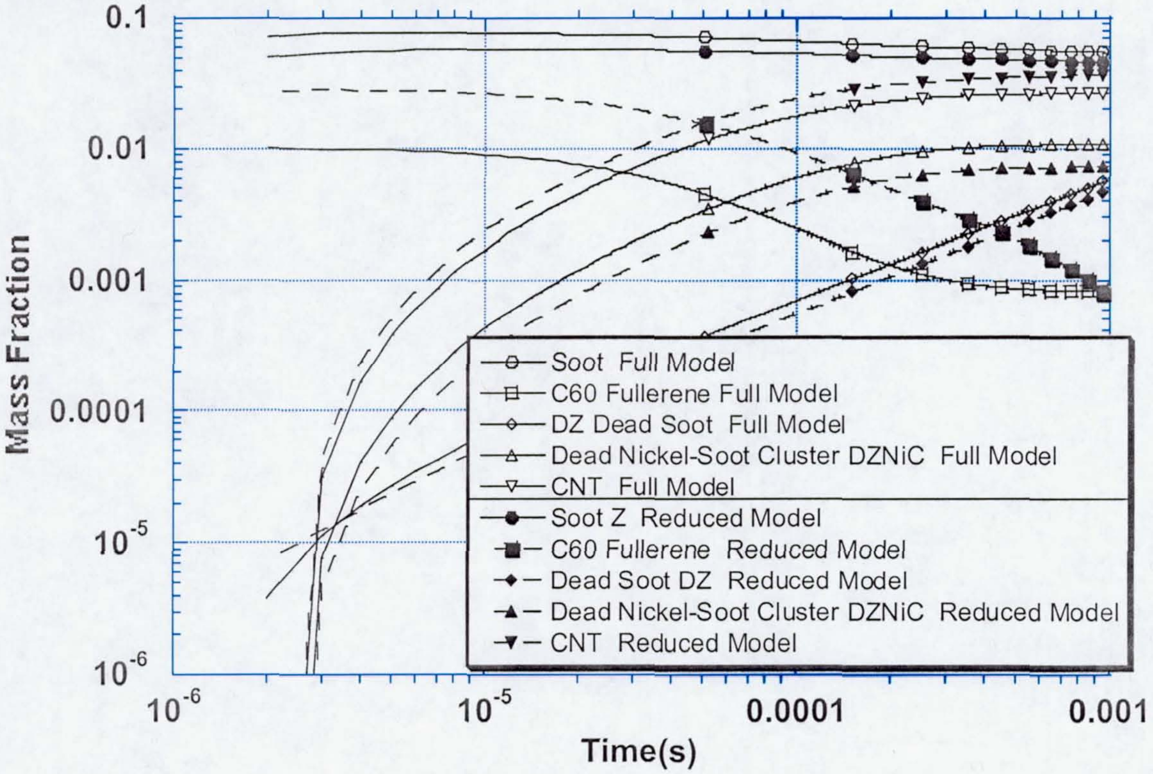

Fig. §.5 Published in JNN Vol. 4 No. 4 (2004) Fig. 3

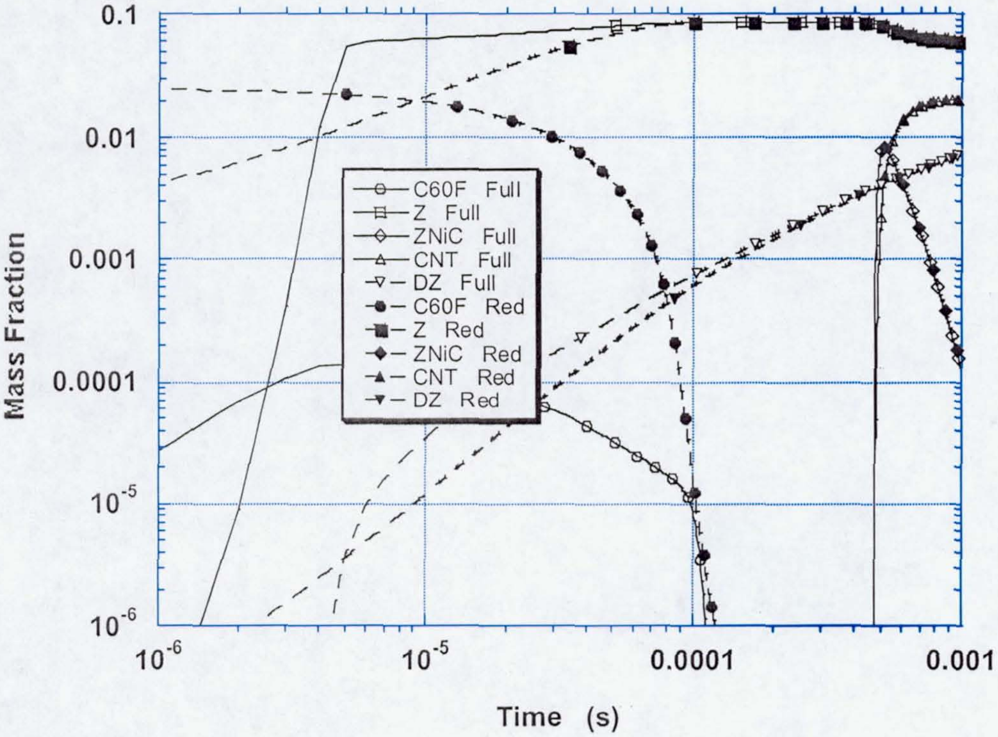
0.1
0.01
0.001
0.0001
10^{-5}
10^{-6}
Mass Fraction
10^{-6}
10^{-5}
0.0001
0.001
Time (s)
C60F Full
Z Full
ZNiC Full
CNT Full
DZ Full
C60F Red
Z Red
ZNiC Red
CNT Red
DZ Red

Fig. §.6

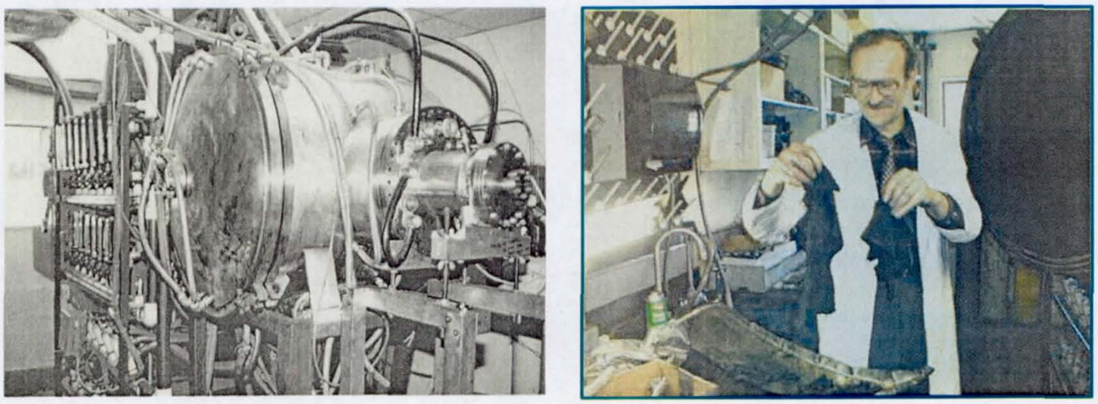

Figure §.7.

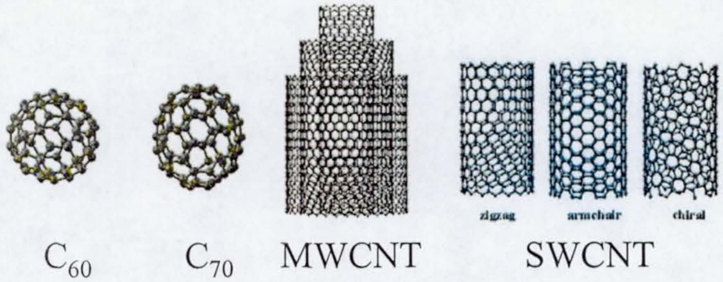

a- carbon structures

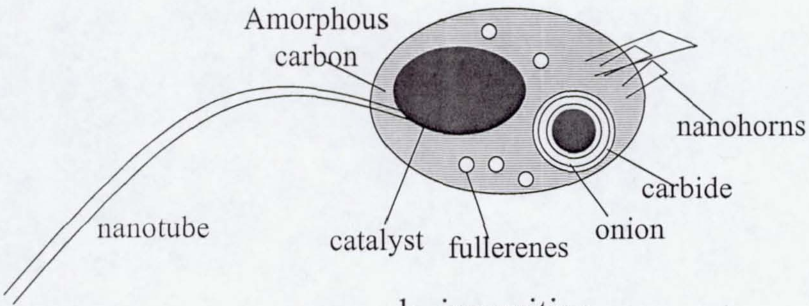

b- impurities

Figure §.8.

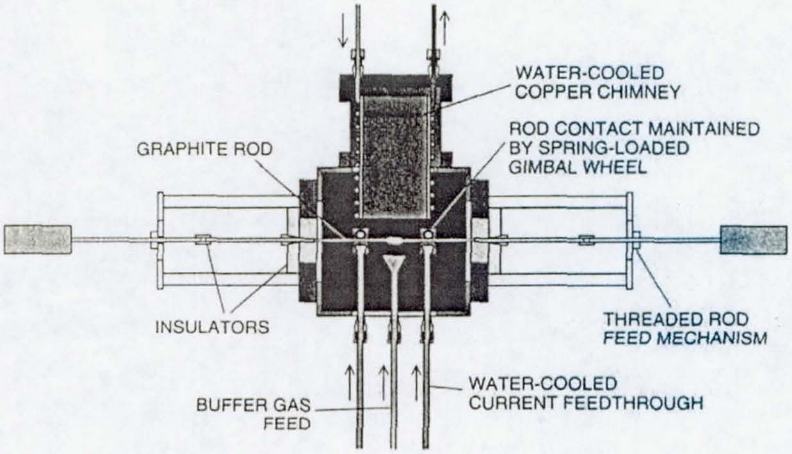
WATER-COOLED COPPER CHIMNEY
ROD CONTACT MAINTAINED BY SPRING-LOADED GIMBAL WHEEL
GRAPHITE ROD
INSULATORS
THREADED ROD FEED MECHANISM
WATER-COOLED CURRENT FEEDTHROUGH
BUFFER GAS FEED

Figure §.9.

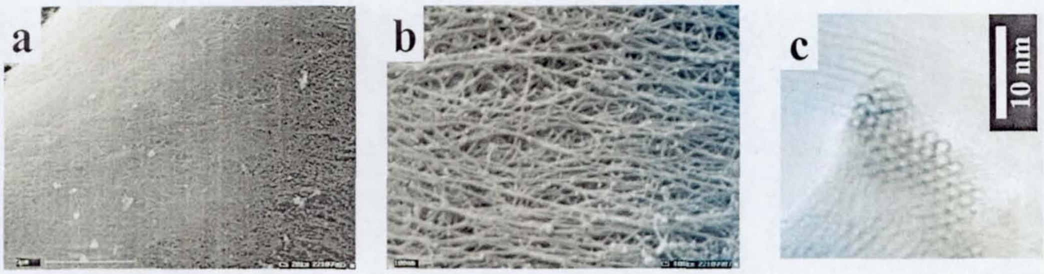

Figure §.10.

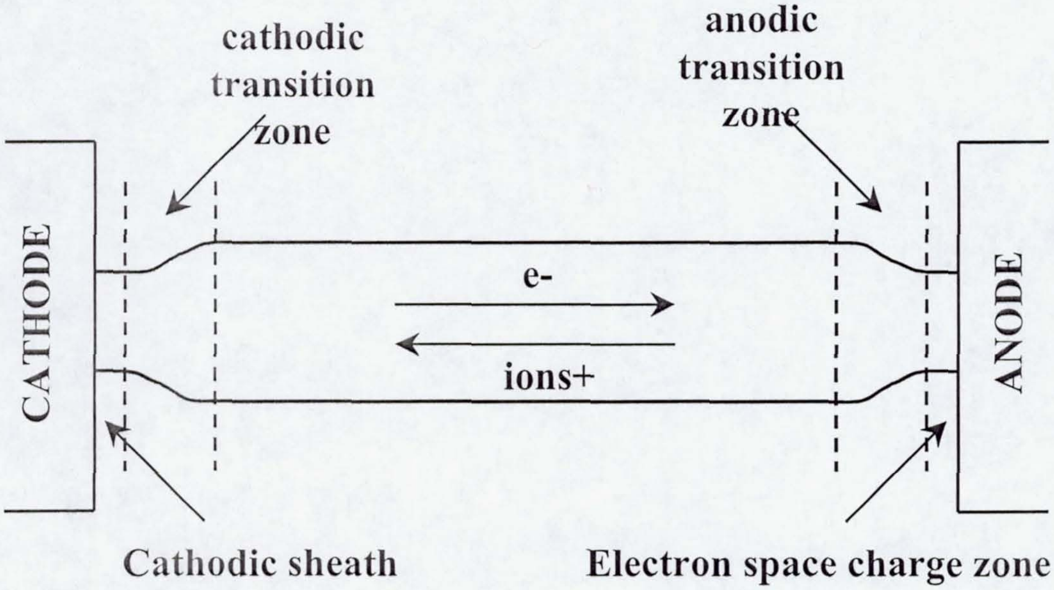
cathodic transition zone
anodic transition zone
CATHODE
ANODE
e-
ions+
Cathodic sheath
Electron space charge zone

Figure §.11.

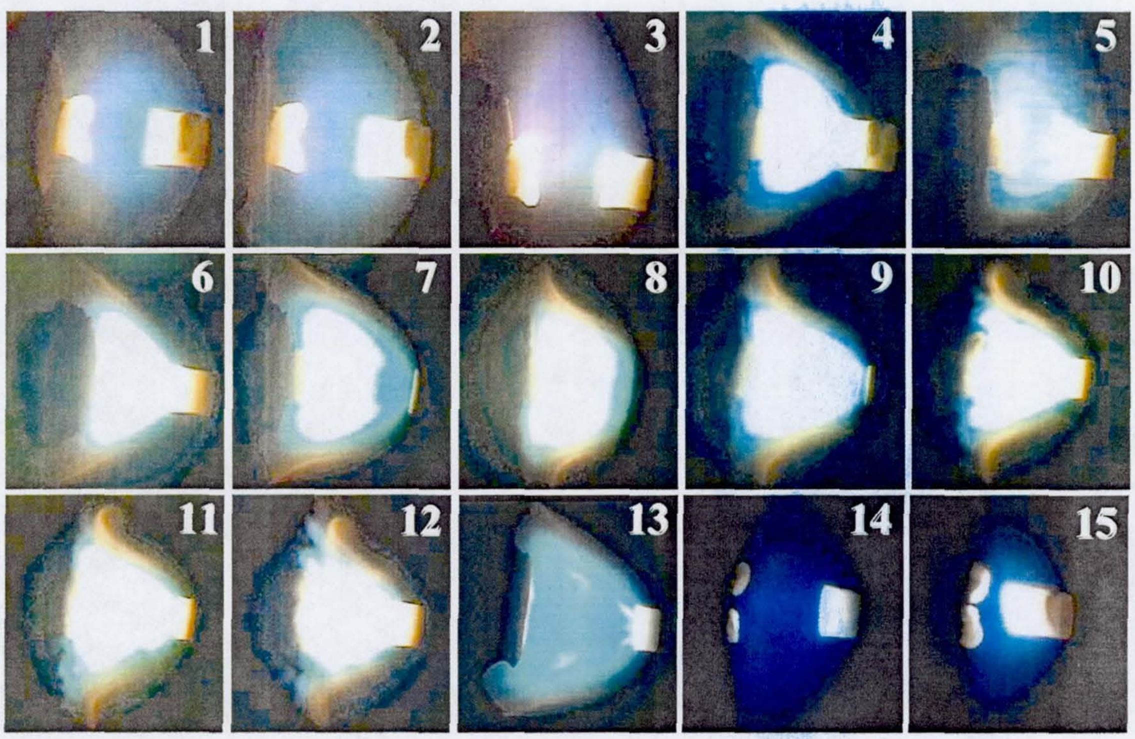

Figure §.12.

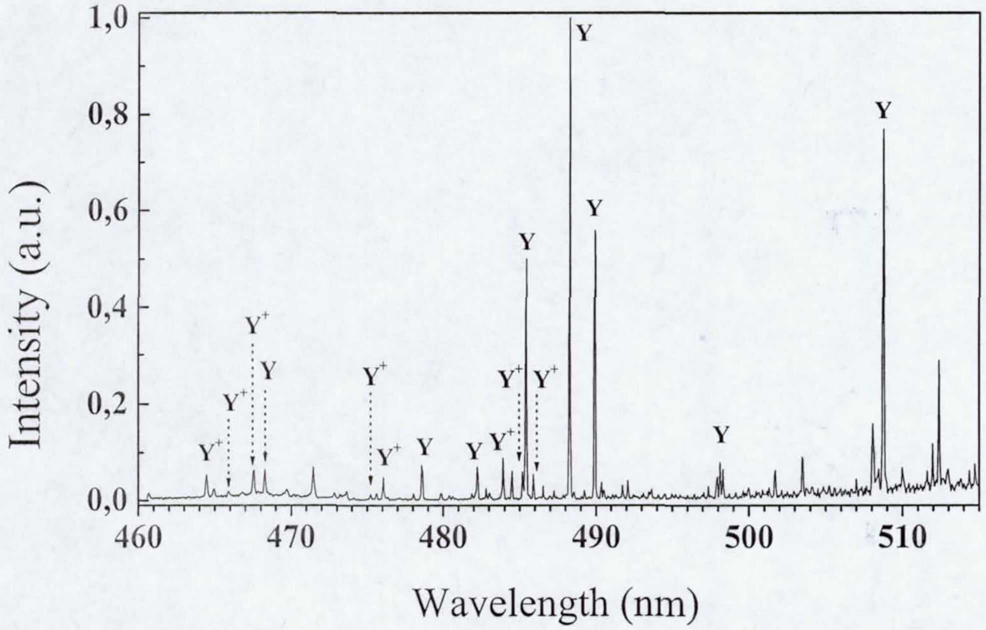
Intensity (a.u.)
Wavelength (nm)
1,0
0,8
0,6
0,4
0,2
0,0
460
470
480
490
500
510
Y
Y
Y
Y
Y⁺
Y⁺
Y
Y⁺
Y⁺
Y⁺
Y⁺
Y
Y
Y⁺
Y⁺
Y⁺
Y

Figure §.13.

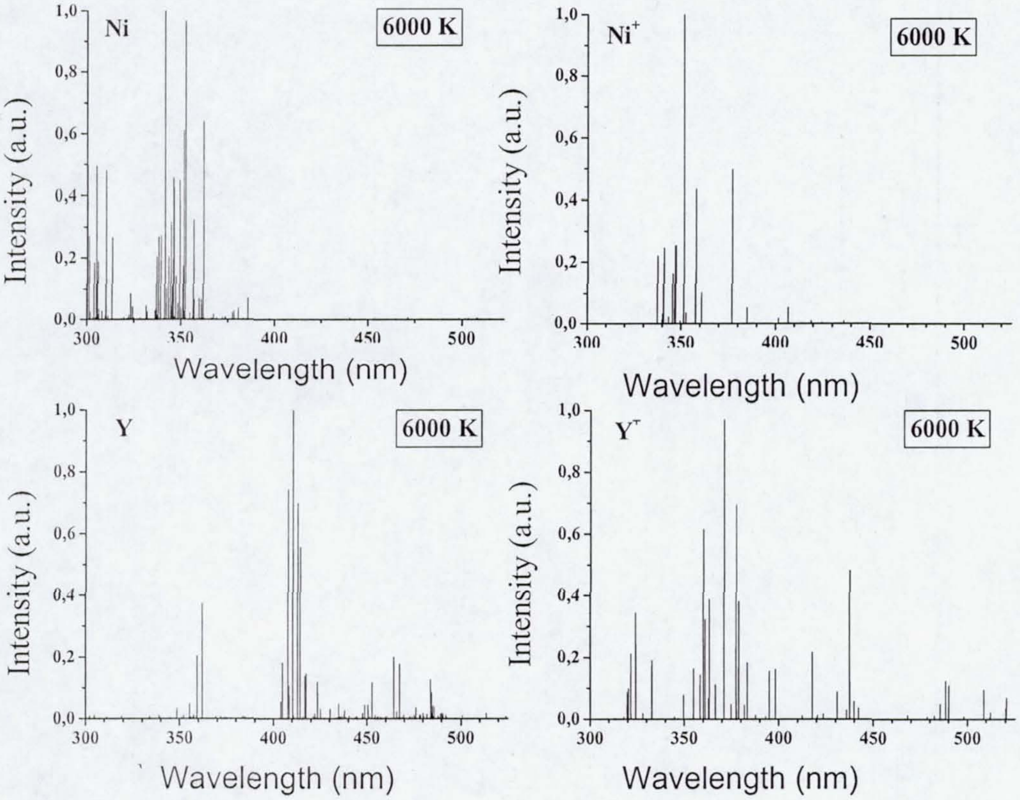
Ni
6000 K
Ni$^+$
6000 K
Y
6000 K
Y$^+$
6000 K
Intensity (a.u.)
Wavelength (nm)
0,0
0,2
0,4
0,6
0,8
1,0
300
350
400
450
500

Figure §.14.

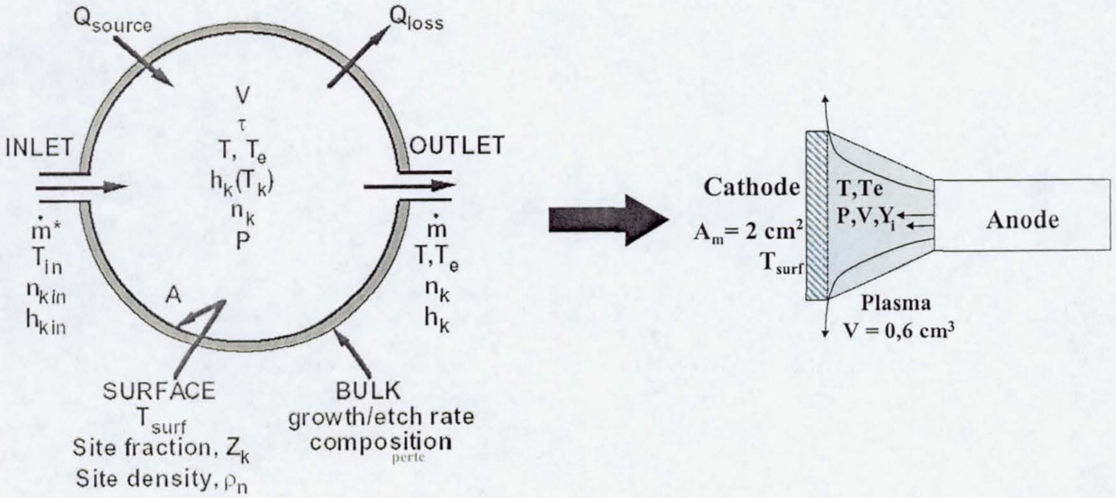

Q_{source}
Q_{loss}
V
τ
T, T_e
$h_k(T_k)$
n_k
P
INLET
OUTLET
$\dot{m}^*$
T_{in}
n_{kin}
h_{kin}
$\dot{m}$
T,T_e
n_k
h_k
A
SURFACE
T_{surf}
Site fraction, Z_k
Site density, ρ_n
BULK
growth/etch rate
composition
perte
Cathode
A_m= 2 cm^2
T_{surf}
T,Te
P,V,Y_i
Anode
Plasma
V = 0,6 cm^3

Figure §.15.

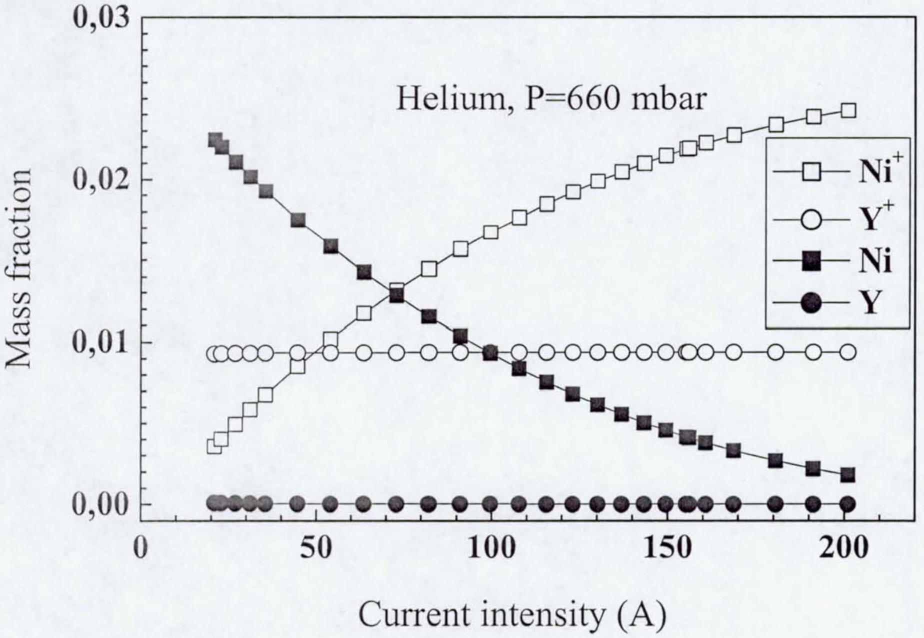
Helium, P=660 mbar
Mass fraction
0,03
0,02
0,01
0,00
0
50
100
150
200
Current intensity (A)
Ni+
Y+
Ni
Y

Figure §.16.

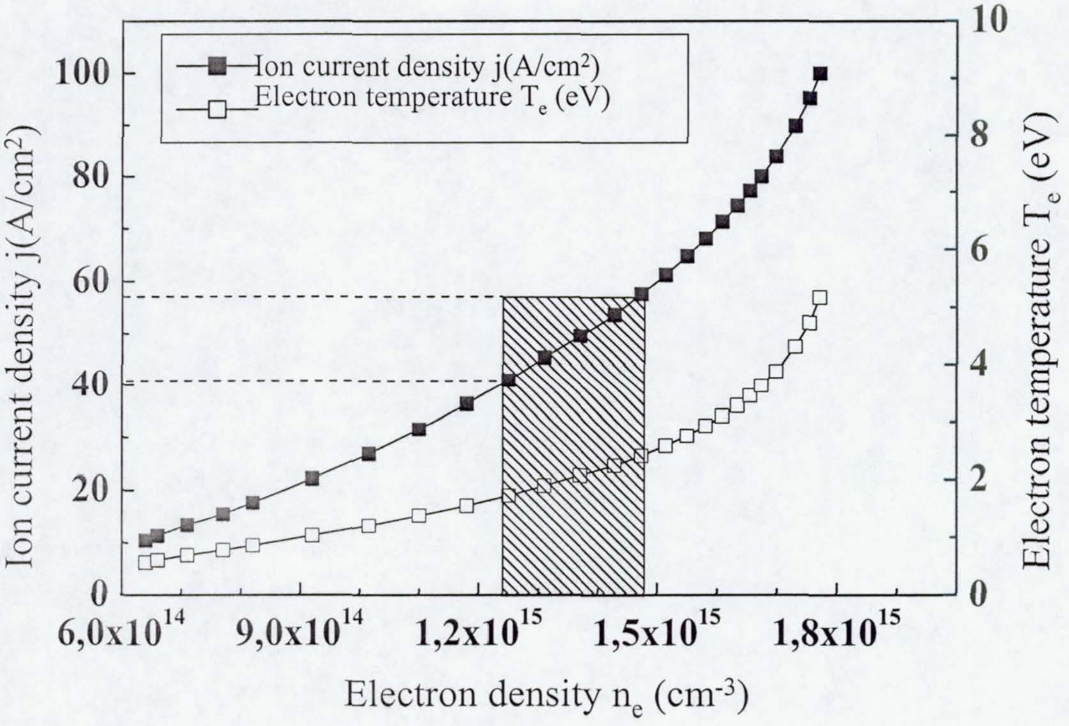

Ion current density j(A/cm²)
Electron temperature T_e (eV)
0
20
40
60
80
100
0
2
4
6
8
10
6,0x10^{14}
9,0x10^{14}
1,2x10^{15}
1,5x10^{15}
1,8x10^{15}
Electron density n_e (cm^{-3})
Ion current density j(A/cm^2)
Electron temperature T_e (eV)

Figure §.17.

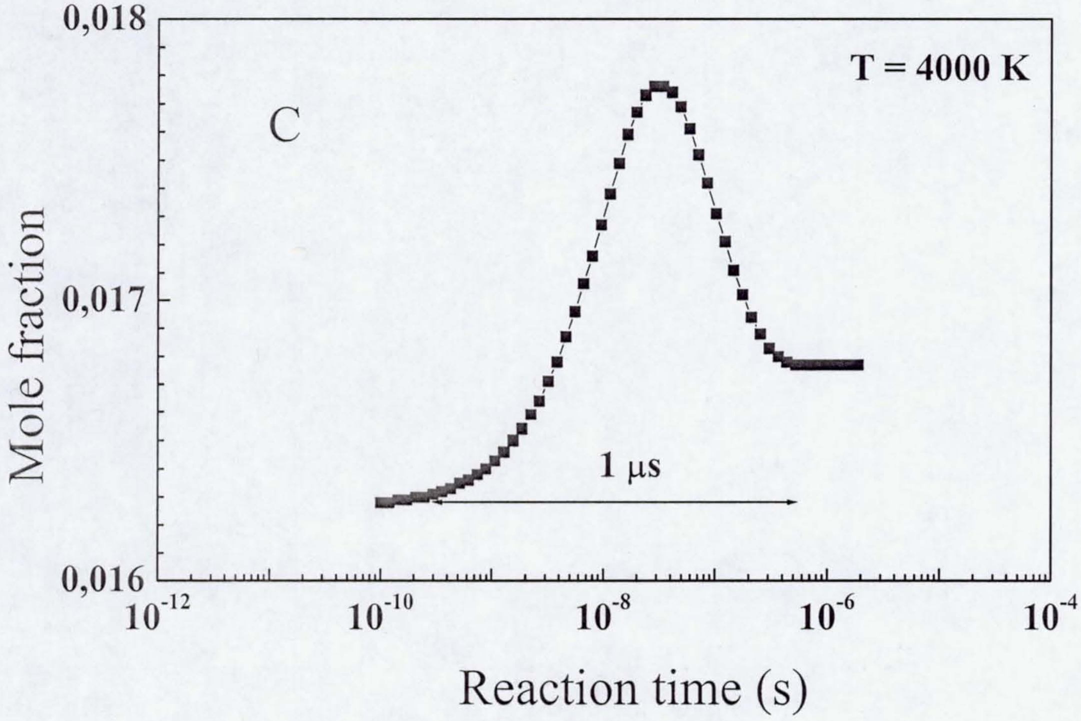
0,018
0,017
0,016
Mole fraction
C
T = 4000 K
1 μs
10^{-12}
10^{-10}
10^{-8}
10^{-6}
10^{-4}
Reaction time (s)

Figure §.18.

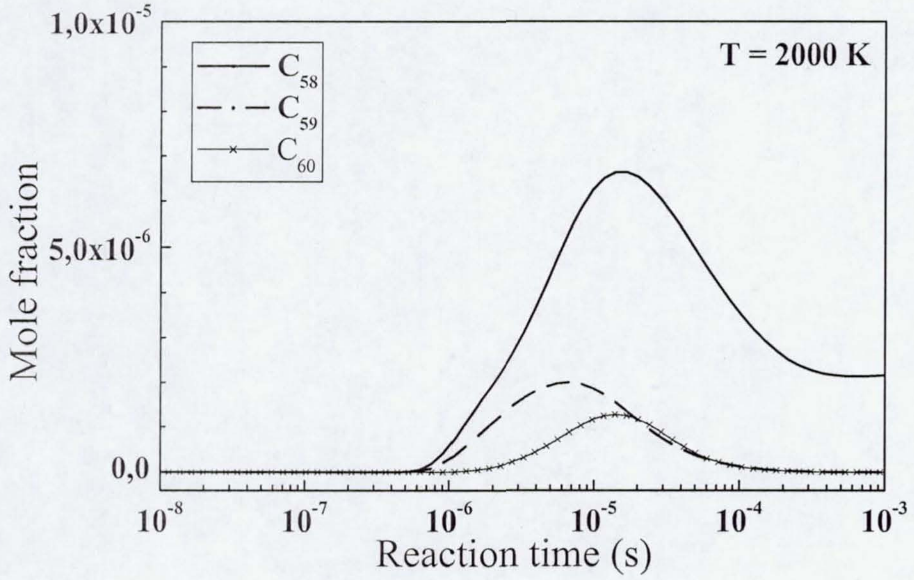

1,0x10^{-5}
5,0x10^{-6}
0,0
Mole fraction
C_{58}
C_{59}
C_{60}
T = 2000 K
10^{-8}
10^{-7}
10^{-6}
10^{-5}
10^{-4}
10^{-3}
Reaction time (s)

Figure §.19.

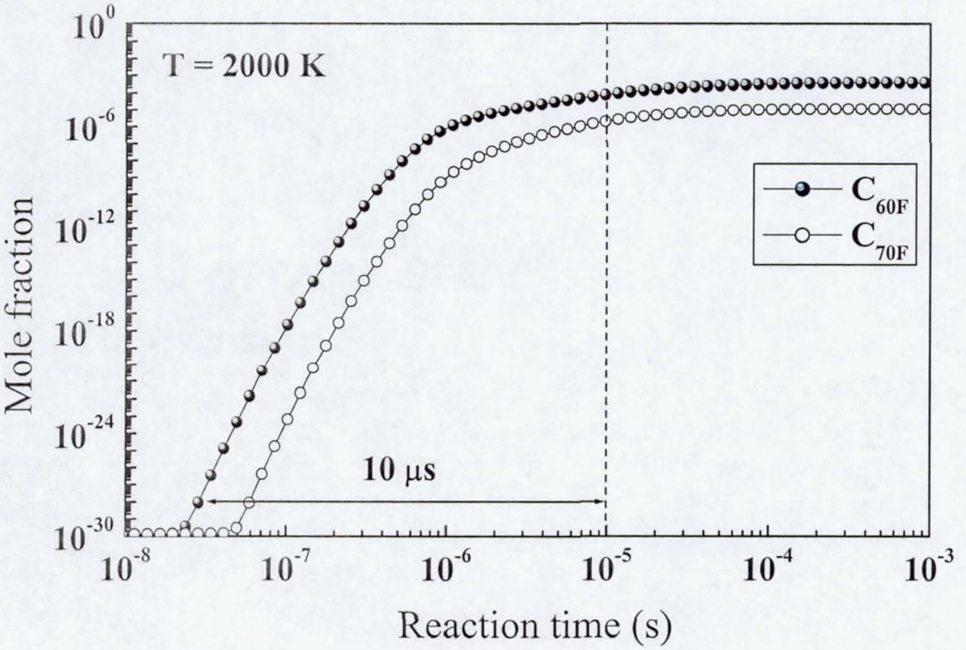
T = 2000 K
10 μs
Mole fraction
Reaction time (s)
C_{60F}
C_{70F}
10^{0}
10^{-6}
10^{-12}
10^{-18}
10^{-24}
10^{-30}
10^{-8}
10^{-7}
10^{-6}
10^{-5}
10^{-4}
10^{-3}

Figure §.20.

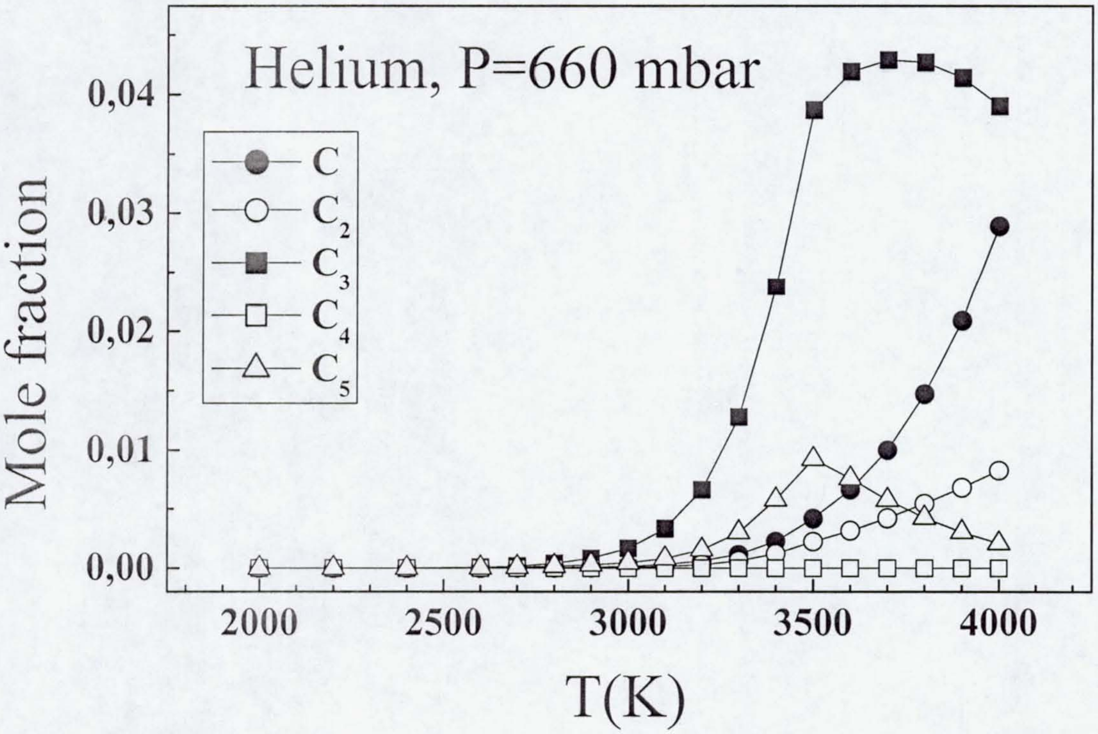

Helium, P=660 mbar
C
C_2
C_3
C_4
C_5
Mole fraction
0,00
0,01
0,02
0,03
0,04
2000
2500
3000
3500
4000
T(K)

Figure §.21-a.

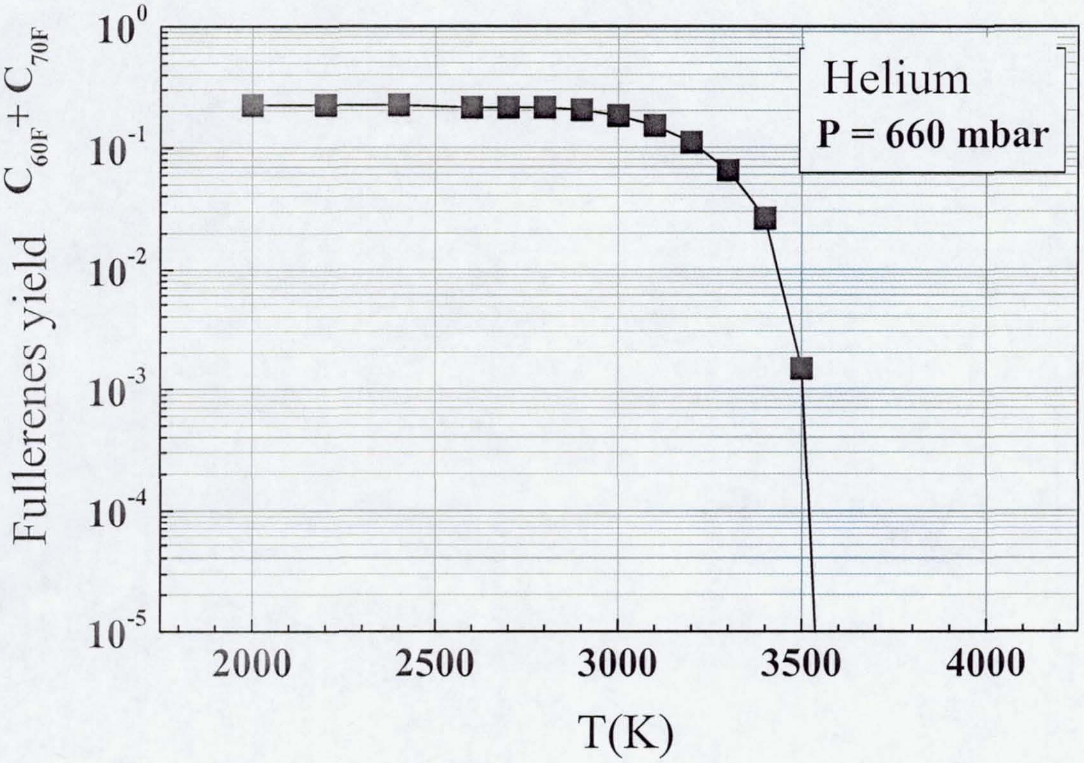
Fullerenes yield $C_{60F} + C_{70F}$
10^0
10^{-1}
10^{-2}
10^{-3}
10^{-4}
10^{-5}
2000
2500
3000
3500
4000
T(K)
Helium
P = 660 mbar

Figure §.21-b.

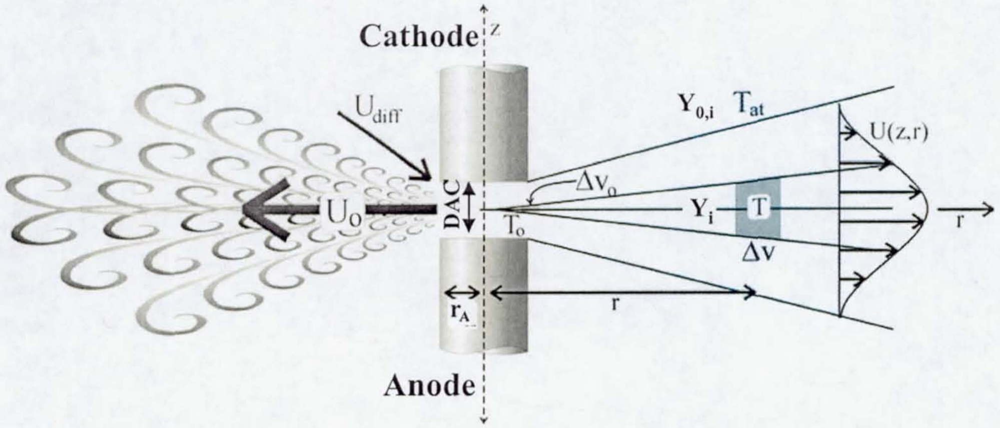
Cathode
z
U_{diff}
$Y_{0,i}$
T_{at}
$U(z,r)$
Δv_o
U_O
DAC
T_o
Y_i
T
r
Δv
r_A
r
Anode

Figure §.22.

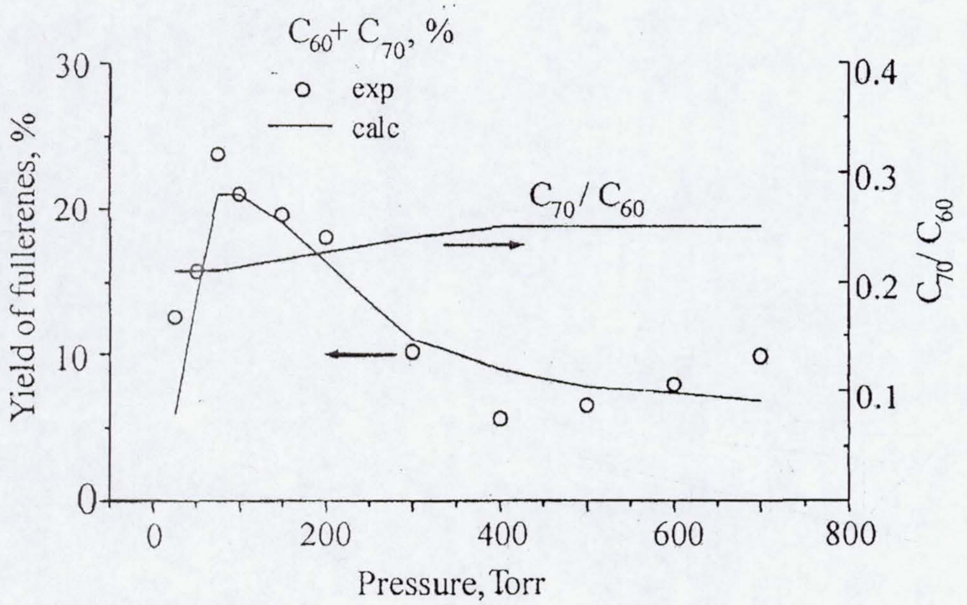
$C_{60}+C_{70}$, %
exp
calc
C_{70}/C_{60}
Yield of fullerenes, %
30
20
10
0
0.4
0.3
0.2
0.1
C_{70}/C_{60}
0
200
400
600
800
Pressure, Torr

Figure §.23.

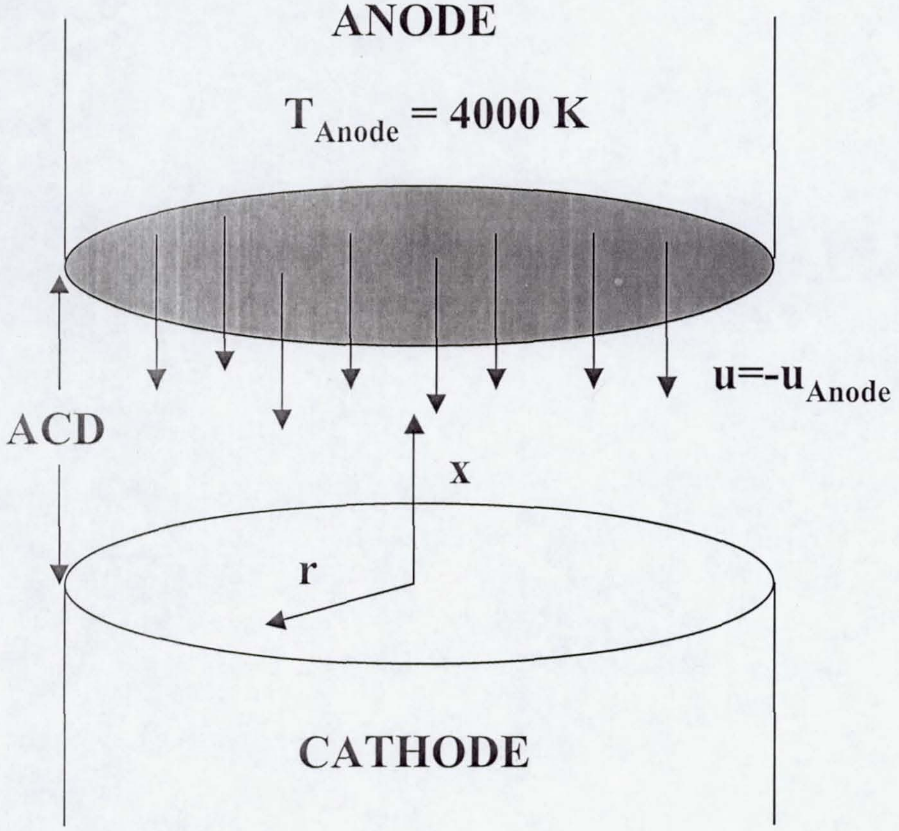

Figure §.24.

Figure §.25.

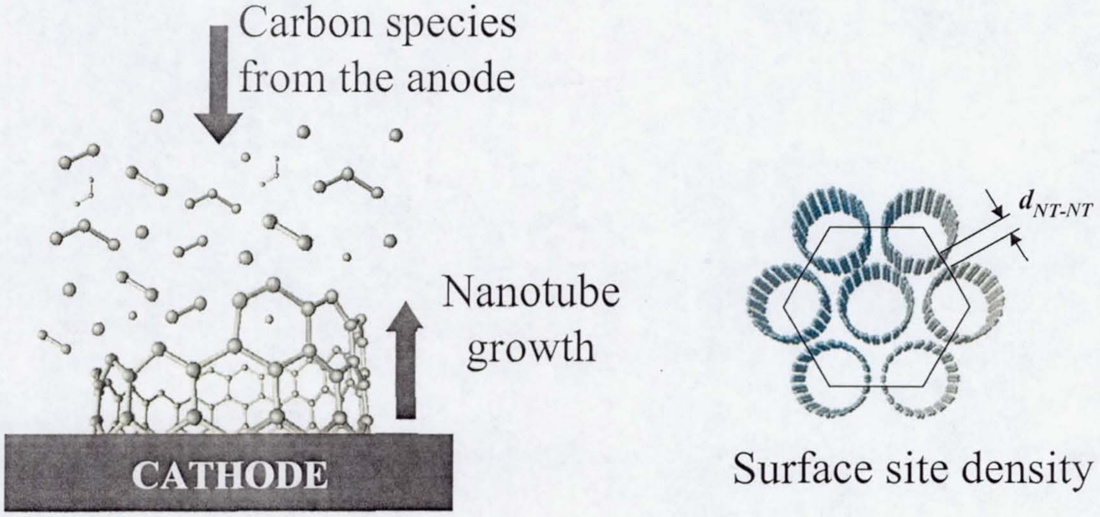
Carbon species
from the anode
Nanotube
growth
CATHODE
$d_{NT\text{-}NT}$
Surface site density

Figure §.26.

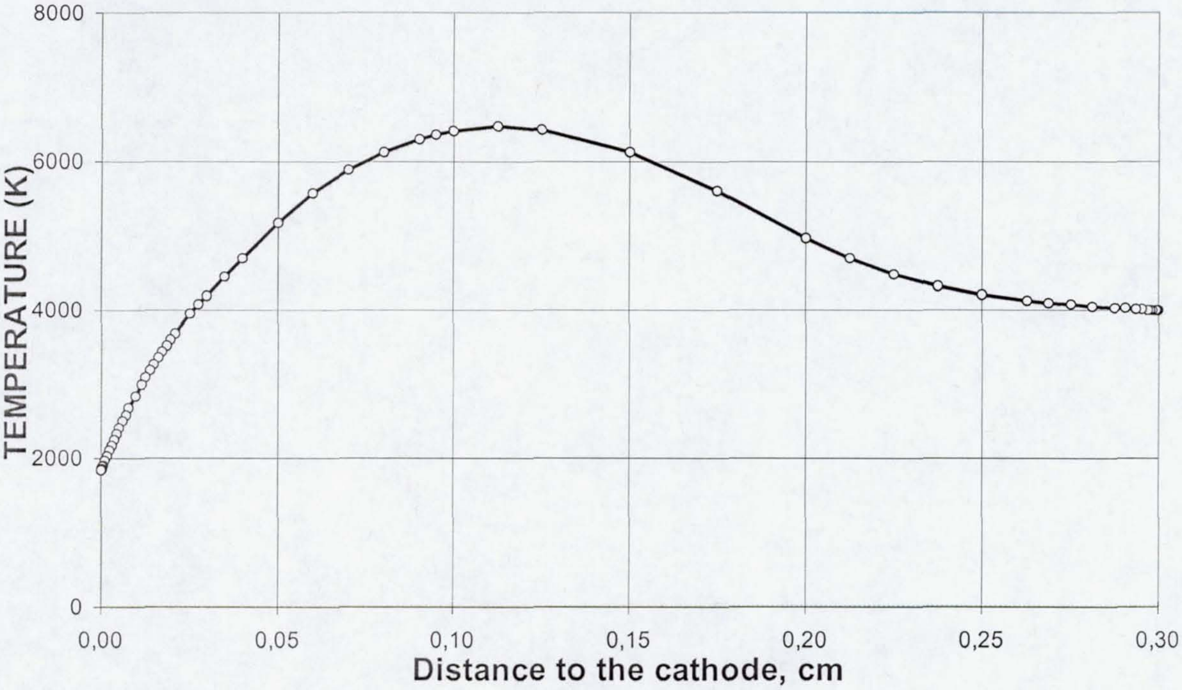
8000
6000
4000
2000
0
TEMPERATURE (K)
0,00
0,05
0,10
0,15
0,20
0,25
0,30
Distance to the cathode, cm

Figure §.27.

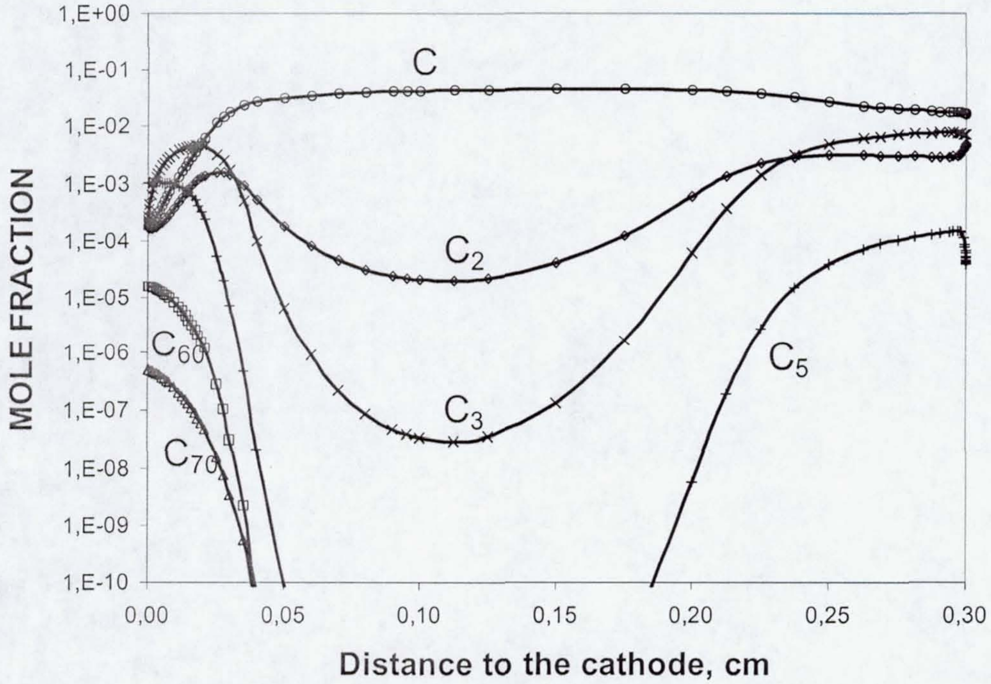
1,E+00
1,E-01
1,E-02
1,E-03
1,E-04
1,E-05
1,E-06
1,E-07
1,E-08
1,E-09
1,E-10
MOLE FRACTION
0,00
0,05
0,10
0,15
0,20
0,25
0,30
Distance to the cathode, cm
C
C_2
C_3
C_5
C_{60}
C_{70}

Figure §.28.

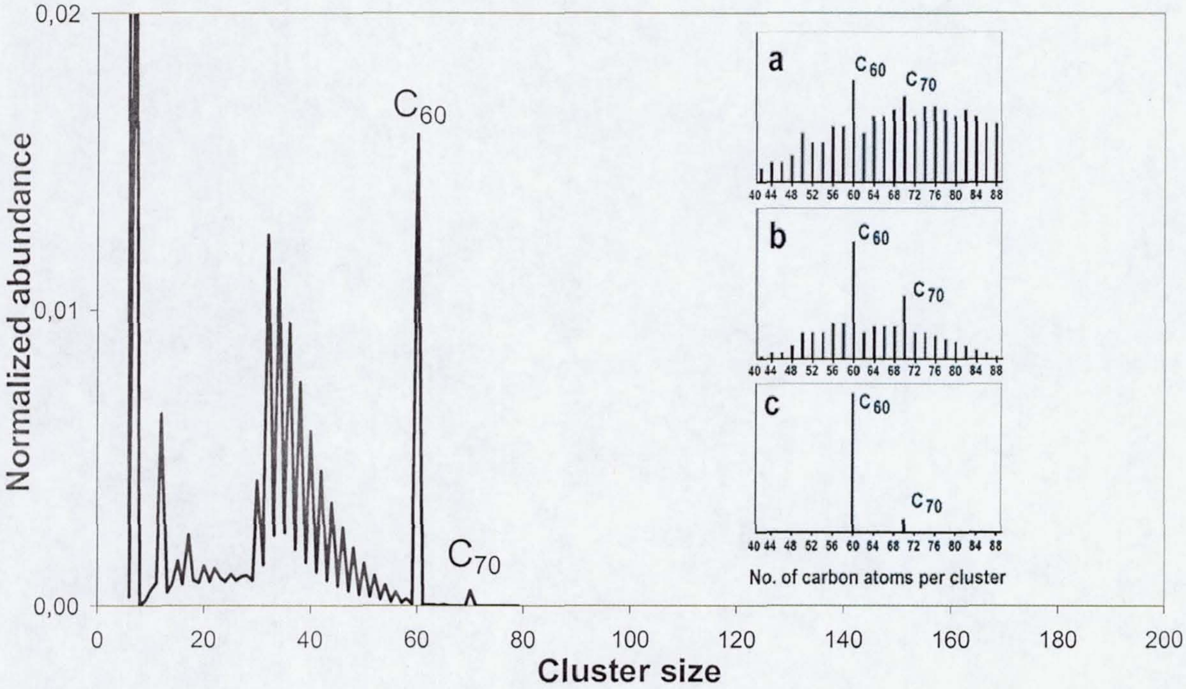
0,02
0,01
0,00
Normalized abundance
C_{60}
C_{70}
0
20
40
60
80
100
120
140
160
180
200
Cluster size
a
C_{60}
C_{70}
b
C_{60}
C_{70}
c
C_{60}
C_{70}
40 44 48 52 56 60 64 68 72 76 80 84 88
No. of carbon atoms per cluster

Figure §.29.

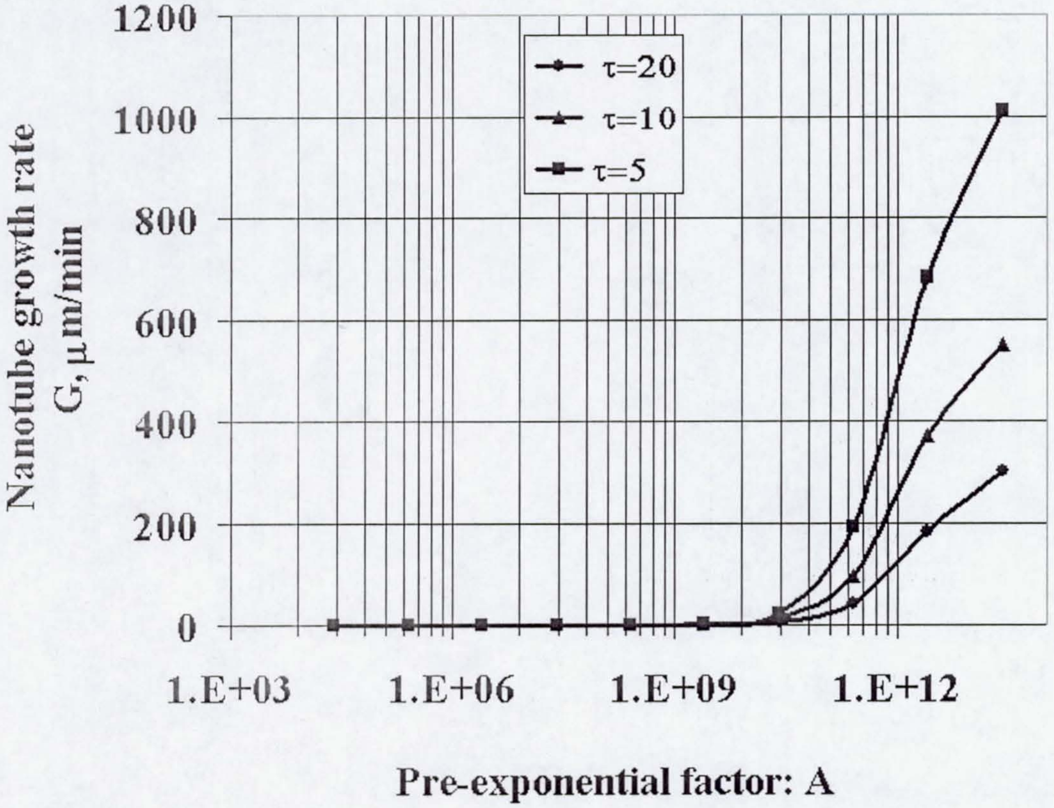

1200
1000
800
600
400
200
0
Nanotube growth rate
G, μm/min
τ=20
τ=10
τ=5
1.E+03
1.E+06
1.E+09
1.E+12
Pre-exponential factor: A

Figure §.30.

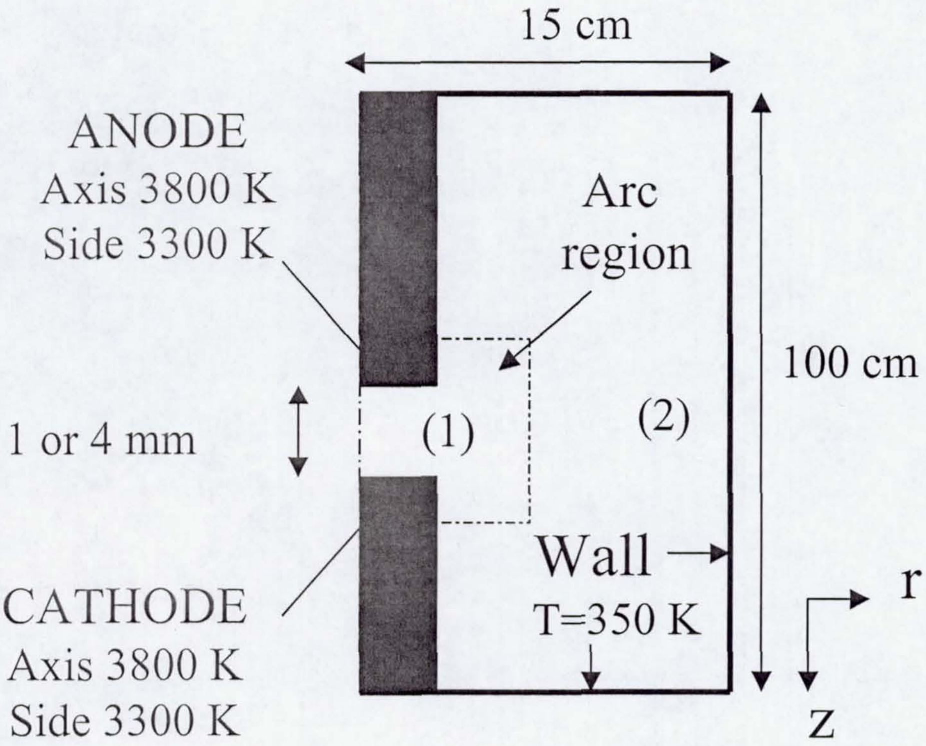
15 cm
ANODE
Axis 3800 K
Side 3300 K
Arc
region
100 cm
1 or 4 mm
(1)
(2)
Wall
CATHODE
T=350 K
r
Axis 3800 K
Side 3300 K
z

Figure §.31.

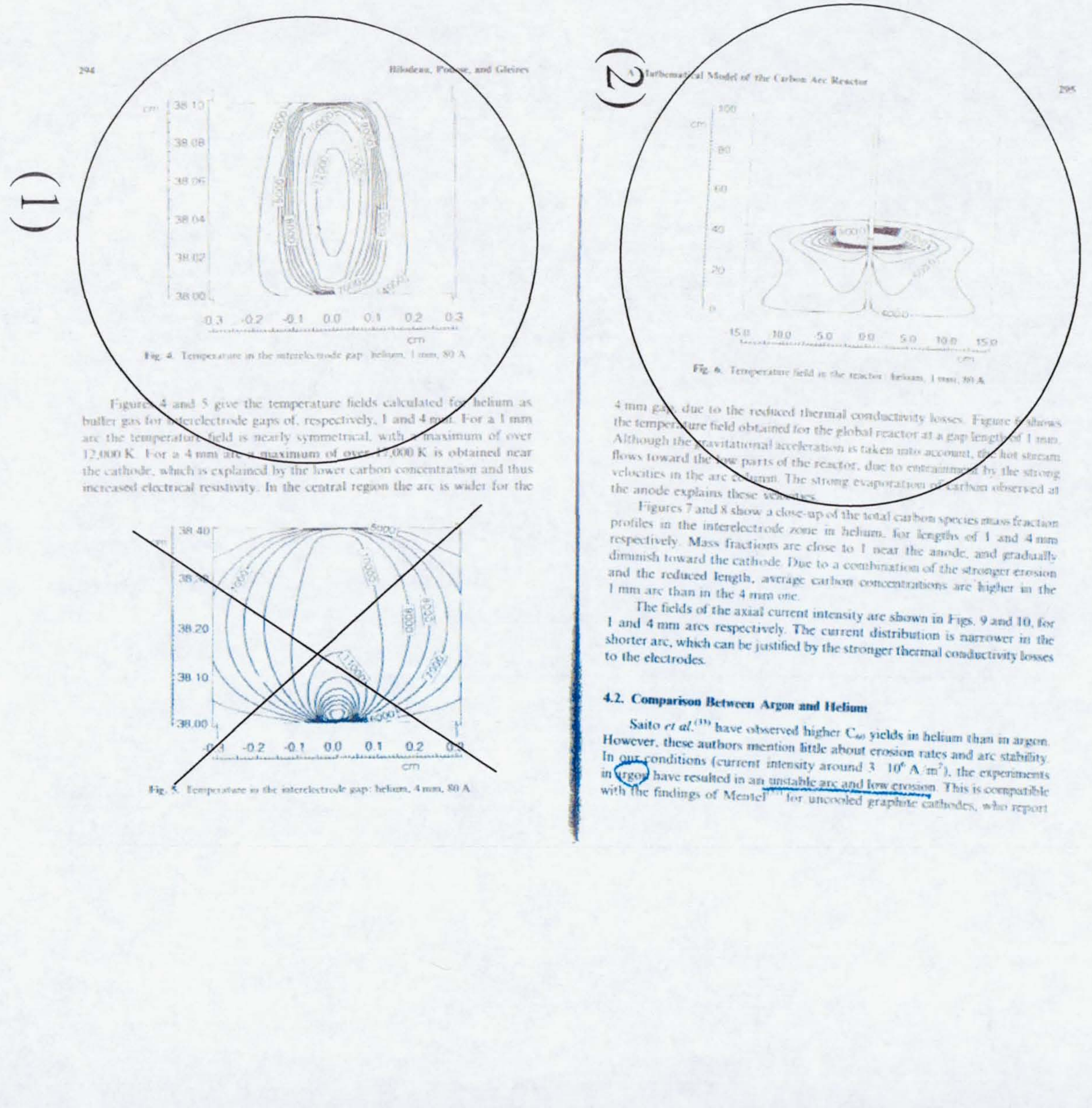

294 Bilodeau, Pousse, and Gleizes

Fig. 4. Temperature in the interelectrode gap: helium, 1 mm, 80 A

Figures 4 and 5 give the temperature fields calculated for helium as buffer gas for interelectrode gaps of, respectively, 1 and 4 mm. For a 1 mm arc the temperature field is nearly symmetrical, with a maximum of over 12,000 K. For a 4 mm arc a maximum of over 13,000 K is obtained near the cathode, which is explained by the lower carbon concentration and thus increased electrical resistivity. In the central region the arc is wider for the

Fig. 5. Temperature in the interelectrode gap: helium, 4 mm, 80 A

Mathematical Model of the Carbon Arc Reactor 295

Fig. 6. Temperature field in the reactor: helium, 1 mm, 80 A

4 mm gap, due to the reduced thermal conductivity losses. Figure 6 shows the temperature field obtained for the global reactor at a gap length of 1 mm. Although the gravitational acceleration is taken into account, the hot stream flows toward the low parts of the reactor, due to entrainment by the strong velocities in the arc column. The strong evaporation of carbon observed at the anode explains these velocities.

Figures 7 and 8 show a close-up of the total carbon species mass fraction profiles in the interelectrode zone in helium, for lengths of 1 and 4 mm respectively. Mass fractions are close to 1 near the anode, and gradually diminish toward the cathode. Due to a combination of the stronger erosion and the reduced length, average carbon concentrations are higher in the 1 mm arc than in the 4 mm one.

The fields of the axial current intensity are shown in Figs. 9 and 10, for 1 and 4 mm arcs respectively. The current distribution is narrower in the shorter arc, which can be justified by the stronger thermal conductivity losses to the electrodes.

4.2. Comparison Between Argon and Helium

Saito *et al.*(11) have observed higher C_{60} yields in helium than in argon. However, these authors mention little about erosion rates and arc stability. In our conditions (current intensity around 3×10^6 A/m^2), the experiments in argon have resulted in an unstable arc and low erosion. This is compatible with the findings of Mentel for uncooled graphite cathodes, who report

Figure §.32. (to be improved)

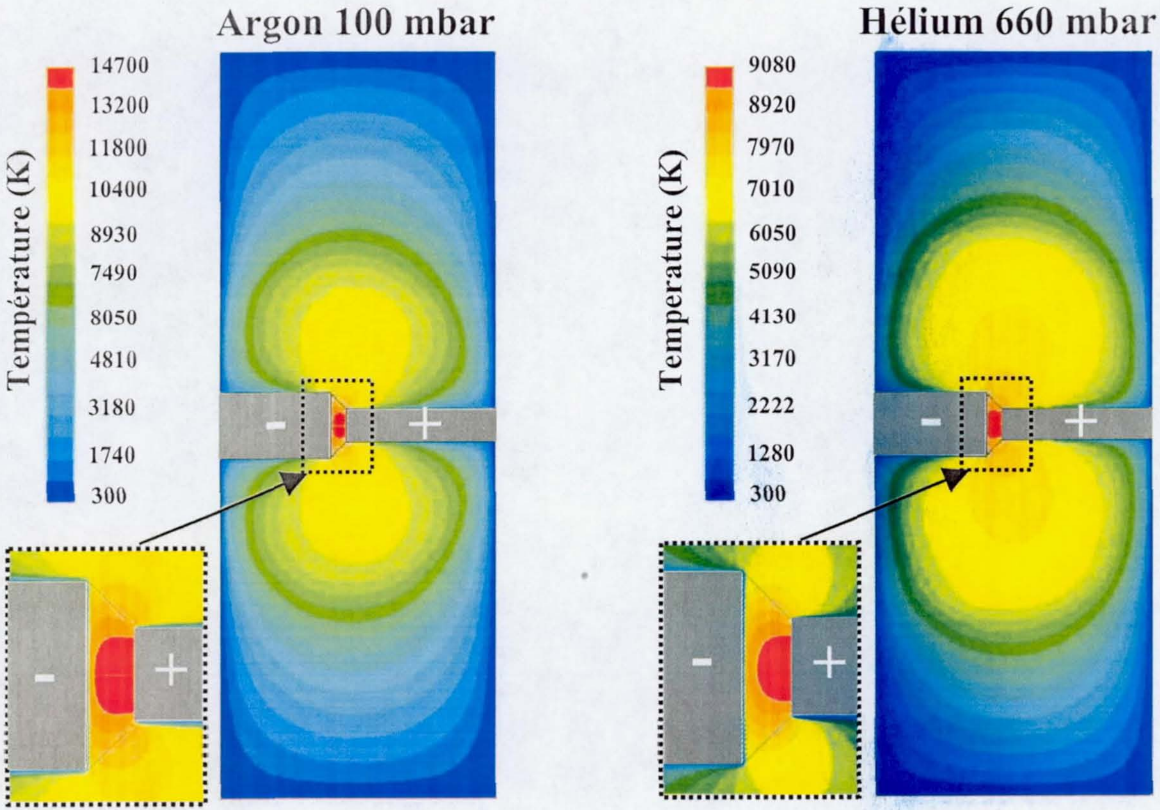
Argon 100 mbar

Hélium 660 mbar

Figure §.33.

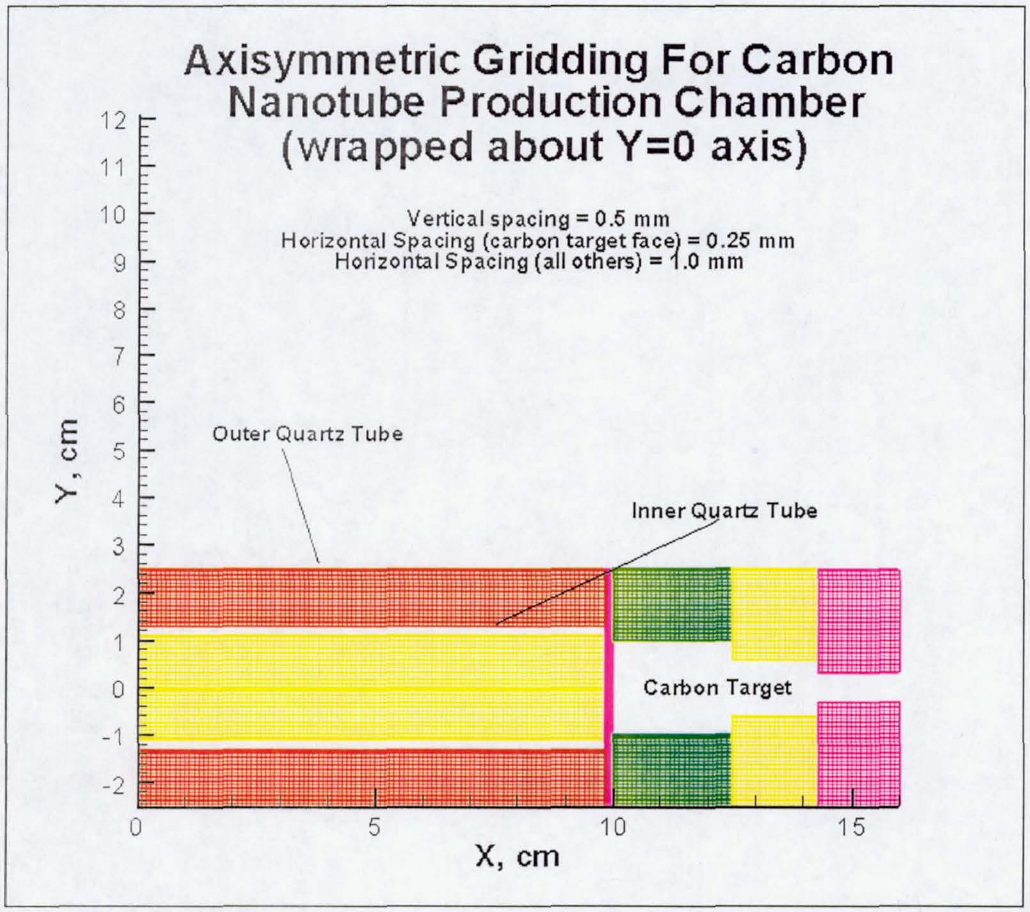
Axisymmetric Gridding For Carbon Nanotube Production Chamber (wrapped about Y=0 axis)
Vertical spacing = 0.5 mm
Horizontal Spacing (carbon target face) = 0.25 mm
Horizontal Spacing (all others) = 1.0 mm
Outer Quartz Tube
Inner Quartz Tube
Carbon Target
Y, cm
X, cm
12
11
10
9
8
7
6
5
4
3
2
1
0
-1
-2
0
5
10
15

Figure §.34

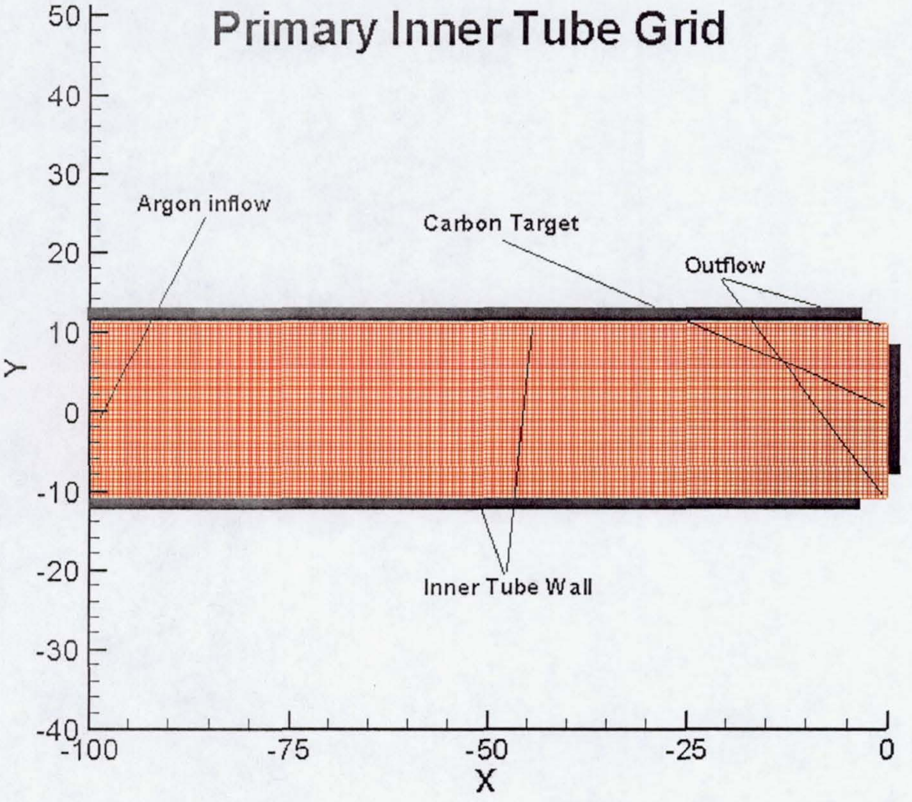
Primary Inner Tube Grid
Argon inflow
Carbon Target
Outflow
Inner Tube Wall
Y
X
50
40
30
20
10
0
-10
-20
-30
-40
-100
-75
-50
-25
0

Figure §.35

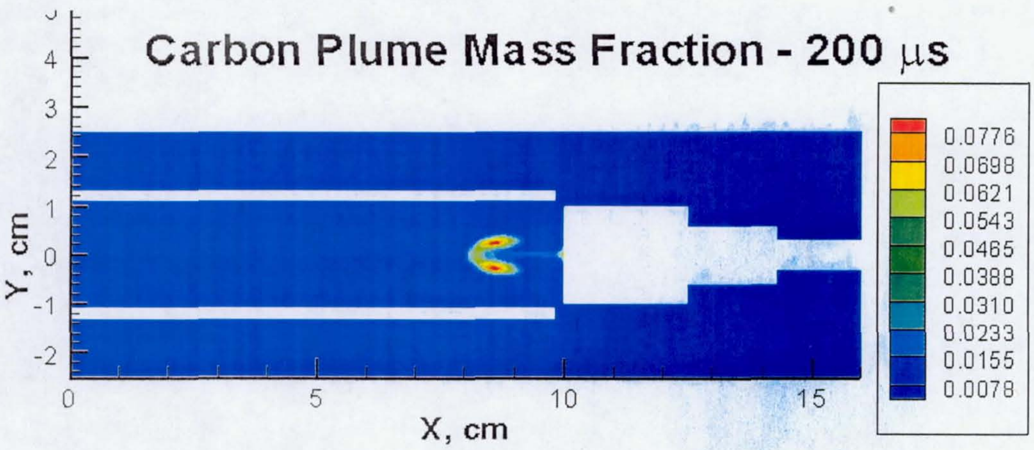

Carbon Plume Mass Fraction - 200 μs
Y, cm
X, cm
4
3
2
1
0
-1
-2
0
5
10
15
0.0776
0.0698
0.0621
0.0543
0.0465
0.0388
0.0310
0.0233
0.0155
0.0078

Figure §.36

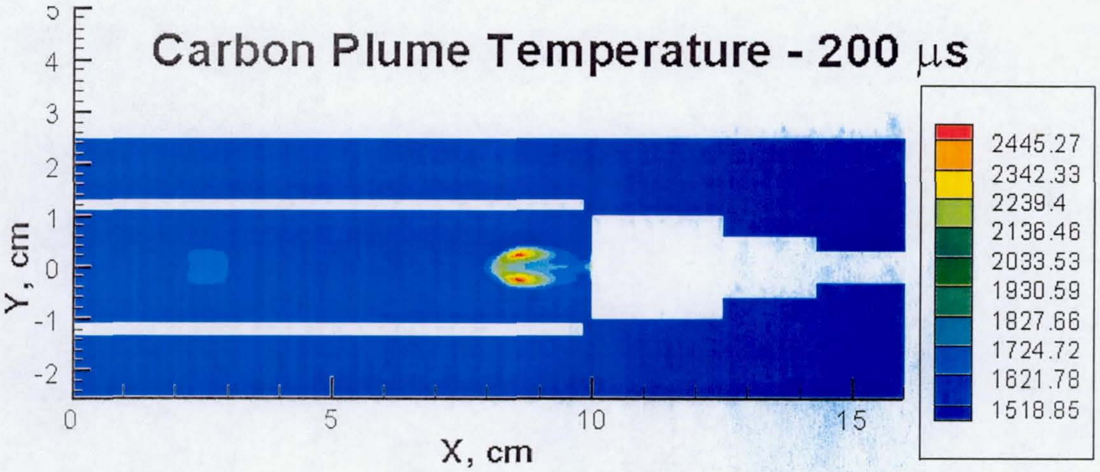
Carbon Plume Temperature - 200 μs
Y, cm
X, cm
5
4
3
2
1
0
-1
-2
0
5
10
15
2445.27
2342.33
2239.4
2136.46
2033.53
1930.59
1827.66
1724.72
1621.78
1518.85

Figure §.37

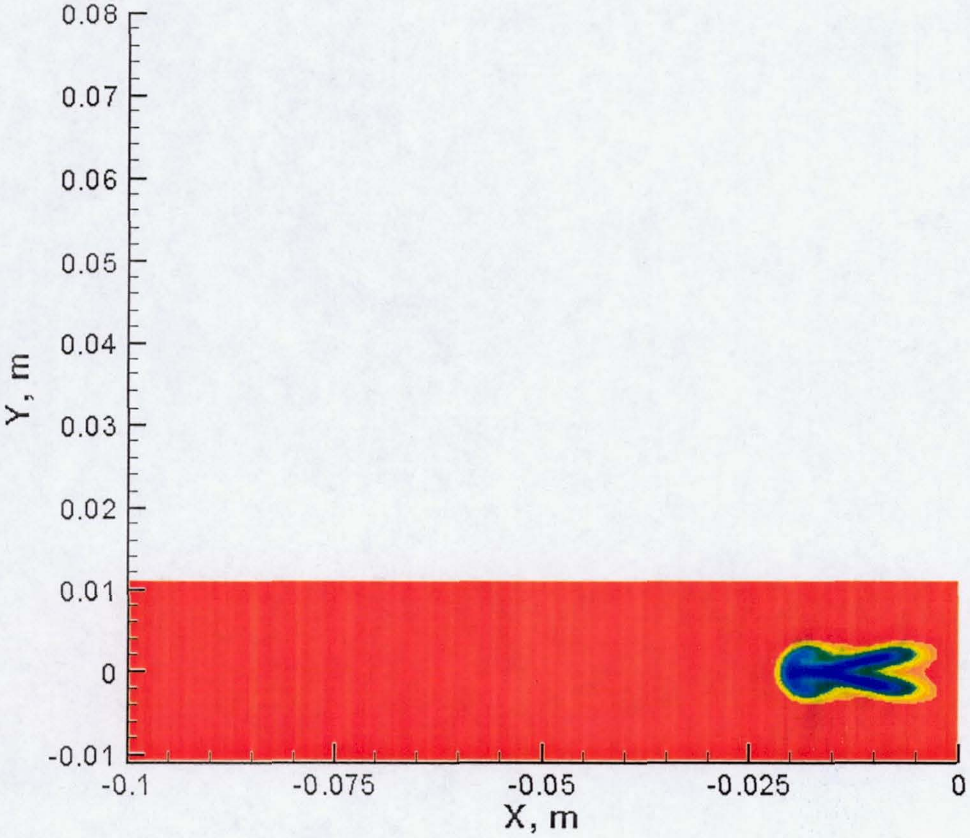

Figure §.38

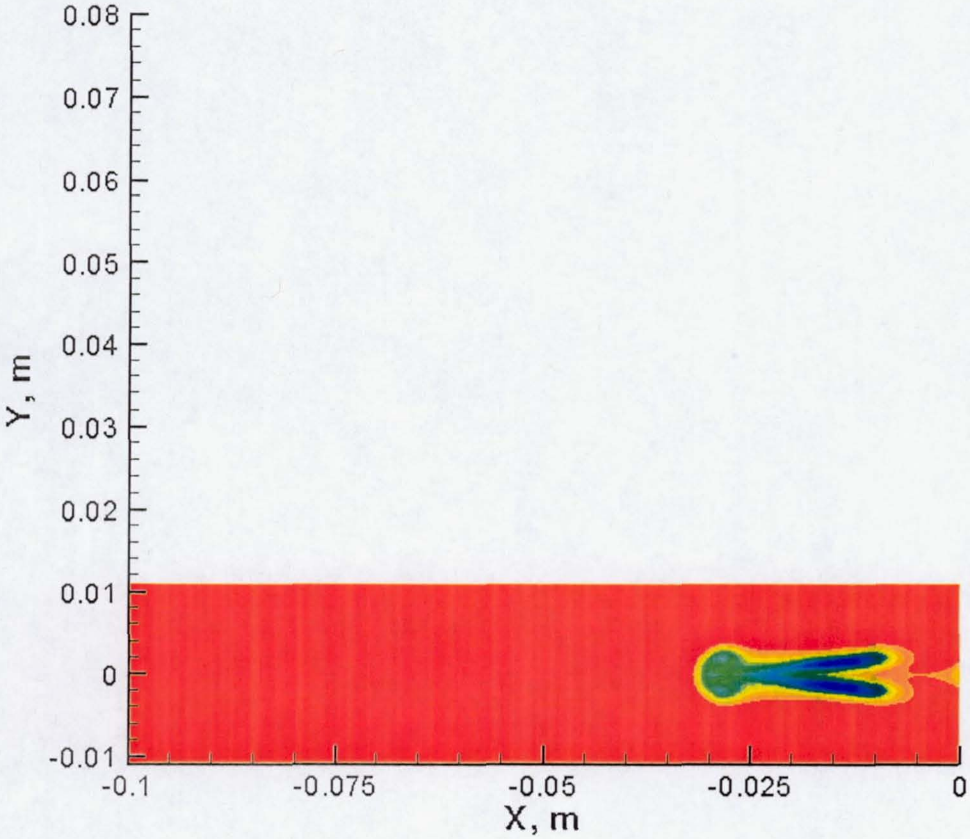

Figure §.39

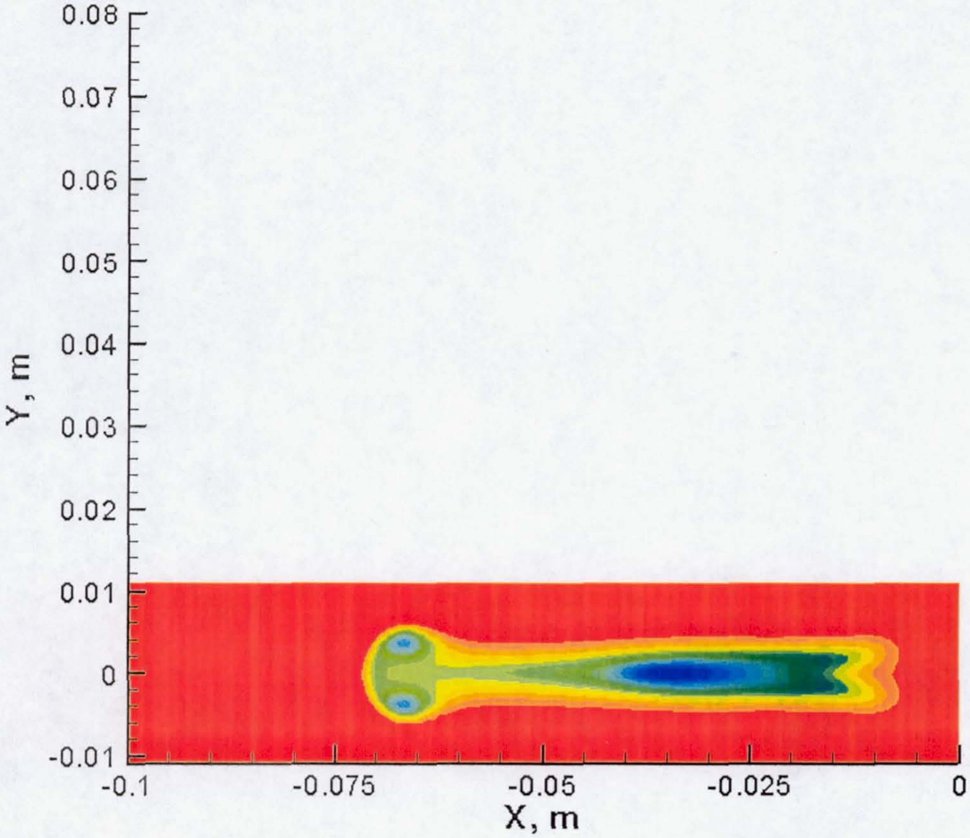

Figure §.40

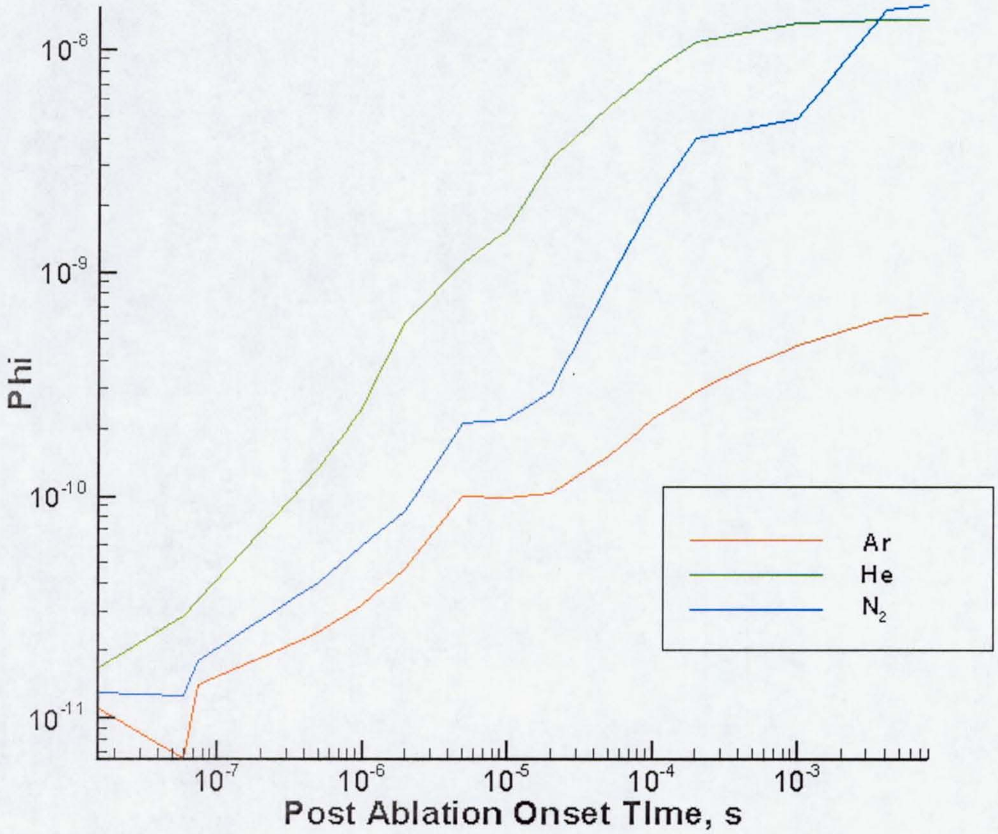

10^-8
10^-9
Phi
10^-10
10^-11
10^-7
10^-6
10^-5
10^-4
10^-3
Post Ablation Onset TIme, s
Ar
He
N2

Figure §.41

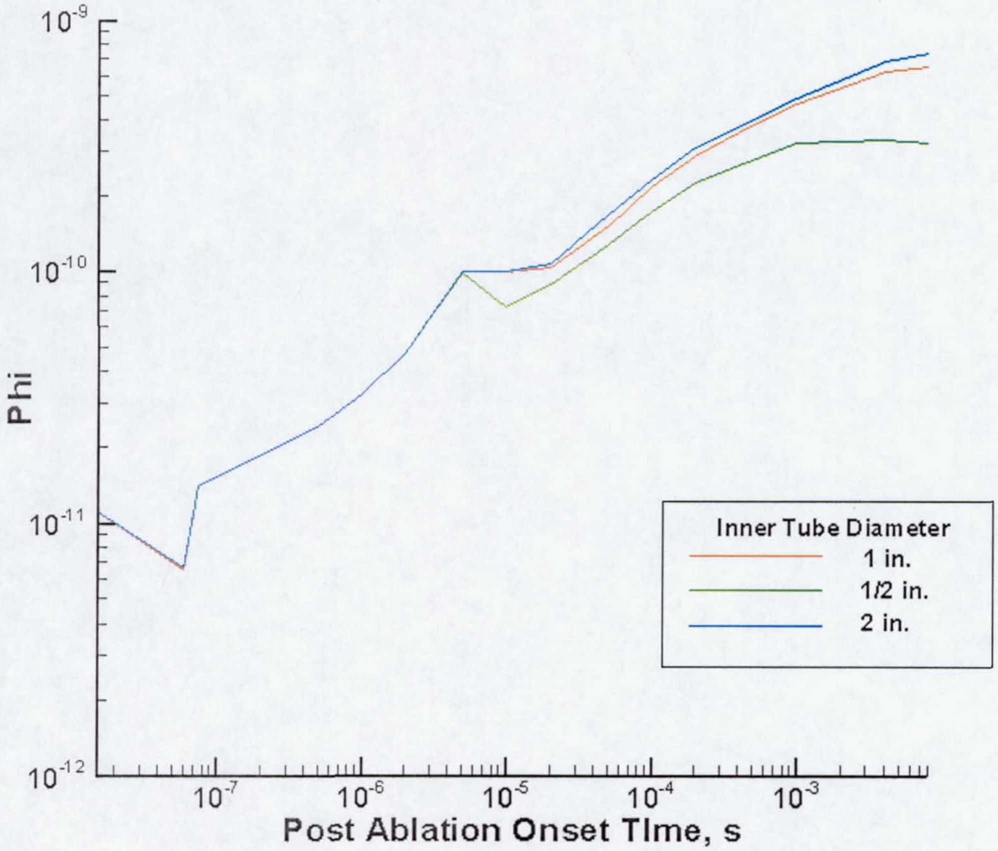

10^{-9}
10^{-10}
10^{-11}
10^{-12}
Phi
10^{-7}
10^{-6}
10^{-5}
10^{-4}
10^{-3}
Post Ablation Onset TIme, s
Inner Tube Diameter
1 in.
1/2 in.
2 in.

Figure §.42

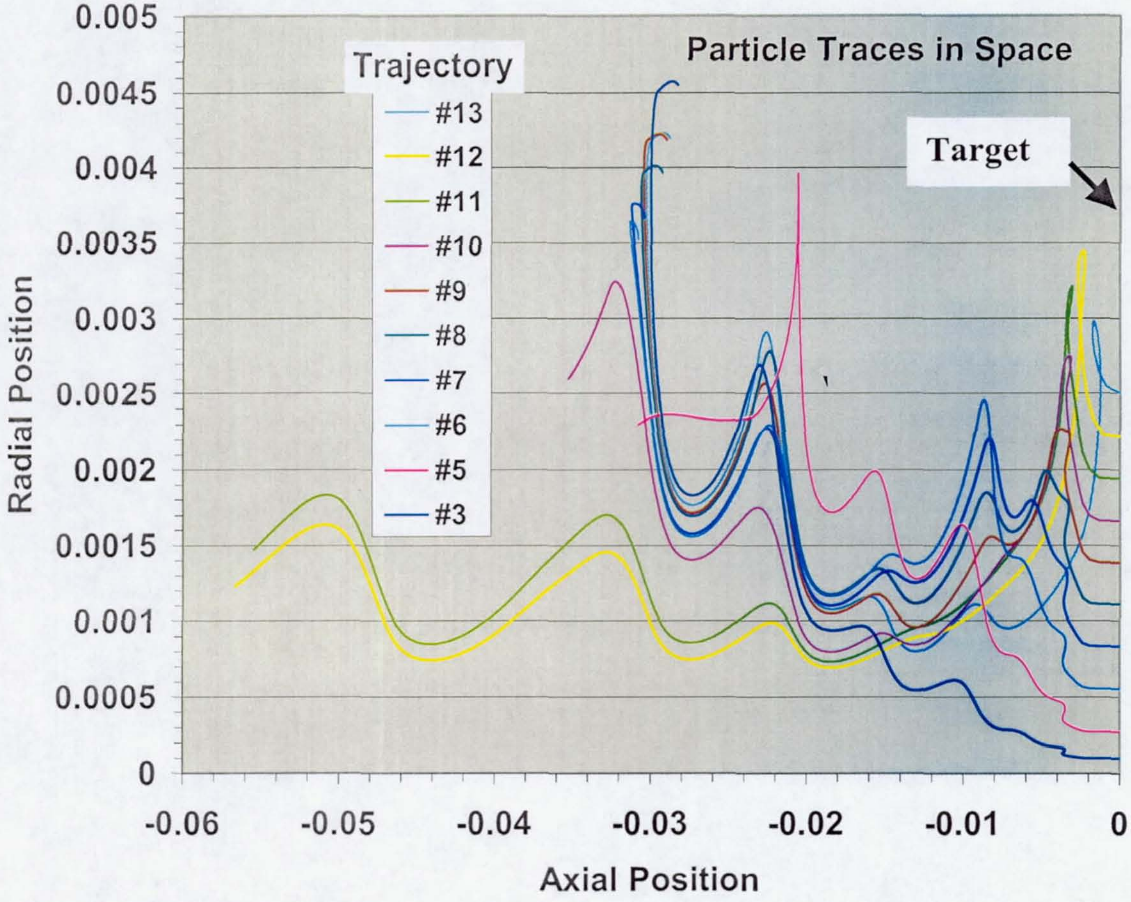

Fig. §.43 Streak lines in space for laser ablation axisymmetric calculation

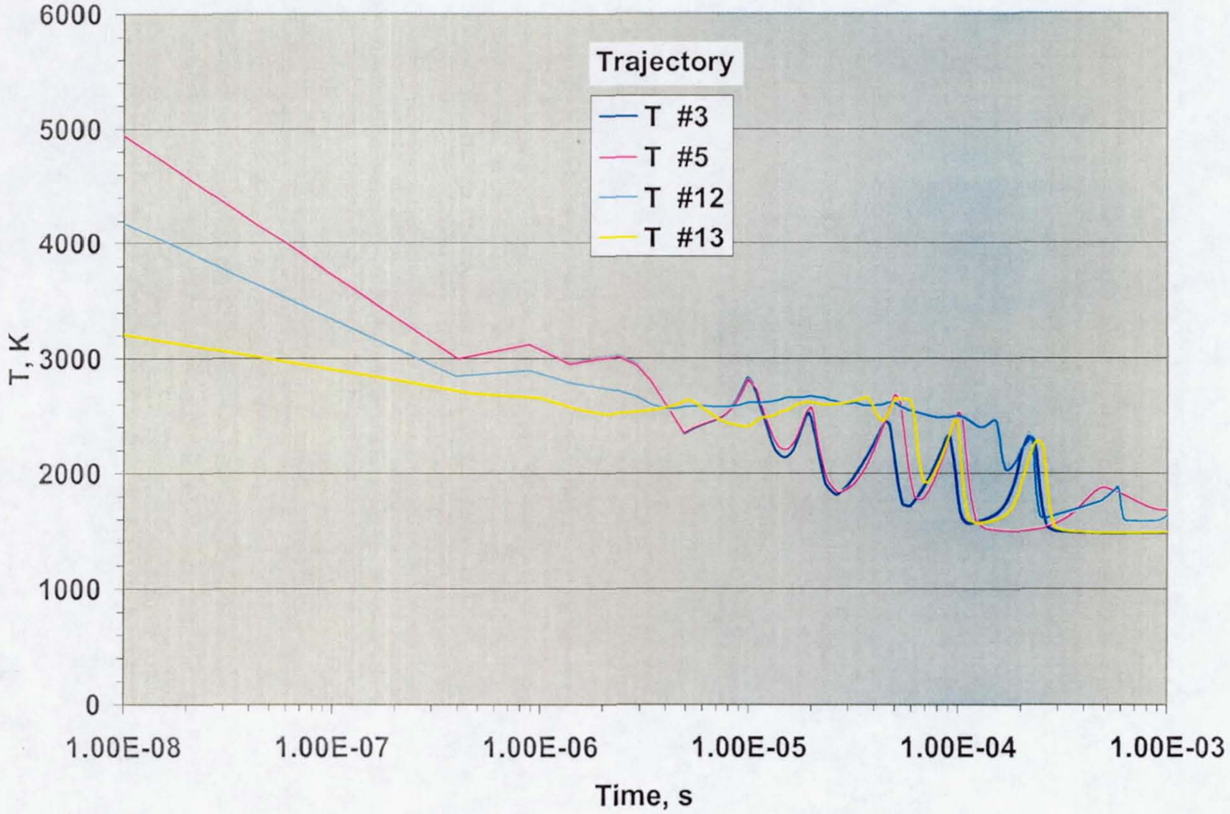

Fig. §.44 Temperature histories along selected streak lines for laser ablation calculations

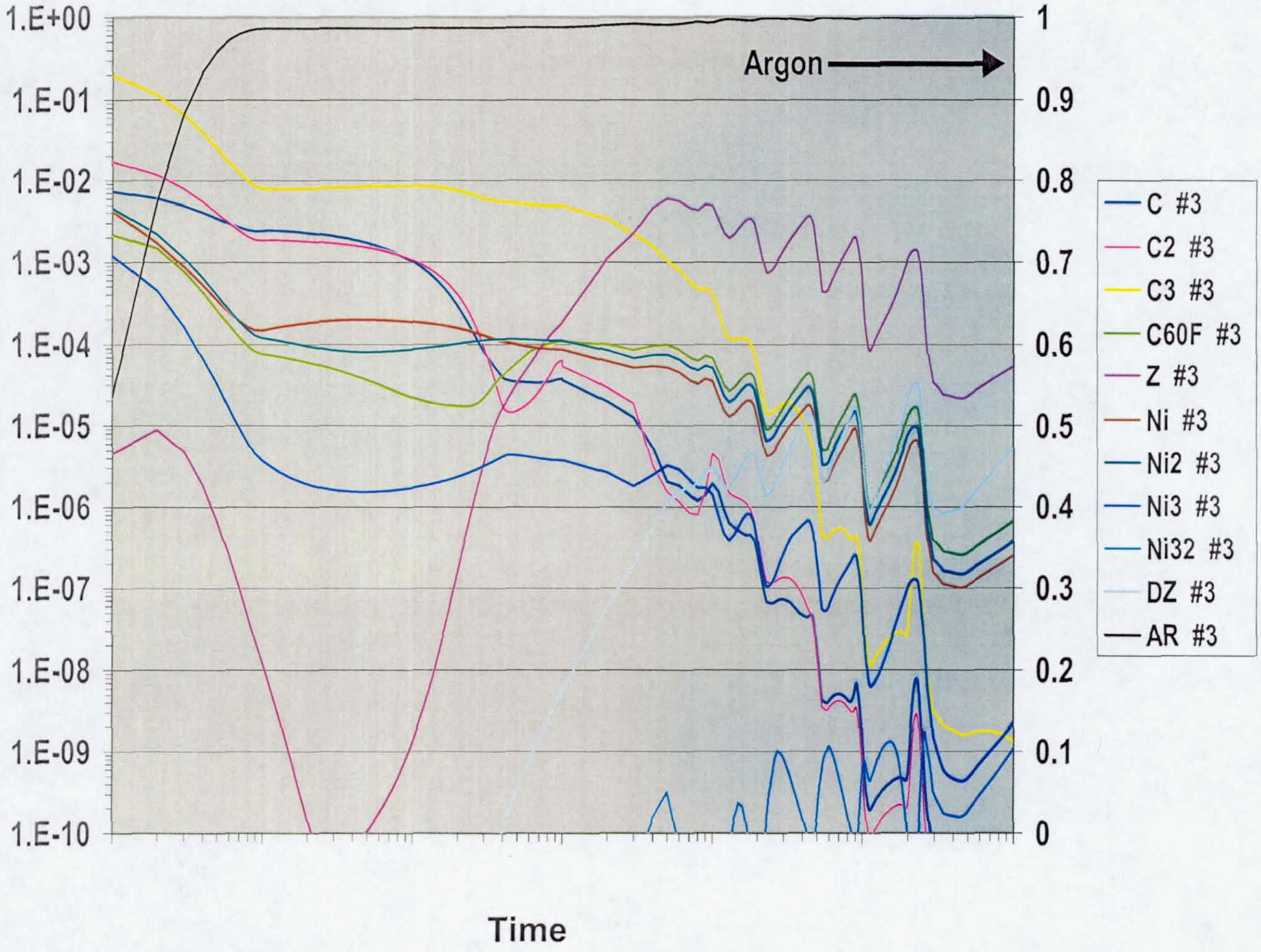

Fig. §.45 Example of evolution of species mass fractions along streak line in laser ablation. Arbitrary evaporation rate coefficients were used in calculation, therefore, data is not accurate, but only shown as an example of methodology.

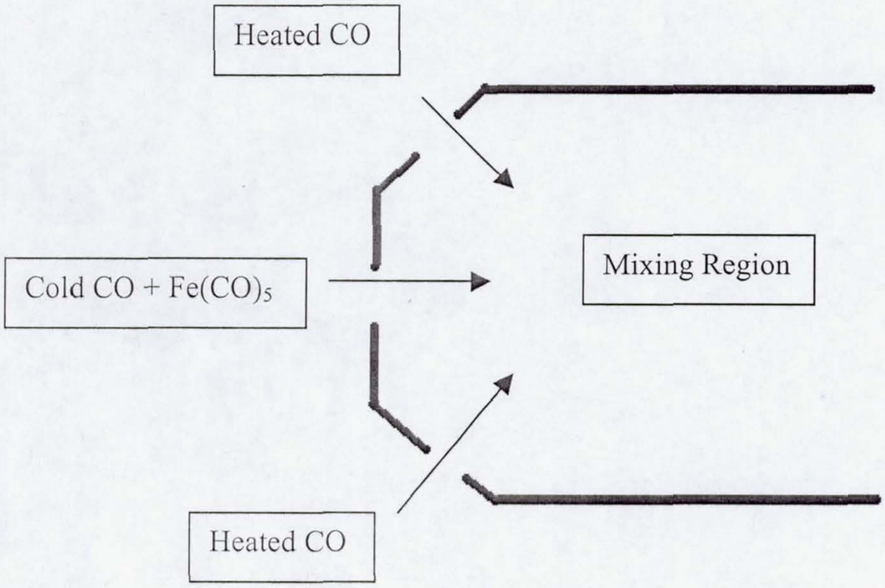

Figure §.46

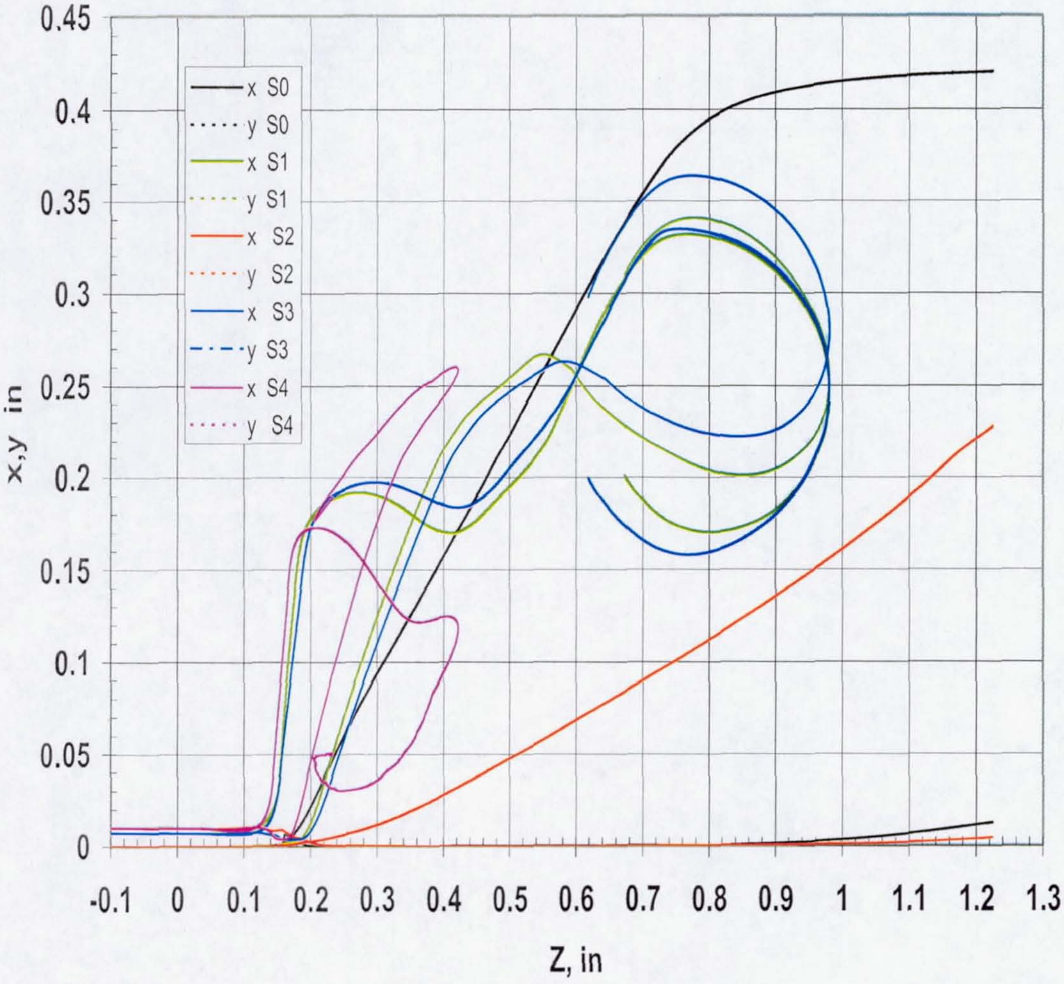

0.45
0.4
0.35
0.3
0.25
0.2
0.15
0.1
0.05
0
x,y in
-0.1
0
0.1
0.2
0.3
0.4
0.5
0.6
0.7
0.8
0.9
1
1.1
1.2
1.3
Z, in
x S0
y S0
x S1
y S1
x S2
y S2
x S3
y S3
x S4
y S4

Fig.47

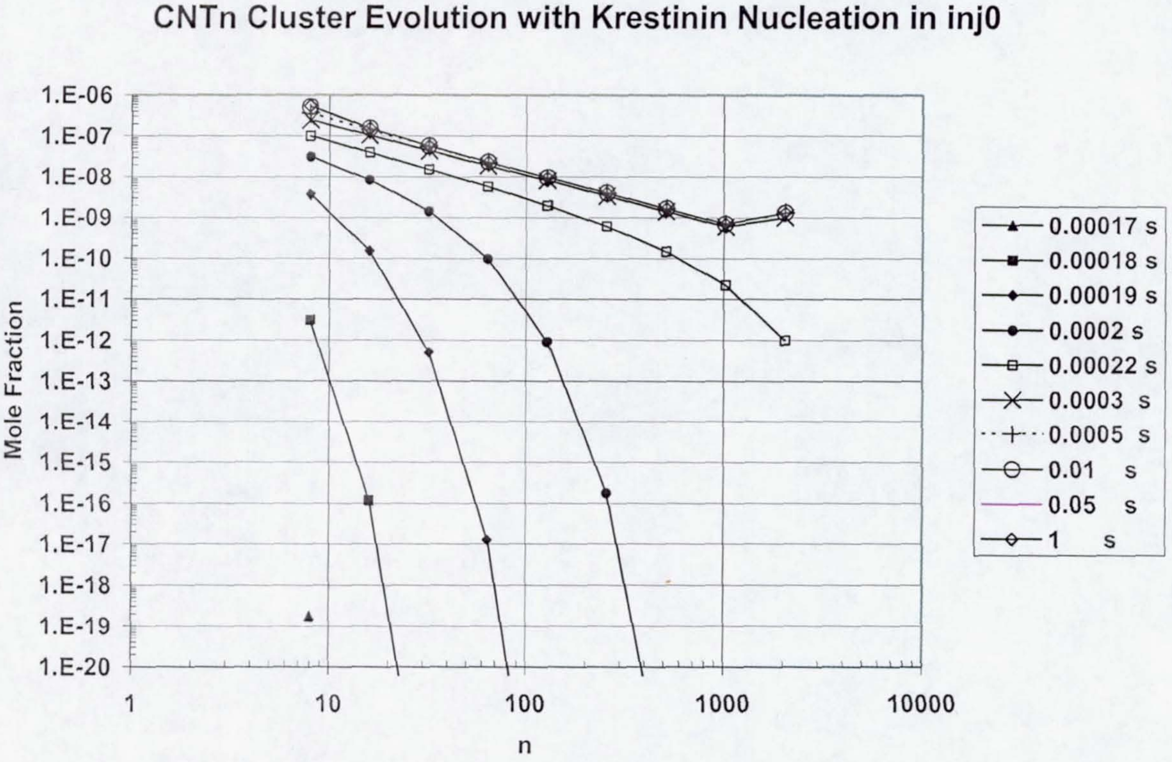
CNTn Cluster Evolution with Krestinin Nucleation in inj0
Mole Fraction
1.E-06
1.E-07
1.E-08
1.E-09
1.E-10
1.E-11
1.E-12
1.E-13
1.E-14
1.E-15
1.E-16
1.E-17
1.E-18
1.E-19
1.E-20
1
10
100
1000
10000
n
0.00017 s
0.00018 s
0.00019 s
0.0002 s
0.00022 s
0.0003 s
0.0005 s
0.01 s
0.05 s
1 s

Fig. 48

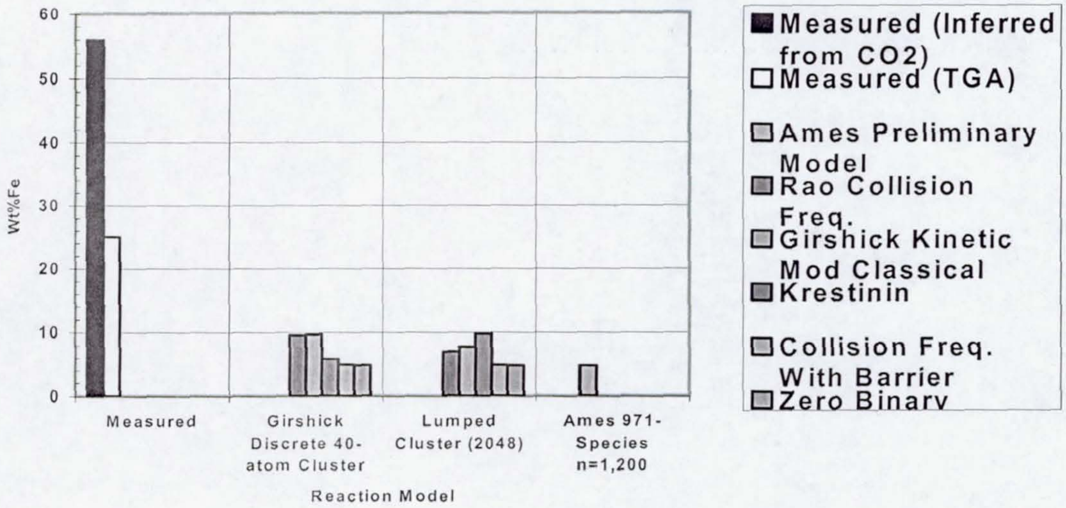

60
50
40
30
20
10
0
Wt%Fe
Measured
Girshick Discrete 40-atom Cluster
Lumped Cluster (2048)
Ames 971-Species n=1,200
Reaction Model
Measured (Inferred from CO2)
Measured (TGA)
Ames Preliminary Model
Rao Collision Freq.
Girshick Kinetic Mod Classical
Krestinin
Collision Freq. With Barrier
Zero Binary

Fig. 49

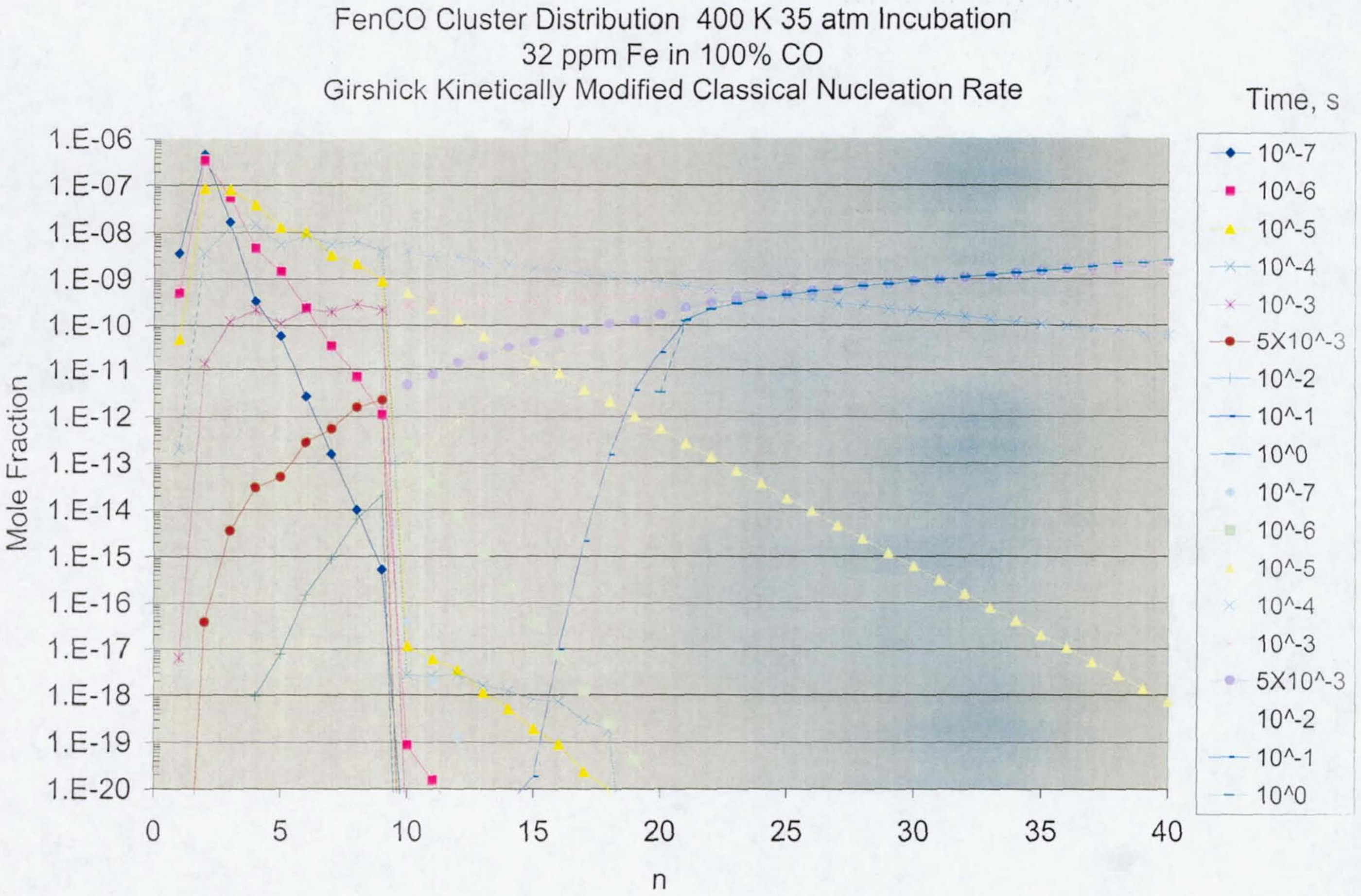
FenCO Cluster Distribution 400 K 35 atm Incubation
32 ppm Fe in 100% CO
Girshick Kinetically Modified Classical Nucleation Rate

Fig. 50